

# ON THE POTENTIAL OF LARGE EDDY SIMULATION TO SIMULATE CYCLONE SEPARATORS

Von der Fakultät für Maschinenbau der  
Technischen Universität Chemnitz

Genehmigte

**Dissertation**

Zur Erlangung des akademischen Grades

Doktoringenieur

(Dr.-Ing.)

Vorgelegt

von M.Sc. Hemdan Hanafy Shalaby  
geboren am 18.04.1967 in Ebehera, Ägypten

Gutachter:

Prof. Dr.-Ing. habil. Wozniak, Günter  
Prof. Dr.-Ing. habil. Bernd Platzer  
Prof. Dr.-Ing. habil. Dominique Thévenin

Chemnitz, den 24. Januar 2007

**ON THE POTENTIAL OF LARGE EDDY  
SIMULATION TO SIMULATE CYCLONE  
SEPARATORS**

By

M.Sc. Eng. Hemdan Hanafy Shalaby

SUBMITTED IN PARTIAL FULFILLMENT OF THE  
REQUIREMENTS FOR THE DEGREE OF  
DOCTOR OF ENGINEERING  
AT  
CHEMNITZ UNIVERSITY OF TECHNOLOGY  
CHEMNITZ, GERMANY  
JANUARY 2007

© Copyright by M.Sc. Eng. Hemdan Hanafy Shalaby, 2007

CHEMNITZ UNIVERSITY OF TECHNOLOGY  
DEPARTMENT OF  
MECHANICS, CHAIR: FLUID MECHANICS

The undersigned hereby certify that they have read and recommend to the Faculty of Mechanical Engineering for acceptance a thesis entitled **“On The Potential of Large Eddy Simulation to Simulate Cyclone Separators”** by **M.Sc. Eng. Hemdan Hanafy Shalaby** in partial fulfillment of the requirements for the degree of **Doctor of Engineering**.

Dated: January 2007

External Examiner: \_\_\_\_\_  
Dominique Thévenin

Research Supervisor: \_\_\_\_\_  
Günter Wozniak

Examining Committee: \_\_\_\_\_  
Bernd Platzer

\_\_\_\_\_

CHEMNITZ UNIVERSITY OF TECHNOLOGY

Date: **January 2007**

Author: **M.Sc. Eng. Hemdan Hanafy Shalaby**  
Title: **On The Potential of Large Eddy Simulation to Simulate Cyclone Separators**  
Institute: **Mechanics, Chair: Fluid Mechanics**  
Degree: **Ph.D.** Convocation: **January** Year: **2007**

Permission is herewith granted to Chemnitz University of Technology to circulate and to have copied for non-commercial purposes, at its discretion, the above title upon the request of individuals or institutions.

---

Signature of Author

THE AUTHOR RESERVES OTHER PUBLICATION RIGHTS, AND NEITHER THE THESIS NOR EXTENSIVE EXTRACTS FROM IT MAY BE PRINTED OR OTHERWISE REPRODUCED WITHOUT THE AUTHOR'S WRITTEN PERMISSION.

THE AUTHOR ATTESTS THAT PERMISSION HAS BEEN OBTAINED FOR THE USE OF ANY COPYRIGHTED MATERIAL APPEARING IN THIS THESIS (OTHER THAN BRIEF EXCERPTS REQUIRING ONLY PROPER ACKNOWLEDGEMENT IN SCHOLARLY WRITING) AND THAT ALL SUCH USE IS CLEARLY ACKNOWLEDGED.

*To my parents, my wife, and my children.*

# Table of Contents

Table of Contents	v
List of Tables	vii
Abstract	xiv
Acknowledgements	xvi
<b>1 Introduction and Literature survey</b>	<b>1</b>
1.1 Motivation . . . . .	1
1.2 Literature survey . . . . .	3
1.3 Thesis goals and contents . . . . .	10
<b>2 Continuous phase flow computation</b>	<b>13</b>
2.1 Introduction . . . . .	13
2.2 Turbulent scales . . . . .	15
2.3 Governing equations . . . . .	18
2.3.1 Reynolds-Averaged Navier-Stokes Models . . . . .	19
2.3.2 Standard $k - \epsilon$ turbulence model . . . . .	22
2.3.3 Reynolds Stress Model . . . . .	25
2.4 Large Eddy Simulation model (LES) and Smagorinsky model . . . . .	27
2.5 Solution algorithm . . . . .	33
<b>3 Dispersed Phase Motion</b>	<b>35</b>
3.1 Introduction . . . . .	35
3.2 Coupling between phases . . . . .	36
3.3 Classification parameters of gas-particle flows . . . . .	36
3.4 Euler-Lagrangian approach . . . . .	38
3.4.1 Equations for the particle rotation . . . . .	46

3.4.2	Influence of fluid turbulence on the particle movement . . . . .	47
3.4.3	Influence of particles on the fluid movement . . . . .	49
3.5	Particle/wall collisions . . . . .	51
3.6	Computation of the dispersed phase flow . . . . .	55
3.6.1	Trajectory computation . . . . .	55
3.6.2	Simultaneous particle tracking . . . . .	56
3.7	Solution algorithm . . . . .	56
<b>4</b>	<b>Validation process and computational results of cyclone flows</b>	<b>58</b>
4.1	Validation Process . . . . .	58
4.1.1	Channel flow . . . . .	58
4.1.2	Flow and geometry descriptions . . . . .	60
4.1.3	Computational parameters . . . . .	61
4.1.4	Periodic boundary condition . . . . .	62
4.1.5	Wall boundary conditions . . . . .	62
4.1.6	Results and discussions . . . . .	63
4.2	Cyclone Flows . . . . .	68
4.2.1	Computational parameters . . . . .	69
4.2.2	Continuous flow predictions (Cyclone A) . . . . .	73
4.2.3	Pressure drop (Cyclone A) . . . . .	87
4.2.4	Continuous flow predictions (Cyclone B) . . . . .	91
4.3	Dispersed phase motion . . . . .	96
4.3.1	Cyclone separation efficiency (Cyclone A) . . . . .	97
4.3.2	Particle trajectories (Cyclone A) . . . . .	98
4.4	Conclusion . . . . .	100
<b>5</b>	<b>Concluding Remarks and future work</b>	<b>102</b>
	<b>List of Figures</b>	<b>108</b>
	<b>Bibliography</b>	<b>109</b>

# List of Tables

4.1	Cyclone dimensions in mm . . . . .	70
4.2	Computed variables . . . . .	73



## Latin symbols

Symbol	Meaning
$A^+$	van Driest factor
$a$	Cyclone inlet duct width
$b$	Cyclone inlet duct height
$D$	Cyclone diameter, dissipation length scale
$D_e$	Outlet pipe diameter
$D_{ij}$	Convection and diffusion of $\overline{u'_i u'_j}$
$D/D_t$	Total time derivative
$E$	Energy spectrum
$c_M$	Magnus force factor
$c_S$	Saffman force factor
$c_W$	Drag force coefficient
$c_{VM}$	Virtual mass force factor
$c_\omega$	Rotation factor
$d_P$	Particle diameter
$e_w$	Impact number of particle wall impact
$\vec{F}_G$	Gravitational force
$\vec{F}_M$	Magnus force
$\vec{F}_S$	Saffman force
$\vec{F}_W$	Drag force
$\vec{F}_\sigma$	Surface force
$f_u$	Wall damping function
$\vec{g}, g_x, g_y, g_z$	Gravity force
$G$	Convolution kernel
$H_r$	Mean roughness depth
$I_P$	Moment of inertia of the particle
$k$	Kinetic energy of turbulence
$L_E$	Size of a turbulence eddy
$L_r$	Mean cycle of roughness
$l$	Integral length scale
$m_P$	Particle mass
$m_F$	Fluid mass

$\dot{m}_F, \dot{m}_P$	Fluid and particle flow rate
$\vec{n}, n_x, n_y, n_z$	Normal vector
$\dot{N}_P$	Particle stream along a trajectory
$N_T$	Number of trajectories
$N_P$	Local number of particles per package and/or cell
$\dot{N}_{in}(d_P)$	Inlet particle flow rate
$\dot{N}_{out}(d_P)$	Outlet particle flow rate
$P$	Perimeter
$p$	Static pressure
$P_{ij}$	Production of $\overline{u'_i u'_j}$
$P_k$	Production term for $k - \epsilon$ equation
$Q_{P_u}, Q_{P_v}$	Particle source terms for the impulse equations
$S_g$	Geometrical swirl number
$T$	Temperature, average interval
$T_{d_P}$	Separation rate
$T_D$	Transit time of a turbulence eddy
$T_E$	Eddy life span
$T_u$	Turbulence intensity
$t$	Time
$u'_F, v'_F, w'_F$	Fluctuation of fluid speed
$\vec{v}_F, u_F, v_F, w_F$	Temporally averaged fluid speed
$\vec{v}_P, u_P, v_P, w_P$	Particle velocity
$\overline{u_i u_j}$	Reynolds-stress tensor
$\vec{v}$	Fluid velocity
$v_r$	Relative velocity between particle surface and wall
$\vec{v}_{rel}$	Relative velocity between particle and fluid
$\vec{V}$	Velocity vector
$V_P$	Particle volume
$x, y, z$	Cartesian coordinates

## Greek Symbols

Symbol	Meaning
$\alpha_F, \alpha_P$	Volume fraction of the fluid and/or the particle phase
$\gamma$	Inclination of the virtual wall
$\Delta\gamma$	Standard deviation of $\gamma$
$\Delta$	Differential, filter length scale
$\overline{\Delta}$	Cutoff length
$\Delta H_r$	Standard deviation of the roughness height.
$\Delta t$	Time step
$\Delta t_E$	Reciprocal effect time of the particle with a turbulence eddy
$\delta_{ij}$	Kronecker constant
$\varepsilon$	Dissipation rate
$\epsilon_{ij}$	Dissipation of $\overline{u'_i u'_j}$
$\phi_{ij}$	Pressure-strain term
$\phi_{ij,1}, \phi_{ij,2}$	Two components of pressure-strain term
$\eta$	Kolmogorov length scale, mass loading
$\kappa$	von Kármán constant
$\mu_{eff}$	Effective viscosity
$\mu_F, \mu, \mu_t$	Dynamic, molecular, turbulent viscosity of the fluid
$\nu_F$	Kinematic viscosity of the fluid
$\sigma$	Surface tension
$\sigma_F, \sigma_P$	Mixture density of the fluid and/or particle phase
$\sigma_M$	Constant for Magnus force factor $c_M$
$\rho_F, \rho_P$	Density of the fluid and particle
$\tau$	Kolmogorov time scale
$\tau_A$	Aerodynamic relaxation time
$\tau_S$	Characteristic system time
$\tau_{xx}, \tau_{xy}, \tau_{xz}$	Components of the stress tensor
$\vec{\omega}_F$	Rotation of the fluid
$\vec{\omega}_P$	Rotation velocity of the particle
$\omega_{rel}$	Rotation of the particle relative to the fluid

## Constants and characteristic numbers

Symbol	Meaning
$c_1, c_2$	Constants of $\phi_{ij}$ components
$C_s$	Smagorinsky constant
$C_\mu, C_{\varepsilon 1}, C_{\varepsilon 2}$	Constant for $k$ - $\varepsilon$ model
$K_0$	Kolmogorov constant
$\sigma_M$	Constant for calculating $c_M$
$\sigma_k, \sigma_\varepsilon$	Constant for $k$ - $\varepsilon$ model
Re	Reynolds number
$Re_P$	Particle Reynolds number
$Re_\omega$	Rotational Reynolds number
$Re_S$	Reynolds number of shear flow
St	Stokes number
Str	Strouhal number

## Abbreviations

ASM	Algebraic Stress Model
BBO	Basset-Bousinesq-Oseen equation for particles
CFD	Computational Fluid Dynamics
CLIC	Chemnitzer Linux Cluster
CPU	Central Processor Unit
DNS	Direct Numerical Simulation
FVM	Finite Volume Method
LDA	Laser Doppler Anemometry
LES	Large Eddy Simulation
LSD	Lagrangian Stochastic-Deterministic
MPI	Message Passing Interface
NS	Navier-Stokes
PDA	Phase Doppler Anemometry
PIV	Particle Image Velocimetry
PVM	Parallel Virtual Machine
RANS	Reynolds-Averaged Navier-Stokes Equation
RNG	Renormalization Group
RSM	Reynolds Stress Model
SIP	Strongly Implicit Procedure
SGS	Sub-Grid Scale
PIC	Particle in Cell
PSI-Cell	Particle Source in Cell
SIMPLE	Semi-Implicit Method for Pressure Linked Equations

# Abstract

This study was concerned with the most common reverse flow type of cyclones where the flow enters the cyclone through a tangential inlet and leaves via an axial outlet pipe at the top of the cyclone. Numerical computations of two different cyclones were based on the so-called Stairmand cyclone. The difference in geometry between these two cyclones was basically characterized by the geometrical *swirl number*  $S_g$  of 3.5 and 4.

Turbulent secondary flows inside a straight square channel have been studied numerically by using Large Eddy Simulation (LES) in order to verify the implementation process. Prandtl's secondary motion calculated by LES shows satisfying agreement with both, Direct Numerical Simulation (DNS) and experimental results.

Numerical calculations were carried out at various axial positions and at the apex cone of a gas cyclone separator. Two different NS-solvers (a commercial one, and a research code), based on a pressure correction algorithm of the SIMPLE method have been applied to predict the flow behavior. The flow was assumed as unsteady, incompressible and isothermal. A  $k - \epsilon$  turbulence model has been applied first using the commercial code to investigate the gas flow. Due to the nature of cyclone flows, which exhibit highly curved streamlines and anisotropic turbulence, advanced turbulence models such as RSM (Reynolds Stress Model) and LES (Large Eddy Simulation) have been used as well. The RSM simulation was performed using the commercial package CFX4.4, while for the LES calculations the research code MISTRAL/PartFlow-3D code developed in our multiphase research group has been applied utilizing the Smagorinsky model. It was found that the  $k - \epsilon$  model cannot

predict flow phenomena inside the cyclone properly due to the strong curvature of the streamlines. The RSM results are comparable with LES results in the area of the apex cone plane. However, the application of the LES reveals qualitative agreement with the experimental data, but requires higher computer capacity and longer running times than RSM.

These calculations of the continuous phase flow were the basis for modeling the behavior of the solid particles in the cyclone separator. Particle trajectories, pressure drop and the cyclone separation efficiency have been studied in some detail.

This thesis is organized into five chapters. After an introduction and overview, chapter 2 deals with continuous phase flow turbulence modeling including the governing equations. The emphasis will be based on LES modelling. Furthermore, the disperse phase motion is treated in chapter 3. In chapter 4, the validation process of LES implementation with channel flow is presented. Moreover, prediction profiles of the gas flow are presented and discussed. In addition, disperse phase flow results are presented and discussed such as particle trajectories; pressure drop and cyclone separation efficiency are also discussed. Chapter 5 summarizes and concludes the thesis.

# Acknowledgements

First I would like to thank my wife for her patience with me especially during the final stage of preparing this thesis. To you Entsar I will always be indebted and in *love*.

Of course, I am grateful to my parents for their patience and *love*. Without them this work would never have come into existence (literally).

I am grateful to my supervisor Prof. Dr.-Ing. Günter Wozniak for his many suggestions and constant support during this research. I have learned many things from his experience and hope to continue collaboration with him in the future. I am also thankful to Prof. Dr.-Ing. Bernd Platzler for his guidance through the first year of my research.

Really, I was lucky during my Ph.D research to be able to work with several enthusiastic people, Dr.-Ing. Thomas Frank, Dr.-Ing Helfred Schneider, Dr.-Ing Jordan Denev and Dr.-Ing Klaus Pachler. They shared with me their knowledge of Computational Fluid Dynamics and provided many useful references and friendly encouragement.

I should also mention that Dr.-Ing. Klaus Wozniak supported me in part of my research especially in developing my technical language.

I am also grateful to Prof. Dr.-Ing. Dominique Thévenin for financing and allowing me to be part of his research team for the period of 2004 until now. This support was crucial to the successful completion of this research.

Chemnitz, Germany  
May 1, 2006

Hemdan Shalaby



# Chapter 1

## Introduction and Literature survey

### 1.1 Motivation

The cyclone separator is one of the most elegant pieces of engineering equipment. It is a device with no moving parts and virtually no maintenance. It enables particles of micrometers in size to be separated from a gas moving at about 15 m/s without excessive pressure-drop.

Cyclone separators are very widely used throughout industry. Moreover, they can be found in all sizes and shapes. They can be used in some industries such as:

- Oil and gas
- Power generation
- Incineration plants
- Iron and steel industry
- Sand plants
- Cement plants

- Coking plants
- Coal fired boilers
- Food industries

A full understanding of how the cyclone separator works and how individual particles behave within it is not yet available. Little information has been gathered until the invention of the measuring equipment necessary to measure fluid velocities within cyclones (laser Doppler anemometry - LDA). Ultimately, the development of computational fluid dynamics (CFD) codes could accurately model swirling flows within the cyclone.

A cyclone separator is a device, which causes centrifugal separation of materials in a fluid flow. Unlike the slow settling of particles within a settling tank, a cyclone separator system yields fast separation and utilizes less space. Separation occurs quickly because one "g" of the gravitational force is replaced by multiple "g" of the acting centrifugal force, Figure 1.1. The material to be separated can consist of solid particles or liquids, i.e. droplets, which are classified according to size, shape, and density. The cyclone utilizes the energy obtained from the fluid pressure gradient to create rotational fluid motion. This rotational motion causes the dispersed phase to separate relatively fast due to the strong acting forces. In widely used reverse flow cyclones of the cylinder on cone design type, gases spiral down from a tangential inlet towards the apex of a conical section, where the flow is reversed and the particles are collected in a hopper. The continuous phase then proceeds upward in an inner core flow towards the gas exit via the vortex finder. Cyclone designs have been developed over many years since their invention. Nowadays, there exist a large number of

different types for various industrial applications. Many attempts have been made to improve the performance of cyclones by modifying their shape in terms of the ratio of different key dimensions. Normally, the continuous phase flow still carries some particles when it proceeds upward in the inner flow core towards the gas exit. Therefore, a solid apex cone has been incorporated in the cyclone to slow down the flow inside the dust collector (hopper).

## 1.2 Literature survey

Computational fluid dynamics has become a widely accepted design tool for research and development over the last decade. The number of publications in the field of experimental investigations of cyclone flows is still exceeding by far the number of published numerical investigations. In the past 2-dimensional analysis has been performed using radial symmetry of the flow in the cyclone which sometimes leads to inadmissible simplifications [1].

In recent years much work with 3-dimensional predictions of gas-particle flow in cyclone separators has been published. The results show that the quality of the numerical solutions strongly depends on the type of turbulence model used for the continuous phase flow. Minier et al. [2] used a 3-dimensional Eulerian-Lagrangian approach on a 3-dimensional numerical grid with approx. 26,000 grid cells applying a modified turbulence model. A comparison of the predicted flow field with experimental data was not included in this publication. Furthermore, these authors used a Lagrangian model for the prediction of the particulate phase. Variations of the coefficients of restitution in the particle-wall model from elastic to completely inelastic bouncing behavior have shown only minor influence on the predicted efficiency grade.

After publication of a number of 2-dimensional cyclone flow predictions collected in [3], Boysan et al. [4] presented the theory of a 3-dimensional modified algebraic Reynolds stress turbulence model (ASM). They found good agreement between the predicted flow field in the investigated cyclone in the range of the potential vortex and an at least qualitative agreement in the core region.

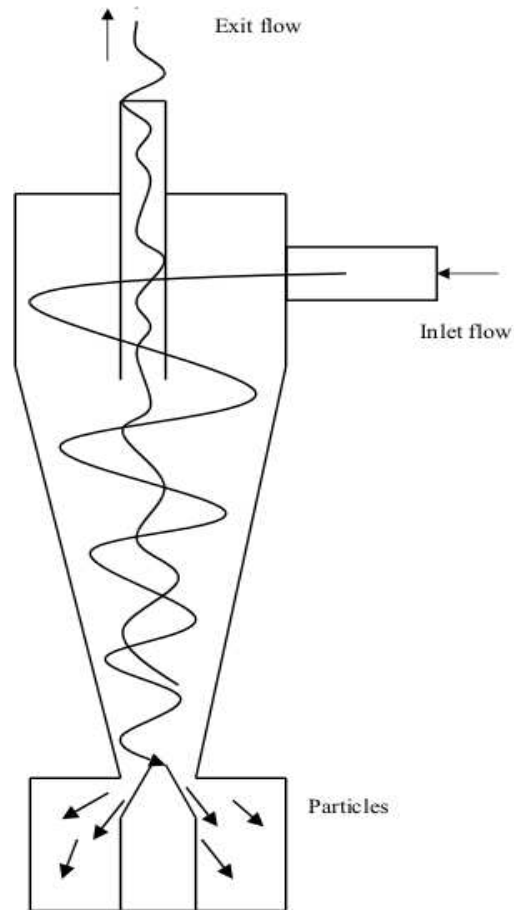


Figure 1.1: Schematic of the cyclone separator principle.

Gorton-Hülgerth [1] and Staudinger et al. [5] performed 3-dimensional calculations for a series of standard cyclones using the commercial computer package FLUENT 4.4.7 and FLUENT UNS 4.2.10 with the built-in RSM turbulence model on a

numerical grid with 170,000 cells. Several different cyclone geometries (e.g. variation of the hopper entrance geometry) have been investigated. Numerical results for the gas velocity field show very good agreement with the LDA measurements of [1]. A numerical prediction of a flow in a hydrocyclone has been presented in [6] using the commercial computer package CFX-5 with two different build-in Reynolds Stress Model (RSM); the Launder, Reece, Rodi closure model (LRR) and the quadratic Speziale, Sarko and Gatski closure model (SSG). Calculations were carried out on a 3-dimensional hexahedral mesh generated with ICEM/CFD-HEXA with approximately 151,000 grid cells. Best agreement with experimental data could be achieved with the SSG formulation of the RSM turbulence model. Predictions of the motion of the particulate phase or the collection efficiency of the investigated cyclone have not been presented in the publication.

The application of a 3-dimensional LES model has been shown within the frame of the LABFLOW code developed by Shell, Netherlands for the numerical prediction of gas-particle flows in cyclone systems [7]. LABFLOW is based on the Lattice-Boltzmann method. The comparison between the measurements and numerical calculations of time averaged tangential velocities at two vertical positions in the cyclone shows an excellent agreement.

Frank et al. [8, 9, 10, 11] developed a 3-dimensional Eulerian-Lagrangian approach (MISTRAL/PartFlow-3D) for the numerical prediction of gas-particle flows. Special emphasis has been put on the parallelization of the numerical algorithm for the prediction of the continuous phase as well as for the particle trajectory calculation in order to enable numerical predictions for disperse gas-particle flows in large

and complex flow configurations of various industrial applications. Derksen [12] presented a numerical prediction of a flow in a Stairmand high-efficiency cyclone at  $Re = 280,000$ . He performed the calculations by using a Large-Eddy Simulation model. His results agree well with experimental data (LDA measurements of the average and RMS values of the tangential and axial velocity).

Souza et al. [13] have used sub-grid scale modeling, which characterizes Large-Eddy Simulations (LES) to predict the behavior of a water-fed hydro cyclone. The numerical results captured the main features of the flow pattern and agreed reasonably well with experiments. The authors suggested that LES represents an interesting alternative to classical turbulence models when applied to the numerical solution of fluid flows within hydro cyclones. Huang et al. [14] developed a partitioning parallel procedure to numerically simulate the fluid flow in complex 3 dimensional domains. They used the developed algorithm to simulate the 3 dimensional turbulent swirling gas flow in cyclone separators. The authors concluded that the developed algorithm could well remove the limitation of speed and capacity of personal computers on a large scale.

A numerical model for the analysis of the fluid flow and particle separation has been presented by Ingham and Ma [15]. The authors discussed in their article the key design parameters for the cyclones. Further, they studied their effect on the overall performance of the cyclone. Generalized performance correlations for the pressure coefficient and the total collection efficiency to dimensionless geometric and operational parameters have been developed by Pant et al. [16]. The authors deduced their correlations based on the results of the numerical computations. The influence of agglomeration on the particle separation has been studied by Ho and Sommerfeld

[17]. The authors stated that the separation efficiency increases for small particles. Lu et al. [18] adopted the SIMPLE algorithm and used a  $k - \epsilon$  turbulence model and a non-staggered grid pressure interpolation method in order to have a numerical value emulation for the cyclone separators flow field. By this way, they proposed an optimum separator and tested it by industry experiments with excellent practical results. In order to investigate the influence of the swirl effect on the particle motion in detail, the coupling method was adopted in [19]. Their investigations are based on using Direct Numerical Simulation (DNS) of gas-particle swirling flows in the axially rotating pipe at a Reynolds number of 180. They investigated the effect of inter-particle collisions on particle motions. The particles accumulation is considered to take place near the wall due to the centrifugal force and since the local particle concentration is very high in this region [19].

Portela and Oliemans [20] have developed a DNS code of particle-laden turbulent flows using an Eulerian-Lagrangian approach. The code was used to study the dynamics of particle-turbulence interactions in channel and pipe flows loaded with small, heavy particles. The authors suggested that the near-wall particle-fluid interaction can be understood in terms of the interaction of the particles with streamwise vortices [20]. Furthermore, they state that strong streamwise vortices above the wall are responsible for the elongated streaky patterns that occur both in the deposition and resuspension of the particles. Ran et al. [21] concluded that the initial position of the particles at the entrance of the separator and the particles diameter play an important role in the particles dynamics.

The collection efficiency of a small-scale cyclone for particles smaller than  $5 \mu m$  in diameter has been studied by Suguri et al. [22]. Single-phase turbulence flow fields

in a gas solid cyclone separator are investigated by using a standard  $k - \epsilon$  model, a Renormalization Group (RNG) model and a Reynolds Stress Model (RSM) [23]. The authors showed that the predicted results of the RSM model have been found to be the most rational forecast results of a vortex structure with a tangential velocity distribution. However, some discrepancies still exist between the simulation results and experimental ones [23]. Wu et al. [24] have used RSM to simulate the cyclone flow. Their results showed that stagnation and reverse flow in axial direction near the cyclone center exists. In addition, the tangential velocity increased with the decrease of the finder tube diameter. From the point of view of the influence of turbulence structure, Xiaodong et al. [25] presented an elementary numerical analysis of the interaction between a particle and a gas phase. The effects of turbulence structure and the thickness of the boundary layer on the separation efficiency in a cyclone separator have been investigated. In addition, the effects of the Saffman force on the particle trajectory are analyzed. The results indicate that the separation efficiency decreases with an increase in turbulence intensity and increases with a decrease in the thickness of the boundary layer [25]. The Saffman force can enhance the separation of small particles and also can shorten their residence time in the cyclone.

The effect of the apex cone height on the particle separation performance of a cyclone separator has been studied by Yoshida et al. [26]. They found that the effect of an apex cone is to decrease the cut size (the particle size with equal probability that particle exits at the top of the cyclone or bottom of the cyclone) and to increase the collection efficiency. The cut size indicates the minimum value for the specific height of the apex cone. The optimum apex cone height changes to the lower position as the cyclone inlet velocity increases. Detached Stress Model (DSM) provided by CFX5.5



was adopted to predict the gas flow field in the cyclone [27]. The authors stated that the DSM model could precisely predict the flow field inside the cyclone separator. Hu et al. [28] have simulated the three-dimensional strongly swirling turbulent flow in a cyclone separator with a volute inlet to optimize the design by improving the pressure-strain generation and convection terms of the Reynolds stress equation in FLUENT 6.0. They obtained good agreement between the predictions and experiments in the separation space and the dust hopper. In the vortex finder the agreement between predictions and measurements is poor, indicating that the turbulence model still needs further improvement. An Eulerian-Lagrangian numerical method is used to simulate the cyclone separator by Snider et al. [29]. The three-dimensional transient simulations showed excellent agreement with measured data. The authors stated that the CFD analysis reveals details that cannot be experimentally measured, such as internal particle size segregation, wall effects, vortex entrainment, particle-to-particle interactions and agglomeration. Liu et al. [30] suggested that for simulating the vortex structure of a highly swirling flow inside the cyclone separator a SIMPLEC algorithm using RSM could be used to simulate the turbulent anisotropic behavior of a complex three-dimensional flow field. The Reynolds Stress Model (RSM) was selected to simulate the strongly swirling turbulent flow in the annular space of a cyclone separator by Xue et al. [31]. They concluded that the predictions with the Reynolds Stress Model (RSM) are in reasonable agreement with experimental results, and it reveals that the RSM is suitable for investigating the flow of cyclone separators. Numerical simulation of the swirling flows in a cyclone separator was performed in [32] using a large eddy simulation (LES) based on a Smagorinsky model. Moreover,

particle motions are treated by a Lagrangian method and are calculated with a one-way coupling. The effect of particle separation was predicted from the results of the particle tracing. It was found that the LES has sufficient accuracy to predict the complicated swirling flows in the cyclone separator.

### **1.3 Thesis goals and contents**

The gas flow in the cyclone separator is turbulent, and this creates a complication when using CFD. With direct numerical simulation (DNS) such CFD simulation were already carried out in small, simple geometries. This field is advancing fast as the computational power increases. However, with currently processing equipment, this is not possible yet. Therefore turbulence models are required. A recent turbulence model technique is Large Eddy Simulation (LES). Therefore, LES has been implemented in the MISTRAL/PartFlow-3D code developed within our multiphase research group. The MISTRAL/PartFlow-3D code is divided into two solvers. The first one is the flow solver for the continuous flow. The second one is concerning the tracking of the individual particles. Briefly speaking, large eddies, which are mostly responsible for anisotropy in turbulence, are simulated directly in the LES model. Furthermore, the effect of the smaller eddies is accounted for in a simple turbulence model. Thus this is an intermediate step towards direct turbulence modelling. The particles motion has been modeled with a Lagrangian particle tracking approach. However, the movement of a single particle is followed, solving its equation of motion as it is tracked through the gas flow field. Therefore, the effect of the gas on the motion of the particle is calculated directly.

In this thesis two different cyclone separators with a geometrical swirl number of

$S_g = 3.5$  and 4 are studied. The geometric swirl number  $S_g$  is a measure for the ratio of tangential to axial momentum [33]. Predictions of the flow pattern, pressure drop and the separation efficiency in the cyclone separator are estimated by using CFD and particularly Large Eddy Simulation (LES). For that, the specific goals of the work are the following:

- Implementation of a sub-grid scale model for LES into the framework of the 3-dimensional computer simulation package MISTRAL/PartFlow-3D.
- Validation of the program modified for a straight square channel flow.
- Study cases with various cyclone geometries.
- Calculation of the velocity profiles at various axial positions.
- Investigation of the separation area between the cyclone apex cone and the dust collector.
- Investigation of particle trajectories.
- Calculation of the pressure drop that can be expected for a given design and for various operating conditions.
- Calculation of cyclone separation efficiency.

This thesis is organized into five chapters. After an introduction and overview, chapter 2 deals with continuous phase flow turbulence modeling including the governing equations. The emphasis lies on the LES model. Furthermore, the disperse phase motion is treated in chapter 3. Chapter 4 contains the validation process of the LES implementation with a channel flow. Moreover, prediction profiles of the

gas flow and disperse phase flow results are presented and discussed such as particle trajectories, cyclone separation efficiency, and pressure drop. Chapter 5 summarizes and concludes the thesis.

# Chapter 2

## Continuous phase flow computation

### 2.1 Introduction

Since the early days of computers, fluid flows governed by the Navier-Stokes equations have been solved numerically. Turbulence is the property of fluid flow that makes it a computational challenge. Turbulent fluid motion is an irregular condition of flow in which the various quantities show a random variation with time and space coordinates. Turbulent flows can be characterized as follows:

- Turbulent flows are highly unsteady. The behavior of the flow variables seems to be random as a function of time at a constant point and as a function of space at an instant moment of time.
- Turbulent flows are three-dimensional. Large scales may have two-dimensional features, but the smallest scales are three-dimensional.
- Turbulent flows contain a lot of vorticity. The process of stretching the vorticity is important in increasing the intensity of turbulence.

- Turbulent flows are highly dissipative, viscous forces dissipate kinetic energy into heat.
- Turbulent flows contain a broad spectrum. The length scale of the largest eddies is of the order of the size of the flow geometry, the smallest scale is of the order of the viscous size, the Kolmogorov length scale.
- Turbulent flows mix much stronger than laminar flows. This is due to the active motion of the fluid, which greatly enhances friction and heat.

Computationally, the direct solution of the Navier-Stokes equations is a very intensive task . It is performed mainly for academic purposes. Traditionally, turbulent flows have been computed with Reynolds-averaged Navier-Stokes (RANS) equations. The flow is averaged over a time to obtain a statistically steady flow. With the increased computer power, Large Eddy Simulation (LES) has become more and more popular. In LES the large-scale motion is resolved and the small scales are modeled. This approach is based on the idea that the large-scale motion is highly dependent on boundary conditions but small-scale motion is assumed to be relatively universal everywhere. The equations are filtered in space and the division into the large and small-scale motion is dependent on the length of the filter. For most engineering computations LES is too expensive today.

All of the methods described in this chapter require the solution of some form of the conservation equations for mass and momentum. The major difficulty is that turbulent flows contain variations on a much wider range of length and time scales than laminar flows.

## 2.2 Turbulent scales

Turbulence is a non-equilibrium phenomenon. The energy is fed constantly at the large scales by forces present in the mean flow. The energy is transferred to smaller vortices mainly by vortex-stretching processes. Eventually the viscous forces dissipate the kinetic energy into the internal energy of the fluid. Between the large scales and the small scales, there exists a range where neither of the processes is important. This is called the inertial sub-range. The energy distribution in the turbulent flow is described in terms of wave numbers. The velocity field can be represented as a Fourier series:

$$u(\vec{x}) = \sum_{\vec{k}} \hat{u}(\vec{k}) e^{i\vec{k}\cdot\vec{x}} \quad (2.2.1)$$

where  $\vec{k}$  is the wave vector. The energy spectrum becomes then

$$E(k) = \frac{1}{2} \hat{u}(k) \hat{u}^*(k) \quad (2.2.2)$$

where  $k = |\vec{k}|$  and an asterisk denotes the complex conjugate of a quantity. Geometrically interpreted  $E(k)dk$  is the amount of energy in a spherical shell with a radius of  $k$  and a thickness of  $dk$ . All the energy that is created is dissipated in the viscous range. As there is no production or dissipation in the inertial range, Kolmogorov [34] argued on dimensional grounds that

$$E(k) = K_0 \varepsilon^{2/3} k^{-5/3} \quad (2.2.3)$$

where  $\varepsilon$  is the rate of dissipation and  $K_0$  is the Kolmogorov constant, whose value has been deduced from measurements to lie in the range 1.4 - 2.2. In turbulent flows, a wide range of scales is present. The largest scales are about the same magnitude as

the geometry of the flow. In the boundary layer, the largest eddies are proportional to the thickness of the boundary layer. The dissipation rate at which the energy is cascaded into smaller vortices is the energy contained in large eddies per unit mass divided by their characteristic time scale.

$$\varepsilon \propto u'^2 / \left(\frac{l}{u'}\right) = \frac{u'^3}{l} \quad (2.2.4)$$

Here,  $u'$  is a characteristic root mean square value of the fluctuations and  $l$  is the integral scale. The energy dissipated directly from the large eddies is obtained by dividing by the viscous time scale  $u'^2 / (l^2 / \nu) = \nu u'^2 / l^2$ , which is small compared to  $\varepsilon$  in Eq. 2.2.4. The smallest scales of motion adjust themselves to the value of the viscosity. As the small-scale motions have small time scales they are statistically quite independent of the mean flow and slower large-scale motion. With that assumption, the small-scale motion should depend only on the rate of the energy transfer from the large scales and on the kinematic viscosity. The following scales are referred to as Kolmogorov micro scales of length  $\eta$ , time  $\tau$  and velocity  $v$

$$\eta \equiv (\nu^3 / \varepsilon)^{1/4} \quad (2.2.5)$$

$$\tau \equiv (\nu / \varepsilon)^{1/2}$$

$$v \equiv (\nu \varepsilon)^{1/4}$$

The Reynolds number at the micro scale level  $\eta v / \nu$  is equal to one, which indicates that the small-scale motion is quite viscous. By substituting  $\varepsilon$  in Eq. 2.2.4 into Eq. 2.2.5, the relations between the smallest and largest scales are obtained in [35]:



$$\eta/l \equiv (u'l/\nu)^{-3/4} = \text{Re}_l^{-3/4} \quad (2.2.6)$$

$$\tau/t \equiv (u'l/\nu)^{-1/2} = \text{Re}_l^{-1/2}$$

$$v/u \equiv (u'l/\nu)^{-1/4} = \text{Re}_l^{-1/4}$$

As the Reynolds number increases, so does the gap between the smallest and the largest scales. The Kolmogorov energy spectrum is shown in Figure 2.1

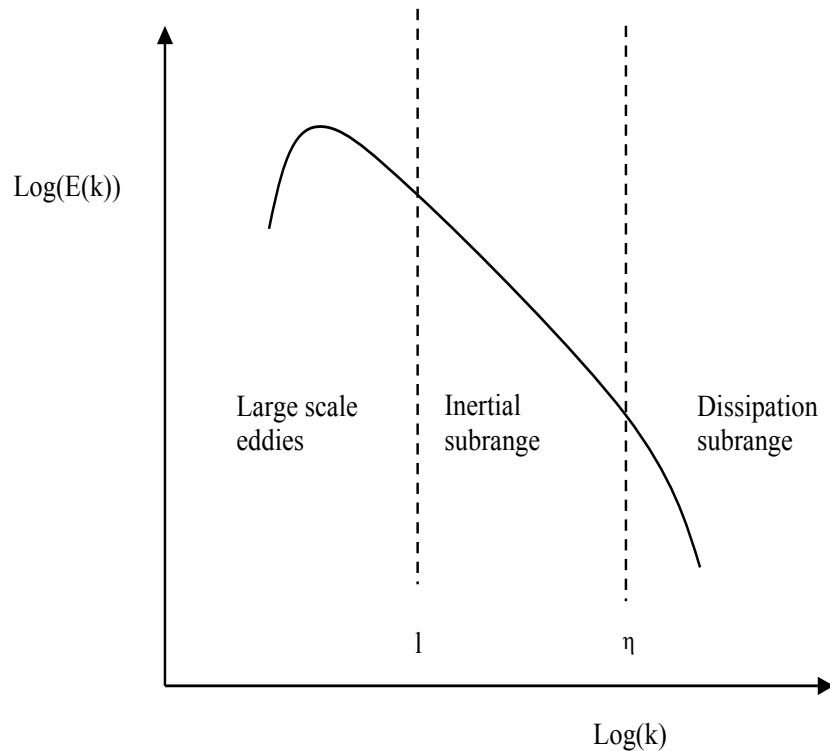


Figure 2.1: A sketch of the Kolmogorov energy spectrum of homogeneous turbulence. The straight section of the curve between the integral scale  $l$  and the viscous micro scale  $\eta$  has a slope of  $-5/3$ .

## 2.3 Governing equations

The following section deals with an Eulerian approach for the prediction of 3-dimensional gas flows and its application to flow simulation in cyclone separators. The flow was assumed as unsteady, incompressible and isothermal. The momentum balance equations can then be written in conservative form as follows [36]:

$$\frac{\partial K}{\partial t} + \frac{\partial (F - F_v)}{\partial x} + \frac{\partial (G - G_v)}{\partial y} + \frac{\partial (H - H_v)}{\partial z} = S^p \quad (2.3.1)$$

with  $S^p$  being the source term. The inviscid fluxes are

$$K = \begin{pmatrix} \rho \\ \rho u \\ \rho v \\ \rho w \end{pmatrix} \quad F = \begin{pmatrix} \rho u \\ \rho u^2 + p \\ \rho v u \\ \rho w u \end{pmatrix} \quad G = \begin{pmatrix} \rho v \\ \rho u v \\ \rho v^2 + p \\ \rho w v \end{pmatrix} \quad H = \begin{pmatrix} \rho w \\ \rho u w \\ \rho v w \\ \rho w^2 + p \end{pmatrix} \quad (2.3.2)$$

Here,  $\rho$  is the density,  $\vec{V} = u\vec{i} + v\vec{j} + w\vec{k}$  the velocity vector and  $p$  the pressure.

The viscous fluxes are;

$$F_v = \begin{pmatrix} 0 \\ \tau_{xx} \\ \tau_{xy} \\ \tau_{xz} \\ u\tau_{xx} + v\tau_{xy} + w\tau_{xz} \end{pmatrix} \quad G_v = \begin{pmatrix} 0 \\ \tau_{xy} \\ \tau_{yy} \\ \tau_{yz} \\ u\tau_{xy} + v\tau_{yy} + w\tau_{yz} \end{pmatrix}$$

$$H_v = \begin{pmatrix} 0 \\ \tau_{xz} \\ \tau_{yz} \\ \tau_{zz} \\ u\tau_{xz} + v\tau_{yz} + w\tau_{zz} \end{pmatrix} \quad (2.3.3)$$

with the viscous stress tensor

$$\tau_{ij} = \mu \left[ \left( \frac{\partial u_j}{\partial x_i} + \frac{\partial u_i}{\partial x_j} \right) - \frac{2}{3} (\nabla \cdot \vec{V}) \delta_{ij} \right] \quad (2.3.4)$$

Here,  $i, j$  are indices for  $x, y, z$  and  $\delta_{ij}$  is the Kronecker delta defined such that  $\delta_{ij} = 1$  if  $i = j$  and  $\delta_{ij} = 0$  otherwise and  $\mu$  the molecular viscosity. For incompressible and isothermal flows with constant properties, Eq. 2.3.1 is reduced to the conservation equations for continuity and momentum:

$$\frac{\partial \rho}{\partial t} + \frac{\partial \rho u_i}{\partial x_i} = 0 \quad (2.3.5)$$

$$\frac{\partial u_i}{\partial t} + \frac{\partial u_i u_j}{\partial x_j} = -\frac{1}{\rho} \frac{\partial p}{\partial x_i} + \frac{\mu}{\rho} \frac{\partial^2 u_i}{\partial x_j \partial x_j} \quad (2.3.6)$$

where  $p$  is the pressure. Note that we use the summation convention. This means that a repeated subscript indicates summation over that subscript.

### 2.3.1 Reynolds-Averaged Navier-Stokes Models

In Reynolds-average models, all of the unsteadiness is averaged out i.e. all unsteadiness is regarded as part of the turbulence. By this way, the nonlinearity of the Navier-Stokes (NS) equations leads to terms that must be modeled. Due to the complexity of turbulence no Reynolds-average model exists which can be used to simulate

all turbulent flows. In a statistically steady flow, every variable can be written as the sum of a time averaged value and a fluctuation about that value:

$$u(x_i, t) = \bar{u}(x_i) + u'(x_i, t) \quad (2.3.7)$$

where

$$\bar{u}(x_i) = \lim_{T \rightarrow \infty} \frac{1}{T} \int_0^T u(x_i, t) dt. \quad (2.3.8)$$

Here  $t$  is the time and  $T$  is the averaging interval. This interval must be large compared to the typical time scale of the fluctuations.

The result of applying Eqs. 2.3.7 and 2.3.8 to the Navier-Stokes equations are the Reynolds-average Navier-Stokes (RANS) equations. From Eq. 2.3.7, it follows that  $\overline{u'}$  is zero. Thus, averaging any linear term in conservation equations simply gives the identical term for the average quantity.

From a quadratic nonlinear term we get two terms, the product of the average and a covariance:

$$\overline{u_i u_j} = \overline{(\bar{u}_i + u'_i)(\bar{u}_j + u'_j)} = \bar{u}_i \bar{u}_j + \overline{u'_i u'_j} \quad (2.3.9)$$

As a result, the conservation equations contain terms such as  $\overline{\rho u'_i u'_j}$ , called the *Reynolds stresses*. These can not be represented uniquely in terms of the mean quantities. The averaged continuity and momentum equations can, for incompressible flows without body forces, be written in tensor notation as [37]:

$$\frac{\partial (\rho \bar{u}_i)}{\partial x_i} = 0 \quad (2.3.10)$$

$$\frac{\partial(\rho\bar{u}_i)}{\partial t} + \frac{\partial}{\partial x_j} \left( \rho\bar{u}_i\bar{u}_j + \overline{\rho u'_i u'_j} \right) = -\frac{\partial\bar{p}}{\partial x_i} + \frac{\partial\bar{\tau}_{ij}}{\partial x_j} \quad (2.3.11)$$

where the  $\bar{\tau}_{ij}$  are the mean viscous stress tensor components:

$$\bar{\tau}_{ij} = \mu \left( \frac{\partial\bar{u}_i}{\partial x_j} + \frac{\partial\bar{u}_j}{\partial x_i} \right) \quad (2.3.12)$$

The presence of the Reynolds stresses in the conservation equations means that the latter are not closed. Hence, they contain more variables than number of equations. Closures require some approximations, which usually take the form of prescribing the Reynolds stress tensor in terms of the mean quantities. It is possible to derive equations for the higher order correlations e.g., for the Reynolds stress tensor, but these contain still more and higher order unknown correlations that require modeling approximations. The approximations introduced are called *turbulence models*.

In order to solve the Reynolds equations it is necessary to apply turbulence models for the Reynolds stresses approximation. The commercial code CFX-4.4 provides several options of turbulence models, which have been tested and compared: the  $k - \epsilon$  model and the Reynolds stress turbulence model (RSM) of Launder et al. [38]. The  $k - \epsilon$  model is an eddy-viscosity model that is simple, numerically robust and fast converging. However, it is known to generate poor results for highly swirling flow as in the case of cyclones where turbulence is anisotropic. As an alternative, RSM can be used which solves the equations for the individual Reynolds stress components. The RSM model is on one hand a more fundamental approach to the modeling of turbulence than the eddy-viscosity models but is on the other hand more complex and thus computationally expensive and may cause stability problems. Both the  $k - \epsilon$  and RSM (RANS models) were used in the steady state mode.

For the second CFD code used later on for computations (MISTRAL-3D), only Large-Eddy Simulations and no RANS-models will be used.

### 2.3.2 Standard $k - \epsilon$ turbulence model

The  $k - \epsilon$  turbulence model uses the gradient diffusion hypothesis to relate the Reynolds stresses to the mean velocity gradients and the turbulent viscosity. The turbulent viscosity is modeled as the product of a turbulent velocity and length scale. In  $k - \epsilon$  the turbulent velocity scale is computed from the turbulent kinetic energy, which is provided from the solution of its transport equation. The turbulent length scale is estimated from the turbulent kinetic energy and its dissipation rate. The dissipation rate of the turbulent kinetic energy is provided from the solution of its transport equation.

The  $k - \epsilon$  model introduces two new variables into the system of equations. The momentum equation is then:

$$\frac{\partial \rho u_i}{\partial t} + \frac{\partial \rho u_i u_j}{\partial x_j} = \frac{\partial p'}{\partial x_i} + \frac{\partial}{\partial x_j} \left( \mu_{eff} \frac{\partial u_i}{\partial x_j} \right) \quad (2.3.13)$$

where  $\mu_{eff}$  is the effective viscosity accounting for turbulence,

$$\mu_{eff} = \mu + \mu_t \quad (2.3.14)$$

and  $p'$  is the modified pressure given by

$$p' = p + \frac{2}{3} \rho k \quad (2.3.15)$$

where  $\mu_t$  is the turbulent viscosity. The  $k - \epsilon$  model assumes that the turbulence viscosity is linked to the turbulence kinetic energy and dissipation via the relation

$$\mu_t = \rho c_\mu \frac{k^2}{\varepsilon} \quad (2.3.16)$$

The values for  $k - \varepsilon$  come directly from the differential transport equations for the turbulent kinetic energy and the turbulence dissipation rate [39]. For a steady flow:

$$\frac{\partial}{\partial x_j} (\rho u k) = \frac{\partial}{\partial x_j} \left[ \left( \mu + \frac{\mu_t}{\sigma_k} \right) \frac{\partial k}{\partial x_j} \right] + P_k - \rho \varepsilon \quad (2.3.17)$$

$$\frac{\partial}{\partial x_j} (\rho u \varepsilon) = \frac{\partial}{\partial x_j} \left[ \frac{\mu_t}{\sigma_\varepsilon} \frac{\partial \varepsilon}{\partial x_j} \right] + \frac{\varepsilon}{k} (c_{\varepsilon 1} P_k - c_{\varepsilon 2} \rho \varepsilon) \quad (2.3.18)$$

The production term has the form

$$P_k = \mu_t \left\{ 2 \cdot \left[ \left( \frac{\partial u}{\partial x} \right)^2 + \left( \frac{\partial v}{\partial y} \right)^2 + \left( \frac{\partial w}{\partial z} \right)^2 \right] + \left( \frac{\partial u}{\partial y} + \frac{\partial v}{\partial x} \right)^2 + \left( \frac{\partial u}{\partial z} + \frac{\partial w}{\partial x} \right)^2 + \left( \frac{\partial w}{\partial y} + \frac{\partial v}{\partial z} \right)^2 \right\} \quad (2.3.19)$$

The constants of the  $k - \varepsilon$  model [39] are

$$c_\mu = 0.09 , \quad c_{\varepsilon 1} = 1.44 , \quad c_{\varepsilon 2} = 1.92 , \quad \sigma_k = 1.0 , \quad \sigma_\varepsilon = 1 \quad (2.3.20)$$

The RANS equations have the same form as the laminar equations provided the molecular viscosity,  $\mu$ , is replaced by the effective viscosity  $\mu_{eff} = \mu + \mu_t$ . The most important difference is that two new partial differential equations need to be solved. As the time scales encountered with the turbulence are much shorter than those connected with the mean flow, the  $k - \varepsilon$  equations are much stiffer than the laminar equations. The profiles of the turbulent kinetic energy and its dissipation are typically much more peaked near the wall than the mean velocity profile. These

peaks are difficult to capture. Therefore a finer grid for the turbulence quantities has to be applied near the wall than for the mean flow.

Boundary conditions are needed for the model equations. However, at solid walls there may be significant differences. In  $k - \epsilon$ , it is appropriate to set  $k = 0$  at the wall but the dissipation is not zero there; instead one can use the conditions:

$$\frac{\partial \epsilon}{\partial n} = 0 \quad (2.3.21)$$

where  $n$  is the coordinate normal to the wall. When this is done, it is necessary to modify the model itself near the wall. A number of modifications at low Reynolds numbers for the  $k - \epsilon$  model have been proposed by [40, 41].

At high Reynolds numbers, the viscous sublayer of a boundary layer is so thin that it is difficult to use enough grid points to resolve it. This problem can be avoided by using *wall functions*. The wall function is relying on the existence of a logarithmic region in the velocity profile. The log-law of the wall was used for the wall treatment following Launder and Spalding [42]:

$$u^+ = \frac{1}{\kappa} \ln(y^+) + C \quad (2.3.22)$$

where  $\kappa$  is the evaluated Kármán constant 0.38 and  $C = 4.1$  is the integration constant depending on the wall roughness [43].  $y^+$  is the dimensionless distance from the wall:

$$y^+ = \frac{u_t y}{\nu} \quad (2.3.23)$$

where  $u_t$  is the friction velocity, see Reference [42].



### 2.3.3 Reynolds Stress Model

Eddy viscosity models have significant deficiencies. In three-dimensional flows, the Reynolds stress and the strain rate may not be related in such a simple way. This means that the eddy viscosity may no longer be a scalar. Anisotropic models based on using  $k - \epsilon$  equations have been proposed in [44].

The most complex models in common use are Reynolds stress models which are based on dynamic equations for the Reynolds stress tensor itself. The exact transport equation for the Reynolds-stress tensor  $\overline{u_i u_j}$  is obtained from the momentum equation 2.3.6 by multiplying the instantaneous component  $u_i$  equation by the fluctuation velocity  $u'_i$ , adding the two and then time-averaging the result. The result can be written for constant-density flows neglecting body forces after some rearrangement as

$$\begin{aligned}
 \underbrace{\frac{\partial \overline{u'_i u'_i}}{\partial t}}_{C_{ij}} = & - \underbrace{\left( \overline{u'_i u'_k} \frac{\partial u_j}{\partial x_k} + \overline{u'_j u'_k} \frac{\partial u_i}{\partial x_k} \right)}_{P_{ij}} \\
 & - \underbrace{\frac{\partial}{\partial x_i} \left[ \overline{u'_i u'_j u'_k} + \frac{1}{\rho} \left( \overline{p' u'_i} \delta_{ij} + \overline{p' u'_j} \delta_{ik} \right) - \nu \frac{\partial \overline{u'_i u'_j}}{\partial x_k} \right]}_{D_{ij}} \\
 & + \underbrace{\frac{p'}{\rho} \left( \frac{\partial u_i}{\partial x_j} + \frac{\partial u_j}{\partial x_i} \right)}_{\phi_{ij}} - \underbrace{2\nu \left( \frac{\partial u_i}{\partial x_k} \frac{\partial u_j}{\partial x_k} \right)}_{\epsilon_{ij}}
 \end{aligned} \tag{2.3.24}$$

Here  $P_{ij}$  is the production of  $\overline{u'_i u'_j}$ ;  $\phi_{ij}$  is the pressure-strain term, which promotes isotropy of turbulence;  $\epsilon_{ij}$  is the dissipation (i.e. transformation of mechanical energy into heat in the small-scale turbulence) of  $\overline{u'_i u'_j}$ ;  $D_{ij}$  is the convection and diffusion of  $\overline{u'_i u'_j}$ . The pressure-strain term, which is an important term since its contribution is significant, is modeled according to Launder et al. [38]. The pressure-strain

correlation  $\phi_{ij}$  was split into two components that were given as

$$\phi_{ij,1} = -c_1 \frac{\epsilon}{k} (\overline{u_i u_j} - \frac{2}{3} \delta_{ij} k) \quad (2.3.25)$$

$$\phi_{ij,2} = -c_2 \frac{\epsilon}{k} (P_{ij} - \frac{2}{3} \delta_{ij} P_k) \quad (2.3.26)$$

The constants for  $\phi_{ij}$  are

$$c_1 = 1.8, c_2 = 0.6 \quad (2.3.27)$$

In three dimensions, this model requires the solution of seven partial differential equations in addition to the equations for the mean flow. These equations are solved in a manner similar to that for the  $k - \epsilon$  equations and even more care is required in their solution.

There is no doubt that the Reynolds stress model has greater potential to represent turbulent flow phenomena more correctly than the  $k - \epsilon$  model. Excellent results have been obtained in [36] for some flows in which the  $k - \epsilon$  types of models are known to perform badly; however, in some flows their performance is not better at all (e.g., swirling flows, flows with strong curvature and with separation from curved surfaces, etc.).

## 2.4 Large Eddy Simulation model (LES) and Smagorinsky model

Solving the unsteady Navier-Stokes equation implies that we must take into account all the space-time scales if we want to have a result of maximum quality. The discretization has to be fine enough to represent all these scales numerically. Hence, the simulation is discretized in steps  $\Delta x$  in space and  $\Delta t$  in time that must be smaller than the characteristic length and the characteristic time encountered with the smallest scale of the exact solution. This solution criterion is extremely constrictive when the solution to the exact problem contains scales with wide range of sizes. This can be demonstrated with the simplest turbulent flow case (homogenous and isotropic). For this case, the ratio between the characteristic length of the most energetic scale,  $L$ , and that of the smallest dynamically active scale,  $\eta$ , is calculated by the relation:

$$\frac{L}{\eta} = O\left(\text{Re}^{3/4}\right) \quad (2.4.1)$$

We therefore need  $O\left(\text{Re}^{9/4}\right)$  degree of freedom in order to be able to represent all the scales in a cubic volume of edge length  $L$ . In order to calculate the evolution of the solution in a volume for a duration equal to the characteristic time of the most energetic scale, we have to solve the Navier-Stokes equations numerically  $O(\text{Re}^3)$  times. This type of computation for large Reynolds numbers requires computer resources very much greater than currently available supercomputer capacities. Therefore, this is not practical.

Turbulent flows contain a wide range of length and time scales. The large scale motions are generally much more energetic than the small scales; their size and strength

make them by far the most effective transporters of the conserved properties. The small scales are usually much weaker and provide little transport of these properties. Large Eddy Simulation (LES) treats the large eddies more exactly than the small ones. In LES, we calculate the large scales in space directly as illustrated in Figure 2.2.

The scale selection on which the LES technique is based [45, 46, 47, 48] is a separation between large and small scales. A cutoff length first has to be determined. Those scales that are of a characteristic size greater than the cutoff length are called large or resolved scales, and others are called small or subgrid scales. The subgrid scales are included by way of a model called subgrid model.

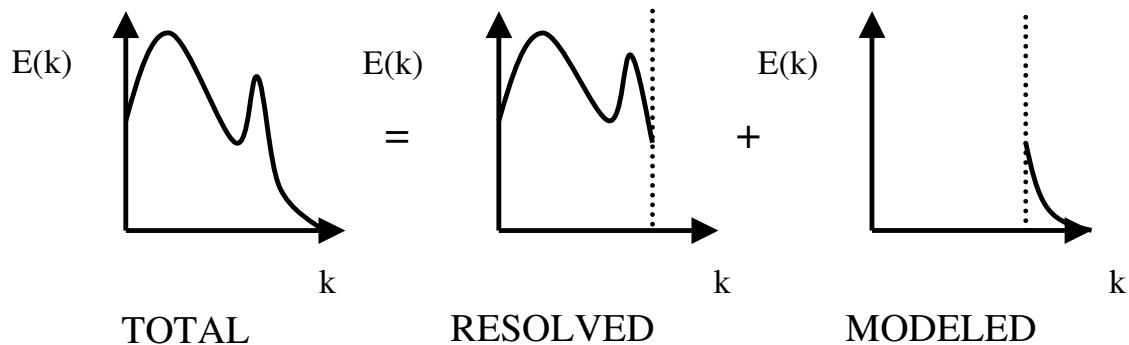


Figure 2.2: Decomposition of the energy spectrum in the solution encountered with large eddy simulation [45].

The LES requires the separation of small eddies from large eddies with a filter. For the sake of simplicity, the following section uses one-dimensional notations. It is essential to define the quantities to be computed precisely. We need a velocity field

that contains only the large scale components of the total field. This is best done by filtering [49]. In one-dimension, the filtered velocity is defined by:

$$\bar{u}_i = \int G(x, x') u_i(x) dx' \quad (2.4.2)$$

where  $G(x, x')$  is a filter function. The filter function is large where  $G(x, x')$  is less than the filter width  $\Delta$ , a length scale, over which the averaging is performed. Flow eddies larger than the filter width are defined as "large eddies" and smaller than this width as "small eddies". Two convolution filters are ordinarily used for performing the spatial separation. For a cutoff length  $\bar{\Delta}$ , in the one-dimensional case, these are the:

- Box or top-hat filter:

$$G(x_i) = \left\{ \begin{array}{ll} \frac{1}{\Delta_i} & |x_i| \leq \frac{\Delta_i}{2} \\ 0 & |x_i| > \frac{\Delta_i}{2} \end{array} \right\} \quad (2.4.3)$$

- Gaussian filter:

$$G(x) = \left( \frac{\gamma}{\pi \Delta^2} \right)^{1/2} \exp \left( \frac{-\gamma |x|^2}{\Delta^2} \right) \quad (2.4.4)$$

The convolution kernel  $G$  of eq. 2.4.3 is represented in the upper part of Figure 2.3.  $\gamma$  is a constant generally taken to be equal to 6 [36]. The convolution kernel  $G$  of eq. 2.4.4 is presented in the lower part of Figure 2.3.

Using the finite volume method, it seems natural to define the filter width,  $\Delta_i$ , as an average over a grid volume. With the filter, it is possible to derive the governing conservation equations for the momentum (Navier-Stokes equations), and mass continuity. The filtered Navier-Stokes equations for an incompressible flow are:

$$\frac{\partial \bar{u}_i}{\partial x_i} = 0 \quad (2.4.5)$$

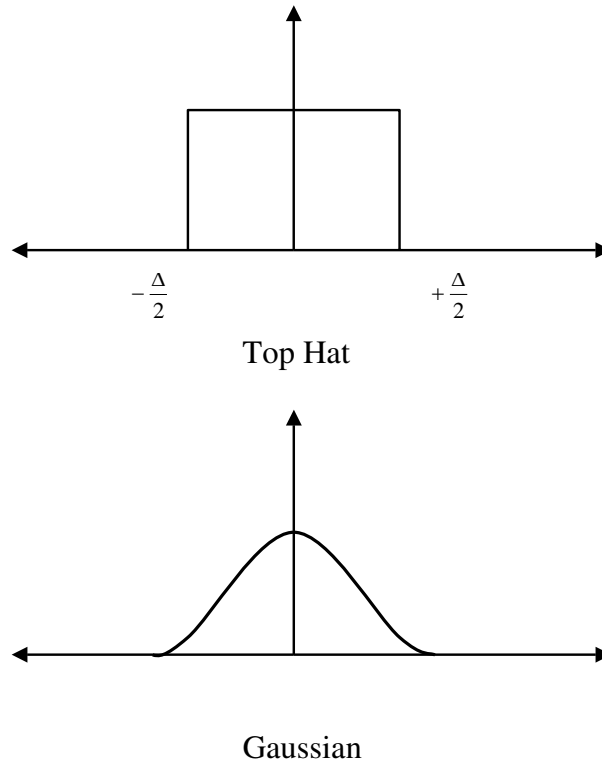


Figure 2.3: Commonly used filter kernels.

$$\frac{\partial \bar{u}_i}{\partial t} + \frac{\partial}{\partial x_j} (\overline{u_i u_j}) = -\frac{\partial \bar{p}}{\partial x_i} + \frac{1}{\text{Re}} \frac{\partial^2 \bar{u}_i}{\partial x_j \partial x_j} - \frac{\partial \tau_{ij}}{\partial x_j} \quad (2.4.6)$$

Since the continuity equation is linear, filtering does not change it significantly. Eqs. 2.4.5-2.4.6 govern the evolution of the large scales. The effects of the small scales appear in the subgrid-scale stresses,

$$\tau_{ij} = \overline{u_i u_j} - \bar{u}_i \cdot \bar{u}_j \quad (2.4.7)$$

that must be modeled. Most of the existing models are of the eddy viscosity type:

they assume proportionality between the anisotropic part of the Sub Grid Scale (SGS) stress tensor,

$$\tau_{ij}^a = \tau_{ij} - \delta_{ij}\tau_{kk}/3 \quad (2.4.8)$$

and the large-scale strain rate tensor,  $\overline{S}_{ij}$  :

$$\tau_{ij}^a = -2\nu_t\overline{S}_{ij} = -\nu_t \left( \frac{\partial\overline{u}_i}{\partial x_j} + \frac{\partial\overline{u}_j}{\partial x_i} \right) \quad (2.4.9)$$

The first SGS model was proposed by Smagorinsky [50] in 1963. It is based on the Boussinesq eddy-viscosity approximation that relates the turbulent shear stresses linearly to the strain rates. Equilibrium turbulence and isotropic sub-grid scales are assumed. Thus one can write

$$\tau_{ij} = -\frac{\mu_t}{\rho}\overline{S}_{ij} \quad (2.4.10)$$

where  $\mu_t$  is the eddy viscosity and  $\overline{S}_{ij}$  is the strain rate of the large scale field. This model can be derived by equating production and dissipation of subgrid turbulent kinetic energy or through turbulence theories. The form of the subgrid scale eddy viscosity can be derived by dimensional arguments and is:

$$\mu_t = C_s^2\rho\Delta^2|\overline{S}| \quad (2.4.11)$$

where  $C_s$  (termed Smagorinsky constant) is a model parameter to be determined,  $\Delta$  is the filter length scale, and  $|\overline{S}| = (\overline{S}_{ij}\overline{S}_{ij})^{1/2}$ . This form of the model can also be derived in a number of different ways. Theories provide estimates of the parameter. Most of these methods can be applied only to isotropic turbulence for which they all agree that  $C_s \approx 0.2$  . Unfortunately,  $C_s$  is in reality not constant; it may be

a function of the Reynolds number and other non-dimensional parameters and may take different values in different flows. The Smagorinsky model, although relatively successful, is not without problems. For example, to simulate channel flow, several modifications are required. The value of the parameter  $C_s$  in the bulk of the flow has to be reduced from 0.2 to approximately 0.065 [36] or to 0.1 in [51, 52], which reduces the eddy viscosity by almost an order of magnitude.

In the near-wall region, where the motion is mainly governed by molecular viscosity, the contribution of the model has to be damped. Therefore, a wall damping function has been applied in the form [42]

$$f_\mu = 1 - \exp \left[ - \left( \frac{y^+}{A^+} \right)^3 \right] \quad (2.4.12)$$

with  $A^+ = 25$  being the so-called *van Driest factor* [53] and  $y^+$  a dimensionless wall-coordinate defined by

$$y^+ = \frac{u_\tau y}{\nu} \quad (2.4.13)$$

The purpose of the van Driest damping factor is to reduce the subgrid scale eddy viscosity near the wall;  $\mu_t \propto y^3$  in this region. An alternative is a subgrid scale model which reduces the eddy viscosity when the subgrid scale Reynolds number,  $|\overline{S}| \Delta^2/\nu$ , becomes small. Models of this kind were suggested in [54, 55].

An additional problem is that near the wall the flow structure is very anisotropic. Regions of low and high speed fluid (streaks) are created; they are approximately 1000 viscous units long and 30-50 viscous units wide in both the spanwise and normal directions. Resolving the streaks requires a highly anisotropic grid and the choice of length scale,  $\Delta$ , to use in the SGS model is not obvious. The usual choice is



$(\Delta_1\Delta_2\Delta_3)^{1/3}$  but  $(\Delta_1^2 + \Delta_2^2 + \Delta_3^2)^{1/2}$  is possible. It is possible that with the proper choice of length scale, the damping would become unnecessary. Further details related to this issue can be found in [56]. In cyclone flows in which rotation and curvature play significant roles, it is necessary to reduce the Smagorinsky constant as shown in [13].

## 2.5 Solution algorithm

Navier Stokes equations are solved using two different codes (a commercial one (CFX 4.4) [57], and a research code (MISTRAL-3D)) based on a pressure correction algorithm of the SIMPLE method.

CFX 4.4 is a finite-volume based code that solves the conservation equations for mass, momentum, and energy in three dimensions. It employs a so-called block-structured grid to define the geometrical domain. Thus the geometry is composed of a number of blocks, which are glued together. A body-fitted Cartesian co-ordinate system is used. A more detailed description of the mathematical models can be found in the solver manual documentation [57].

The research program package called MISTRAL-3D [58] is based on a Finite Volume Method (FVM) discretization on colocated, block-structured numerical grids. This method is developed by Schreck and Perić [59]. The most fundamental points of MISTRAL-3D are:

1. The flow solver is a finite volume code working on a block-structured hexahedral grid.
2. The basic solving method of the flow solver is the SIMPLE method [60]. This

means, the equation for momentum and a pressure correction equation are iterated one after the other in an outer iteration cycle.

3. For the inner iterations the Strongly Implicit Procedure (SIP) solver is used [61]. Up to 5 inner iterations are sufficient for most problems, except for the pressure correction equation, which needs a much higher number of SIP iterations (up to 500).
4. The high number of SIP iterations for the pressure correction equation can be reduced using a multigrid iteration for this equation. It tends to a strong improvement of the efficiency of the SIMPLE algorithm [62].
5. Full parallelization using the domain decomposition method, parallelization based on standard libraries like PVM and MPI.

In this chapter the computations of continuous phase flow with three turbulence models have been presented. The emphasis was based on LES modelling. The computations of disperse phase motion is presented in the following chapter. This computations are based on Euler-Lagrangian approach.

# Chapter 3

## Dispersed Phase Motion

### 3.1 Introduction

In this chapter we present the Euler-Lagrange method that is suitable for disperse flows such as in the cyclone separators. The method bears its name from the fact that the continuous phase flow is treated in an Eulerian manner while the disperse phase flow is treated in a Lagrangian manner. In the Eulerian approach the flow variables are a function of space and time, thus are represented as fields. In the Lagrangian approach instead individual particles are considered and the position and velocity of each particle is a function of time only. Therefore, in the Euler-Lagrange approach mass and momentum conservation equations are solved for the continuous phase. For the disperse phase, the position and velocity of each particle is obtained from Newton's second law. This requires the interpolation of the continuous phase velocity from the Eulerian grid to the local particle position. For flows involving a small number of dispersed particles it is possible to solve a set of Lagrangian equations for every element. However, if the number of particles is large, a statistical approach is more practical. Hence, discrete particle trajectories are calculated. Each calculated particle

represents a large number of physical particles of the same physical properties, which is characterized by the particle flow rate  $\dot{N}_p$  along each calculated particle trajectory.

## 3.2 Coupling between phases

The Euler-Lagrange method can be classified with respect to the kind of coupling between the phases. The simplest approach is one-way coupling. In a *one-way* coupled system the particle mass loading respectively volume-loading is assumed to be small enough so that any effects which the presence of the dispersed phase may have on the continuous phase can be neglected. Thus, only the local velocity of the continuous phase has a direct impact on the particle motion. If the effects of the particles on the carrier fluid can not be ignored *two-way* coupling is required. Additionally, *four-way* coupling takes into account the particle-particle collision effects due to higher void fraction of the dispersed phase and due to turbulence modification by the particles.

## 3.3 Classification parameters of gas-particle flows

Gas-Particle flows can be classified by characteristic parameters. The first important parameter is the mass loading  $\eta$ . The mass loading is the ratio of mass flux of the dispersed phase to that of the continuous phase,

$$\eta = \frac{\dot{m}_P}{\dot{m}_F} \quad (3.3.1)$$

A further important parameter is the volume fraction  $\alpha$ . Here,  $\alpha_P$  is the volume fraction of the dispersed phase (particles) and  $\alpha_F = 1 - \alpha_P$  the volume fraction of the continuous phase (fluid). The mixture density  $\sigma$  of a phase is the mass of this phase

per unit volume of the phase mixture. The mixture density for the particle phase is determined as follows:

$$\sigma_P = \alpha_P \rho_P \quad (3.3.2)$$

Similarly, the mixture density of the fluid is,

$$\sigma_F = (1 - \alpha_P) \rho_F \quad (3.3.3)$$

where  $\rho_F$  and  $\rho_P$  are the fluid and particle densities, respectively. The response time of a particle to changes in flow velocity is important in establishing nondimensional parameters to characterize the flow. The momentum response time is related to the time required for a particle to respond to a change in velocity [63]:

$$\tau_A = \frac{\rho_P d_P^2}{18\mu} \quad (3.3.4)$$

where  $d_P$  is the particle diameter and  $\mu$  is the molecular viscosity of the gas. As one can see, the momentum response time is most sensitive to the particle size [64]. A further important classification parameter is the *Stokes number*. The Stokes number concerned with the particle velocity is defined as

$$\text{St} = \frac{\tau_A}{\tau_S} \quad (3.3.5)$$

where  $\tau_S$  is the characteristic time of the flow field. If  $\text{St} \ll 1$ , the response time of the particles is much less than the characteristic time encountered with the flow. On the other hand, if  $\text{St} \gg 1$ , the particles will have basically no time to respond to the fluid velocity changes.

### 3.4 Euler-Lagrangian approach

In this section, the numerical modeling of the Lagrangian approach is presented. The disperse phase is regarded thereby as a quantity of discrete single particles, whose Lagrangian motion equations are numerically solved. In order to limit the cost of computation, the simulated particles regarded are generally less than the number of particles in the real systems. Each simulated particle represents therefore a certain number of physical particles with the same physical characteristics. The movement of an individual particle results from the forces and moments acting on this particle.

A particle moving in a flow field changes its movement as a result of outside forces. First, these forces are aerodynamic forces exerted by the fluid on the particle. Moreover there are body forces due to gravitation and electrical or magnetic forces. Also collision forces, which arise during the collision of the particle with a wall or with another particle, entail a change of the movement conditions of the particle. In this section first only the influence of the aerodynamic forces and the body forces on the particle movement is to be considered.

Equating the sum of the steady state drag forces, the pressure force, virtual mass force and body force to the mass  $m_P$  times the acceleration of an isolated particle yields the Basset-Boussinesq-Oseen (BBO) equation for particle motion.

$$m_P \frac{d\vec{v}_P}{dt} = \vec{F}_W + \vec{F}_M + \vec{F}_S + \vec{F}_G + \vec{F}_{VM} + \vec{F}_P + \vec{F}_B \quad (3.4.1)$$

where  $\vec{F}_W$  is the aerodynamic force,  $\vec{F}_M$  the lift force due to the particle rotation (Magnus force),  $\vec{F}_S$  the lift force due to shear in the fluid flow field (Saffman force),  $\vec{F}_G$  the gravitational force,  $\vec{F}_{VM}$  virtual mass force,  $\vec{F}_P$  the thrust force due to a pressure gradient of the continuous phase and  $\vec{F}_B$  Basset force.

The aerodynamic force  $\vec{F}_W$  results in a flow field on the particle due to the friction and pressure field. Friction resistance is caused by the conditions at the particle surface. The pressure conditions result from an uneven pressure distribution at the particle surface. The pressure effects on the side of the particle downstream is smaller than the upstream pressure. Hence, the resulting thrust force is directed against the particle movement. The equation for the determination of the aerodynamic force is,

$$\vec{F}_W = \frac{\pi}{8} \rho_F d_P^2 c_W v_{rel} \vec{v}_{rel} \quad (3.4.2)$$

where  $\vec{v}_{rel}$  is the relative velocity between fluid and particle:

$$\vec{v}_{rel} = \vec{v}_F - \vec{v}_P \quad (3.4.3)$$

and

$$v_{rel} = |\vec{v}_{rel}| = \sqrt{(u_F - u_P)^2 + (v_F - v_P)^2 + (w_F - w_P)^2} \quad (3.4.4)$$

The drag coefficient  $c_W$  is an empirical property depending on the particle Reynolds number:

$$Re_P = \frac{d_P v_{rel}}{\nu_F} \quad (3.4.5)$$

Here  $\nu_F$  is the kinematic viscosity of the fluid. For the determination of the drag coefficient numerous investigations were carried out [65, 66]. In this work the drag coefficient computation is based on Moris and Alexander [66].

The Magnus force  $\vec{F}_M$  is the lift developed due to rotation of the particle in the flow field as shown in Figure 3.1. The lift is caused by a pressure differential between

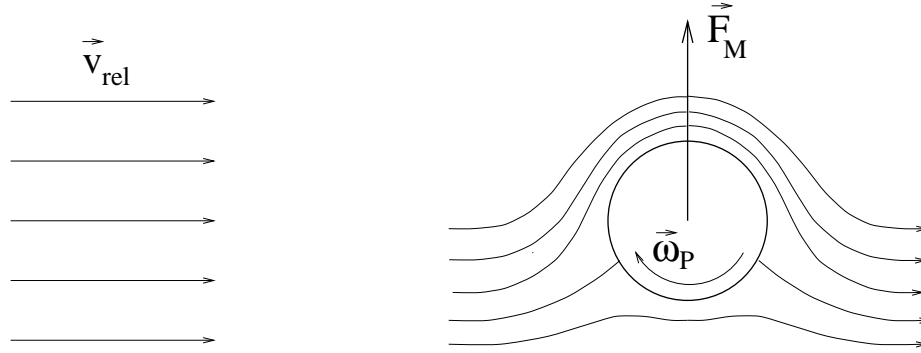


Figure 3.1: Transverse force on a rotating particle in a parallel flow.

both sides of the particle resulting from the velocity differential due to rotation. The rotation may be caused by other sources. A quite descriptive example is the tennis ball struck with topspin, which experiences thereby a strongly modified flight path. The size of the Magnus force depends also on the roughness of the surface of the particle, however the semi empirical factor  $c_M$  was developed for a hydraulically smooth ball.

The equation for the determination of the Magnus force defined in [67] is:

$$\vec{F}_M = \frac{\pi}{8} \rho_F d_P^2 c_M \frac{v_{rel}}{w_{rel}} (\vec{\omega}_{rel} \cdot \vec{v}_{rel}) \quad (3.4.6)$$

where  $\vec{\omega}_{rel}$  is the particle rotation relative to the fluid:

$$\vec{\omega}_{rel} = \vec{\omega}_F - \vec{\omega}_P \quad (3.4.7)$$

with

$$w_{rel} = |\vec{\omega}_{rel}| = \sqrt{(\omega_{Fx} - \omega_{Px})^2 + (\omega_{Fy} - \omega_{Py})^2 + (\omega_{Fz} - \omega_{Pz})^2} \quad (3.4.8)$$

The rotation of the fluid at the particle place results from (only valid for two-dimensional flows):



$$\vec{\omega}_F = \nabla \times \vec{v}_F = \frac{\partial v_F}{\partial x} - \frac{\partial u_F}{\partial y} \quad (3.4.9)$$

The Magnus force factor  $c_M$  has been determined by [68]:

$$c_M = \begin{cases} (0.4 \pm 0.1) \sigma_M & \text{for } \sigma_M < 1, \\ (0.4 \pm 0.1) & \text{for } \sigma_M \geq 1, \end{cases} \quad (3.4.10)$$

with

$$\sigma_M = \frac{1}{2} \frac{d_P \omega_{rel}}{v_{rel}} \quad (3.4.11)$$

If the rotation speed is sufficiently large, the Magnus force can significantly affect the particle movement. This case can particularly be observed for gas-particle flows in channels and pipes. However, it leads frequently to particle wall collisions. With particle wall collisions the friction between the particle surface and the wall is relatively large as the tangential force affects the particle surface. In the case of pneumatic transport of particles with a diameter of 0.5 - 1 mm in a rectangular channel e.g. rotation speeds of 300-2000 rad/s were measured by Matsumoto and Saito [69].

Since measurements for very small particles ( $d_p < 100\mu m$ ) are carried out with difficulty, the correlations for the factor  $c_M$  determined for large particles will be used for smaller particles too. Nevertheless the inertia of small particles with rotation is absorbed fast because of viscous forces around the particles.

If particles are placed in a shear flow, an uneven pressure distribution transverse to the direction of flow will develop along its surface. This is known as Saffman force, shown in Figure 3.2. Saffman deduced an analytic relationship for this force [70]:

$$F_S = 1.615\rho_F\sqrt{\nu_F}d_P^2v_{rel}\sqrt{\left|\frac{\partial u_F}{\partial y}\right|} \quad (3.4.12)$$

where  $\left|\frac{\partial u_F}{\partial y}\right|$  is the perpendicular gradient of the fluid flow to the middle incident-flow velocity. The validity of this relationship is limited to the special case of an unlimited linear shear flow. In addition it is only valid for a small range of values of the particle Reynolds numbers:

$$\text{Re}_\omega \ll 1 \quad \text{and} \quad \text{Re}_P \ll \sqrt{\text{Re}_S} \quad (3.4.13)$$

where  $\text{Re}_\omega$  is the rotational Reynolds number:

$$\text{Re}_\omega = \frac{1}{4} \frac{d_P^2 \omega_{rel}}{\nu_F} \quad (3.4.14)$$

and  $\text{Re}_S$  is the Reynolds number of the shear flow:

$$\text{Re}_S = \frac{d_P^2 \left|\frac{\partial u_F}{\partial y}\right|}{\nu_F} \quad (3.4.15)$$

For larger particle Reynolds numbers corrections of the Saffman relationship were suggested [71, 72]. The determination of the Saffman force in complex three-dimensional flows is carried out with the following more general equation,

$$\vec{F}_S = \frac{1}{4} \rho_F d_P^2 \sqrt{\nu_F} \frac{1}{\sqrt{|\vec{\omega}_F|}} c_S (\vec{v}_{rel} \times \vec{\omega}_F) \quad (3.4.16)$$

whereby  $c_S$  is the Saffman force factor. This factor is a function of  $\text{Re}_P$  and  $\text{Re}_S$ , which is presented in detail by Frank [58].

On a particle of the mass  $m_P$  the acting gravitation/lift force  $\vec{F}_G$  is computed as:

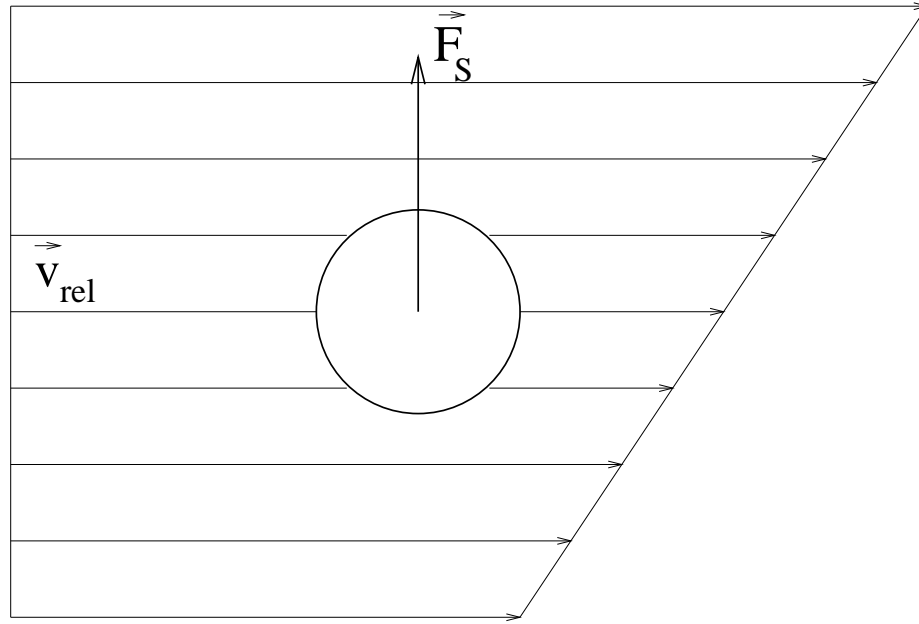


Figure 3.2: Transverse force on a particle in a shear flow.

$$\vec{F}_G = m_P \vec{g} = \frac{\pi}{6} \rho_P d_P^3 \vec{g} \quad (3.4.17)$$

where  $\vec{g}$  is the acceleration due to gravity. Comparing eq. (3.4.2) with eq.(3.4.17), it can be noted that they are depending on the square and/or cubic of the particle diameter. That means that the gravitational force has particularly an influence on the movement of relatively large particles, while the influence of the gravitational force on the motion of relatively small particles is negligible.

The virtual mass force accounts for the effect of acceleration of the continuous flow displaced by the particles, and can be modeled as [73]:

$$\vec{F}_{VM} = \frac{1}{2} c_{VM} \rho_F \frac{\pi d_P^3}{6} \left( \frac{D \vec{v}_P}{Dt} - \frac{D \vec{v}_F}{Dt} \right) \quad (3.4.18)$$

Numerous discussions were concerned whether the virtual mass force exists and

what is the value of the constant  $c_{VM}$  [74, 75]. 3D-simulation results have shown that the concept of virtual mass is meaningful and  $c_{VM}$  can be taken as  $c_{VM} = 1$  [76, 77, 78].

The local pressure gradient of the flow around the fluid developing from its movement, induces a force effect on the particle and is calculated as follows:

$$\vec{F}_P = \frac{-m_F}{\rho_F} \nabla p = -\frac{\pi d_P^3}{6} \nabla p \quad (3.4.19)$$

The Basset force  $\vec{F}_B$  is the force associated with the past movements of the particle. The Basset force is the subject of extensive research, see Huilier et al. [77, 78], Magnaudet [76], Liang et al.[79] and Kim et al. [80]. It can be calculated as follows:

$$\vec{F}_B = \frac{18\rho_F\nu_F}{d_P^2\rho_P} \int_0^t K(t-\tau) \frac{d(\vec{v}_F - \vec{v}_P)}{d\tau} d\tau \quad (3.4.20)$$

with

$$K(t-\tau) = \left\{ \left[ \frac{4\pi(t-\tau)v_F}{d_P^2} \right]^{1/4} + \sqrt{\pi(t-\tau)^2 \frac{|\vec{v}_F - \vec{v}_P|^3}{d_P\nu_F f_H^3}} \right\}^{-2} \quad (3.4.21)$$

where

$$f_H = 0.75 + 0.105\text{Re}_{P,\tau} \quad (3.4.22)$$

Particles are assumed to be non-deformable and spherical. The ratio of particle density and the fluid density is  $\rho_P/\rho_F = 10^3$  approximately. Virtual mass force and pressure gradient force are of the order of  $\rho_F/\rho_P$ , and Basset force is of the order of  $(\rho_F/\rho_P)^{1/2}$ , as discussed by Chung and Troutt [81]; hence these forces are neglected in the present work.

Thus all forces of the translational particle movement relevant for the gas solid flow have been described. The expressions indicated above for the different forces are substituted in Equation 3.4.1, and add the second term of the virtual mass force and divide by the particle mass of  $m_P + 0.5m_F$ , thus we will get an ordinary differential equation for displacement and speed of the particle:

$$\frac{d}{dt} \begin{bmatrix} x_P \\ y_P \\ z_P \end{bmatrix} = \begin{bmatrix} u_P \\ v_P \\ w_P \end{bmatrix} \quad (3.4.23)$$

$$\begin{aligned} \frac{d}{dt} \begin{bmatrix} u_P \\ v_P \\ w_P \end{bmatrix} &= \frac{3}{4} \frac{\rho_F}{(\rho_P + \frac{1}{2}C_{VM}\rho_F)} v_{rel} c_W (Re_P) \begin{bmatrix} u_F - u_P \\ v_F - v_P \\ w_F - w_P \end{bmatrix} \\ &+ \frac{v_{rel}}{\omega_{rel}} c_M(\sigma_M) \begin{bmatrix} (v_F - v_P) (\omega_{z,P} - \frac{1}{2}\omega_{z,F}) - (w_F - w_P) (\omega_{y,P} - \frac{1}{2}\omega_{y,F}) \\ (w_F - w_P) (\omega_{x,P} - \frac{1}{2}\omega_{x,F}) - (u_F - u_P) (\omega_{z,P} - \frac{1}{2}\omega_{z,F}) \\ (u_F - u_P) (\omega_{y,P} - \frac{1}{2}\omega_{y,F}) - (v_F - v_P) (\omega_{x,P} - \frac{1}{2}\omega_{x,F}) \end{bmatrix} \\ &+ \frac{2\sqrt{\nu_F}}{\pi\sqrt{|\vec{\omega}_F|}} c_S(Re_P, Re_S) \begin{bmatrix} (v_F - v_P) \omega_{z,F} - (w_F - w_P) \omega_{y,F} \\ (v_F - w_P) \omega_{x,F} - (u_F - u_P) \omega_{z,F} \\ (u_F - u_P) \omega_{y,F} - (v_F - v_P) \omega_{x,F} \end{bmatrix} \\ &- \frac{1+c_{VM}/2}{\rho_P+c_{VM}\rho_F/2} \begin{bmatrix} \partial p/\partial x \\ \partial p/\partial y \\ \partial p/\partial z \end{bmatrix} + \frac{\rho_P-\rho_F}{\rho_P+c_{VM}\rho_F/2} \begin{bmatrix} g_x \\ g_y \\ g_z \end{bmatrix} \end{aligned} \quad (3.4.24)$$

with

$$\begin{aligned} Re_P &= \frac{d_P v_{rel}}{\nu_F}, \quad Re_\omega = \frac{1}{4} \frac{d_P^2 \omega_{rel}}{\nu_F}, \quad \sigma_M = \frac{1}{2} \frac{d_P \omega_{rel}}{v_{rel}}, \quad \vec{\omega}_F = \text{rot } \vec{v}_F \\ v_{rel} &= \sqrt{(u_F - u_P)^2 + (v_F - v_P)^2 + (w_F - w_P)^2}, \quad Re_S = \frac{d_P^2}{\nu_F} |\text{rot } \vec{v}_F| \end{aligned}$$

$$\omega_{rel} = \sqrt{(0.5\omega_{Fx} - \omega_{Px})^2 + (0.5\omega_{Fy} - \omega_{Py})^2 + (0.5\omega_{Fz} - \omega_{Pz})^2} \quad (3.4.25)$$

If the initial conditions of the particles position and its speed are well known at  $t_0$ , then the particle speed at  $t_1 = t_0 + \Delta t$  is a result of the numerical solution of eq. (3.4.24). The numerical computations are carried out by using a Runge-Kutta method of fourth order. Moreover eq. (3.4.23) is numerically integrated in the same way as eq. (3.4.24). Particle wall and particle-particle collisions have an additional influence both on the translation and rotation particle movement and are described in the next sections.

### 3.4.1 Equations for the particle rotation

The particles are affected with moments due to the collision with the wall or other particles. Therefore, a conservation equation for the particle rotation is necessary. The particle rotation has not an influence on the translation movement of the particles. Thus, Magnus force can be neglected for high rotation velocity. The angular momentum equation is a balance equation for all acting moments:

$$I_P \frac{d\vec{\omega}_P}{dt} = \sum_i \vec{T}_i \quad (3.4.26)$$

Here  $I_P$  is the polar mass-moment of inertia of the spherical particle,

$$I_P = \frac{1}{10} m_P d_P^2 = \frac{\pi}{60} \rho_P d_P^5 \quad (3.4.27)$$

and  $\sum_i \vec{T}_i$  is the sum of the moments acting on the particle. These moments can be e.g. aerodynamic nature, i.e. result from viscous friction between the particle surface and the surrounding fluid. Following investigations of Dennis et al. [82] one can write:

$$\vec{T} = \frac{\rho_F}{2} \left( \frac{d_P}{2} \right)^5 c_\omega \omega_{rel} \vec{\omega}_{rel} \quad (3.4.28)$$

The rotation factor  $c_\omega$  used in the above equation is dependent on the Reynolds number of rotation  $Re_\omega$  .

After using the eq. (3.4.27) and (3.4.28) in eq. (3.4.26) and division by  $I_P$  the differential equation for the rotation speed of the particle results:

$$\frac{d}{dt} \vec{\omega}_P = \frac{15}{16\pi} \frac{\rho_F}{\rho_P} c_\omega \omega_{rel} \vec{\omega}_{rel} \quad (3.4.29)$$

This equation is numerically solved as already done for the translation movement by using the Runge Kutta procedure. In contrast to the computation of the translation movement here no further integration takes place for the determination of the angle around which the particle turns during the time step  $\Delta t$  .

### 3.4.2 Influence of fluid turbulence on the particle movement

The fluid speed has been used in the equations indicated in the preceding subsections for the computation of the particle movement. Hence, also high frequency fluctuations of the fluid flow can be noticed by the particles. The flow speed is accessible using turbulence models. The Stokes number informs us about the inertia of a particle compared to fluctuation of the surrounding fluid. The particles react as a function of their density and diameter strongly differently to turbulent fluctuations of the continuous phase.

In this work the Lagrangian-Stochastic-Deterministic model (LSD) is used following Milojevic [83, 84]. It is a derived version from the Eddy interaction model (EIM),

developed by Graham [85]. In this model mean fluid speed  $u_F$  is replaced by the momentary speed of  $u_{F,mom}$  in the well-known way:

$$u_{F,mom} = u_F + u'_F \quad (3.4.30)$$

The fluctuation speed  $u'_F$  is determined with the help of a stochastic procedure. In addition it is accepted that  $u'_F$  is a random variable, which is subject to a Gaussian distribution (isotropic turbulence) with the average value of 0 m/s and the standard deviation of  $\sqrt{\frac{2}{3}k}$ , whereby  $k$  is the turbulent energy of the fluid. According to the determination of the fluctuation speed the momentary fluid speed of particles can be computed under the influence of turbulence. Production of a coincidental fluctuation speed is equivalent to the generation of a turbulence eddy. The length of the time interval  $\Delta t_W$  is limited here by two factors. These are on the one hand the eddy life duration  $T_E$  and on the other hand the transit time  $T_D$ , i.e. the time, which particles need, in order to cross the eddy. For the determination of the eddy life duration the following relationship is used,

$$T_E = c_T \frac{k}{\varepsilon} \quad (3.4.31)$$

$c_T$  is a semi empirical constant ranging between 0.116 - 0.46 [86]. The transit time  $T_D$  depends on the size of the eddy and the relative velocity between eddies and particles. The size of the eddy becomes:

$$L_E = T_E \sqrt{\frac{2}{3}k} \quad (3.4.32)$$

Thus the transit time is:



$$T_D = \frac{L_E}{v_{rel}} \quad (3.4.33)$$

If a turbulent eddy was generated, then the interaction time between the particle with this eddy can be accounted by:

$$\Delta t_W = \min(T_E, T_D) \quad (3.4.34)$$

### 3.4.3 Influence of particles on the fluid movement

In the preceding subsections the particle movement is described by the aerodynamic forces. If by the aerodynamic application of a force of the fluid flow the impulse of a particle changes by  $\Delta p_P$ , then the impulse of the fluid must likewise change in the environment of the particle, in the following way for reasons of the momentum conservation

$$\Delta p_F = -\Delta p_P \quad (3.4.35)$$

The fluid flow is affected also by the movement of the particles. A reciprocal effect takes place between the dispersed and fluid phase, which is based on mutual impulse transmission between the phases. For the consideration of phase coupling in the numerical computation of gas/particle flows the PSI-Cell-method (Particle-Source-in-Cell) was developed by Crowe [87]. Here the influence of the particles on the fluid flow is modeled by appropriate source terms, which are introduced in the balance equations of the continuous phase.

In Figure 3.3 the shift of a particle is shown schematically within a time step  $\Delta t$  from point 1 to 2. On the assumption that the change of the particle speed between

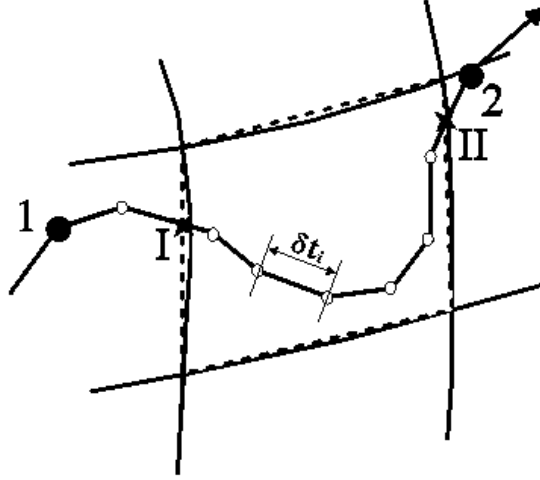


Figure 3.3: Sketch of a particle path in a control volume.

these points is linear, the impulse source terms, which in turn result from this particle path, are for the regarded control volume

$$Q_{Pu,i,j} = -\frac{1}{V_{i,j}} m_P \left( \frac{u_P^2 - u_P^1}{\Delta t^1} - g_x \right) \quad (3.4.36)$$

$$Q_{Pv,i,j} = -\frac{1}{V_{i,j}} m_P \left( \frac{v_P^2 - v_P^1}{\Delta t^1} - g_y \right) \quad (3.4.37)$$

Here  $V_{i,j}$  is the size of the control volume and  $\Delta t^1$  the needed time for the movement from 1 to 2. The source terms of the  $k-\epsilon$  equations, i.e. the consideration of the influence of the dispersed phase on the fluid turbulence, are not generally accepted. Therefore, the influence of the particles to the flow field is not used in this work.

### 3.5 Particle/wall collisions

In most of the important industrial applications disperse multiphase-flows are confined by walls or rigid boundaries. Especially the motion of large particles, which is dominated by inertia, is strongly influenced by this confinement. Considering the wall-collision process it has been shown that irregularities due to wall roughness and deviation of particle shape from sphere play an important role [88, 89, 90]. The particle-wall collisions were treated according to the irregular bouncing model by Sommerfeld [86, 91] in the modified wall roughness formulation given in [67, 88, 10]. The particle collides with an inclined virtual wall shown in Figure 3.5. The inclination angle  $\gamma$  is sampled from a Gaussian distribution with a mean value of  $0^\circ$  and a standard deviation of  $\Delta\gamma$ .  $\Delta\gamma$  depends on the particle diameter  $d_P$  and the roughness parameters shown in Figure 3.4 and may be estimated by:

$$\begin{aligned} \Delta\gamma &= \arctan \frac{2\Delta H_r}{L_r} \quad \text{for } d_P \geq \frac{L_r}{\sin\left(\arctan \frac{2H_r}{L_r}\right)} \\ \Delta\gamma &= \arctan \frac{2H_r}{L_r} \quad \text{for } d_P < \frac{L_r}{\sin\left(\arctan \frac{2H_r}{L_r}\right)} \end{aligned} \quad (3.5.1)$$

Where

- $L_r$  is the mean cycle of roughness.
- $H_r$  is the mean roughness depth.
- $\Delta H_r$  is the standard deviation of the roughness height.

Since no preferential direction of roughness is assumed, the inclined virtual wall is additionally turned around the normal vector of the original wall by an azimuthal

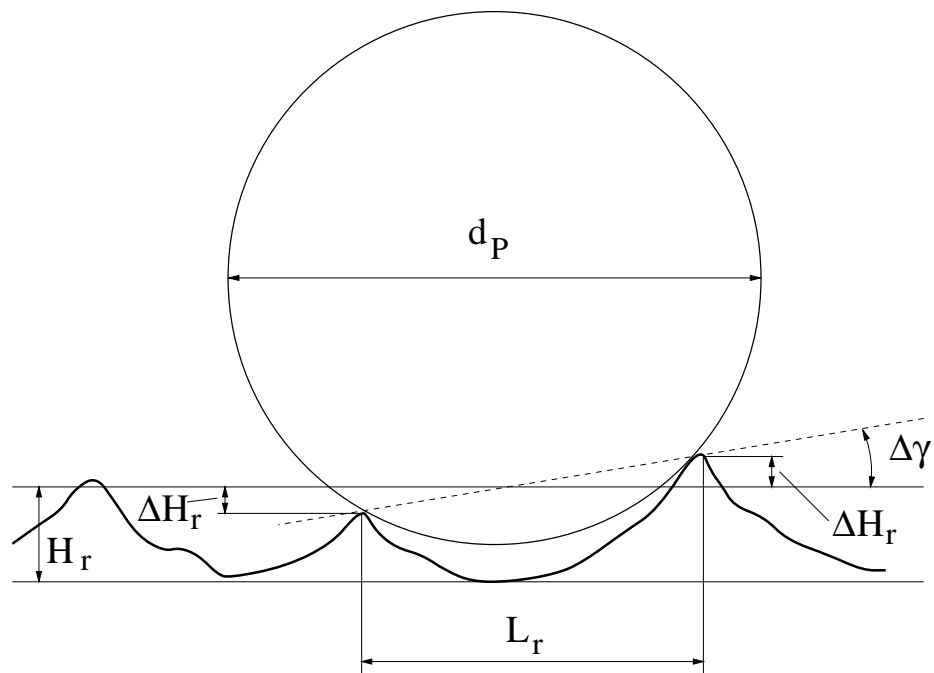


Figure 3.4: Wall roughness effect with the particle.

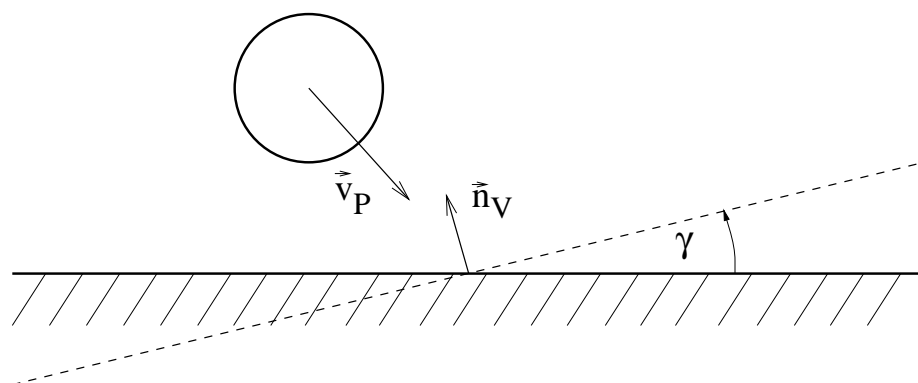


Figure 3.5: Particle-wall collision of a spherical particle with an inclined virtual wall.

angle  $\sigma_a$ . This angle is sampled from a uniform distribution in the range  $[-\pi, \pi]$ .

The particle velocity and angular velocities are transformed to a coordinate system that is aligned with the collision plane. For the following equations it is assumed that the  $y$  axis of the transformed coordinate system is identical to the normal vector of the collision plane. The computation of the velocities and angular velocities after rebound is carried out by applying the impulse equations and taking into account the sort of collision, i.e. sliding or non-sliding collision [67]:

- Sliding collision for:

$$-\frac{2}{7f_w(e_w + 1)} \leq \frac{v_P^{(1)}}{|v_r|} \leq 0$$

$$u_P^{(2)} = u_P^{(1)} + \varepsilon_x f_w (e_w + 1) v_P^{(1)}$$

$$v_P^{(2)} = -e_w v_P^{(1)}$$

$$w_P^{(2)} = w_P^{(1)} + \varepsilon_z f_w (e_w + 1) v_P^{(1)}$$

$$\omega_x^{(2)} = \omega_x^{(1)} - \frac{5}{d_P} \varepsilon_z f_w (e_w + 1) v_P^{(1)}$$

$$\omega_y^{(2)} = \omega_y^{(1)}$$

$$\omega_z^{(2)} = \omega_z^{(1)} + \frac{5}{d_P} \varepsilon_x f_w (e_w + 1) v_P^{(1)} \quad (3.5.2)$$

- Non-sliding collision for:

$$\frac{v_P^{(1)}}{|v_r|} < -\frac{2}{7f_w(e_w + 1)}$$

$$\begin{aligned} u_P^{(2)} &= \frac{5}{7} \left( u_P^{(1)} - \frac{d_P}{5} \omega_z^{(1)} \right) \\ v_P^{(2)} &= -e_w v_P^{(1)} \\ w_P^{(2)} &= \frac{5}{7} \left( w_P^{(1)} + \frac{d_P}{5} \omega_x^{(1)} \right) \\ \omega_x^{(2)} &= \frac{2}{d_P} w_P^{(1)} \\ \omega_y^{(2)} &= \omega_y^{(1)} \\ \omega_z^{(2)} &= -\frac{2}{d_P} u_P^{(1)} \end{aligned} \tag{3.5.3}$$

with

$$|v_r| = \sqrt{\left( u_P^{(1)} + \frac{d_P}{2} \omega_z^{(1)} \right)^2 + \left( w_P^{(1)} - \frac{d_P}{2} \omega_x^{(1)} \right)^2} \tag{3.5.4}$$

and

$$\varepsilon_x = \frac{u_P^{(1)} + \frac{d_P}{2} \omega_z^{(1)}}{|v_r|} \quad , \quad \varepsilon_z = \frac{w_P^{(1)} - \frac{d_P}{2} \omega_x^{(1)}}{|v_r|} \tag{3.5.5}$$

In these equations  $f_w$  is the coefficient for restitution and  $e_w$  is the coefficient of kinetic friction, which can be obtained from [88]. The superscripts <sup>(1)</sup> and <sup>(2)</sup> indicate values before and after collision, respectively.

## 3.6 Computation of the dispersed phase flow

In the previous sections the computation of the motion of an individual particle in a turbulent flow was described. Flow parameters of the particle phase are computed by integration of an individual particle motion in the turbulent flow. These parameters are local particle concentration and mass loading. For the determination of these parameters there are two different procedures, which are described in the following.

### 3.6.1 Trajectory computation

This procedure is based on the successive computation of a large number of particle trajectories. It is accepted that each particle at the same starting point and with the same initial conditions goes together. This procedure assumes first a well-known stationary fluid flow, which is a basis for particle tracking. One trajectory represents thus a group of particles, which possess all the same physical characteristics. This group is a part of the particle mass flow in a stationary gas particle flow. The number of particles per unit time  $\dot{N}_P$ , which moves along a trajectory, results from the total particle mass flow  $\dot{m}_P$  and the total number of the trajectories  $N_T$ .

$$\dot{N}_P = \frac{\dot{m}_P}{\rho_P \sum_{J=1}^{N_T} \frac{\pi}{6} d_{PJ}^3} \quad (3.6.1)$$

The macroscopic flow parameters of the particle phase result for each control volume from the sum of this control volume crossing the trajectories. In order to get statistically representative values the number of computed trajectories must be sufficiently large.

### 3.6.2 Simultaneous particle tracking

In this procedure the motions of all simulated particles, which are at a certain time within the flow area, are computed simultaneously. However, the balance equations of the continuous and dispersed phase are integrated for a given time step  $\Delta t$ . If a particle collides during this time step with the flow boundary, then the computation of the step takes place in two indexing steps. First the particle motion is computed up to reaching the wall. With the help of the collision-wall model described above the particle speed and rotation speed are determined according to the impact. With the result of the computation of all individual particles of the current time step, the next time step is carried out in the same way. The procedure of simultaneous particle tracking is an intermittent computational method. The macroscopic flow parameters of the particle phase result for a control volume at each time from an averaging procedure over all particles, which are present at this time in the control volume. The procedure is suitable both for the simulation of intermittent and stationary gas particle flows.

## 3.7 Solution algorithm

The solution algorithm for the equation of particle motion is based on the program package PartFlow-3D developed by Frank [58]. Fundamental features of the program are:

1. Solution of the particles equations of motion for the particle coordinates, translational and rotational velocities by a 4th order Runge-Kutta solving scheme.
2. Particle tracking on complex, 3-dimensional, block-structured numerical grids.



3. Taking into account all relevant forces of gas-particle systems with  $\rho_F/\rho_P \ll 1$
4. Taking into account the effect of fluid turbulence on the motion of the disperse phase by a Lagrangian Stochastic-Deterministic (LSD) turbulence model.
5. Particle-wall collision model including a wall roughness model depending on particle diameter.
6. Full parallelization using either static or dynamic domain decomposition for optimum work load balancing and maximum parallel efficiency.

# Chapter 4

## Validation process and computational results of cyclone flows

### 4.1 Validation Process

Validation examines whether the physical models used in computer simulations agree with real world observations. It is a process that addresses the question 'Have we accurately formulated and solved the equations?'. Validation is one of the two fundamental columns upon which the credibility of numerical simulations is built. The basic validation strategy is to identify and quantify both error and uncertainty through comparison of simulation results with experimental data. The validation process will be mainly concerned with the investigation of secondary flow phenomena of the *square channel flow*.

#### 4.1.1 Channel flow

Turbulent flows inside square channels represent important engineering issues, which are characterized by the existence of secondary flows. These flow fields are driven by

the turbulent motion of the main flow. The secondary flow also termed Prandtl's secondary motion is directed perpendicular to the bulk flow and represents a resistance regarding the momentum transport. The understanding of the relation between the secondary flow and the ejection mechanisms from the walls still requires complete resolution and thus more detailed investigations. Numerous studies exist regarding the mean streamwise vorticity equation. A more refined model is introduced by Demuren and Rodi [92] to investigate the origin of the secondary motion. The model is verified by the application to a developing flow in a square duct and also to a developing flow in a partially roughened rectangular duct. The mechanisms, which initiate secondary flows in developing turbulent flows along a corner section are examined by Gessner [93] on the basis of both, energy and vorticity considerations. The results show that a transverse flow is initiated and directed towards the corner as a direct result of turbulent shear stress gradients normal to the bisector. The results indicate further, that anisotropy of the turbulent normal stresses does not play a major role in the generation of secondary flows. Mechanisms responsible for the generation of the stress-driven secondary flows are studied by Huser and Biringen [94] based on DNS results by analyzing the instantaneous turbulence structures. It is demonstrated that the mean secondary flow pattern and the anisotropic Reynolds stress distribution can be explained by the preferred location of the ejection structure near the corner. Another reason for this behaviour can be found in the interaction between bursts from the two intersecting walls. A heated duct with a higher temperature prescribed at one wall is considered by Vazquez and Métais [95]. The authors observed, that an amplification of near-wall secondary flows results in a decrease of the turbulent fluctuations in the near-wall region. Conversely, these enhancements can occur in the

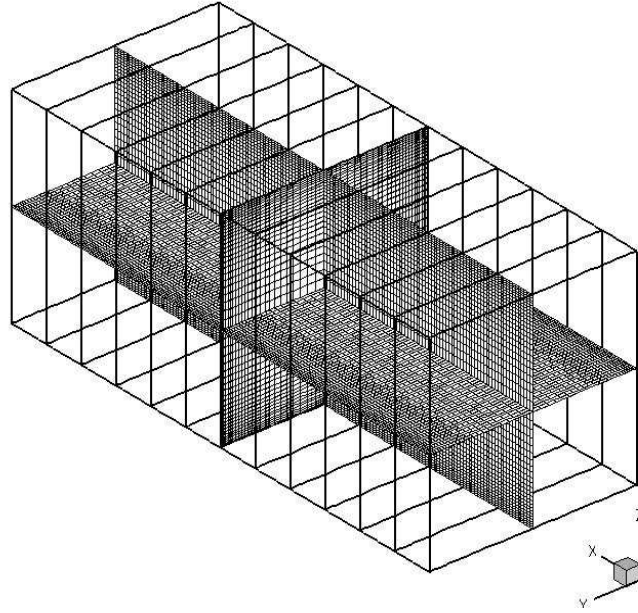


Figure 4.1: Schematic of the channel geometry and numerical grid.

outer wall region.

#### 4.1.2 Flow and geometry descriptions

The objective of the present study is to investigate this physical phenomenon at low and high Reynolds numbers using Large Eddy Simulation (LES). Our results will be compared with previous DNS data gained by Gavrilakis [96] at a low Reynolds number of  $Re = 5000$ . Moreover, a comparison will be carried out with experimental results at a higher Reynolds number of  $Re = 35,000$  of Sato et al. [97]. We also studied the flow at  $Re = 100,000$  numerically using LES. The computations of the fully developed airflow were performed for a straight square channel with a cross section of  $0.25 \times 0.25 \text{ m}^2$  and a length of  $0.6 \text{ m}$ . Figure 4.1 shows the implemented numerical grid and the corresponding co-ordinate system. The performed investigations focus primarily on the mean secondary flow velocity within the channel.

### 4.1.3 Computational parameters

The conservation equations of fluid motion are solved by using the LES with the MISTRAL-3D code, Denev et al. [52]. The code is based on a finite volume approach, implicit time steps, the SIMPLE algorithm for velocity-pressure coupling and a second-order central-differencing scheme (CDS) for convection, Patankar [98]. The solution procedure is based on a geometrical multigrid for improved convergence of pressure-velocity coupling on large numerical grids.

Computational results presented here have been performed on sub clusters of 12 processors of the Chemnitz Linux Cluster CLIC (528 Intel / Pentium III, 800 MHz, 512 Mb RAM per node, 2 x FastEthernet). The calculations on the PC clusters were performed using a Message Passing Interface (MPI) distribution of LAM-MPI 5.3.5. The CPU-time for the investigation (93000 time steps) was 142 hours and the achieved parallel efficiency (the ratio of speed up to the number of processors) amounts to 0.74. On average, 3 iterations of the SIMPLE algorithm within one time step were performed.

Initially, 3000 consequently decreasing time steps were performed in order to allow the duct flow to reach a fully-developed state. The time step reached after the initial iterations was 0.01 s real (physical) time [99]. This time step was kept constant during the rest of the computations. The averaging process was started after the initial iterations and all mean characteristics of the flow have been obtained after averaging over 90000 time steps. The averaging in the present study was done only with respect to time. The CFL number which defines the relation between the temporal and spatial discretization accuracy was 0.90. Furthermore, a second order accurate implicit time scheme was used in the study.

#### 4.1.4 Periodic boundary condition

Many flows have one or more directions of homogeneity (channel and duct flows), that allow the application of periodic boundary conditions. Periodic boundary conditions imply that the computational domain repeats itself an infinite number of times. Periodic boundary conditions are convenient, since they eliminate the need to specify inflow and outflow conditions and are easy to implement and efficient. Periodic boundary conditions are used here so that we copy the values of the three velocity components and the turbulent viscosity from the outflow (plane) toward the inlet boundary of the computational domain [52].

#### 4.1.5 Wall boundary conditions

At solid walls, the momentum flux must be known. Since the wall velocity is assigned, the no-slip condition allows the determination of the convective part  $u_i u_j$  of the momentum flux at the wall. Differentiation of the velocity profile to determine the viscous stress, however, is accurate only if the wall-layer is well resolved. To represent accurately the structure in the near-wall region, the first grid point must be located at  $y^+ > 1$ , and the grid spacing must be of order  $\Delta_x^+ \cong 50 - 150$ ,  $\Delta_z^+ \cong 15 - 40$  [100]. As  $Re \rightarrow \infty$ , an increasing of the number of grid points must be used to resolve a layer of decreasing thickness. This may also result in high aspect ratio of cells. Hence, this tends to degradate the numerical accuracy.

Alternatively, approximate boundary conditions, or wall models, may be used in LES. When the grid is not fine enough to resolve the near wall gradients, the wall layer must be modeled by specifying a correlation between the velocity in the outer flow and the stress at the wall. This approach allows the first grid point to be located

at  $y^+ \approx 30 - 150$ . Since the energy-producing vortical structures in the wall-layer do not have to be resolved, it permits the use of coarser meshes in the other directions as well:  $\Delta_x^+ \cong 100 - 600$ ,  $\Delta_z^+ \cong 100 - 300$  [100]. The classical wall-function approach of Launder and Spalding [42] is based on the  $k - \epsilon$  model and is therefore not suitable for LES computations. Alternatively, the wall functions of Werner and Wengle [101] have been used. They assume that the instantaneous velocity component, which is parallel to the wall, coincides in phase/time with the instantaneous wall shear stress. Thus there is no need for time averaging. The correlation is obtained without iterations from:

$$\begin{aligned}
 u^+ &= y^+ && \text{valid for : } 0 \leq y^+ \leq 11.81 \\
 u^+ &= a (y^+)^b && \text{valid for : } 11.81 < y^+ < 1000 \\
 u^+ &= u_{par}/u_t = u_{par}/\sqrt{\tau_w/\rho} && (4.1.1)
 \end{aligned}$$

The parameters used are:  $a = 8.3$  and  $b = 1/7$  [52]. In the above equations  $u_{par}$  is the instantaneous velocity component parallel to the wall.

#### 4.1.6 Results and discussions

A fully developed airflow in a straight square channel with a cross section of  $0.25 \times 0.25 \text{ m}^2$  and a length of  $0.6 \text{ m}$  has been investigated. The computational grid was designed using the grid generator ICEM/CFD-HEXA, see ICEM [102], and the number of computational cells chosen after testing grid independency is 331,776; 518,400 and 1,440,000 finite volume elements for Reynolds numbers of  $\text{Re} = 5000$ ,  $\text{Re} = 35,000$  and  $\text{Re} = 100,000$ , respectively. The numerical domain has been divided

into 12 blocks as shown in Figure 4.1. Inherently, the LES requires only the small-scale turbulent structures to be modeled. The eddy-viscosity model of Smagorinsky has been implemented to simulate small eddies. One result of our investigations concerns the induction of the secondary flows. The dominant turbulent mechanism is an ejection effect from the wall. The frequency and intensity of these ejections vary with the distance from the channel corners towards the wall centers. Close to the corner, the weak shear prevents the ejections. However, in the vicinity of the center of each wall, the strong shear stresses lead to an enhancement of the ejection mechanisms. This process generates a secondary flow directed from the core of the channel towards the corners, Figure 4.2 .

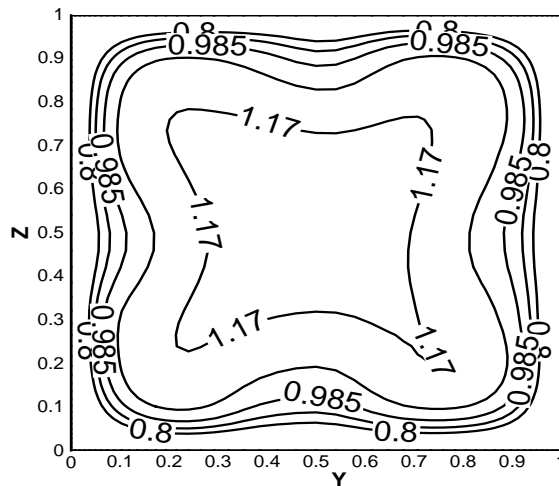


Figure 4.2: Isocontours of the mean streamwise velocity in a cross-section of the channel at a low Reynolds number of 5000 [51].

It becomes obvious from Figure 4.3 and 4.4 that the maximum secondary velocity occurs at a certain distance from the wall and not at the corner bisector. Moreover, the mean cross-stream flow does not remain close to the walls, but can be found at



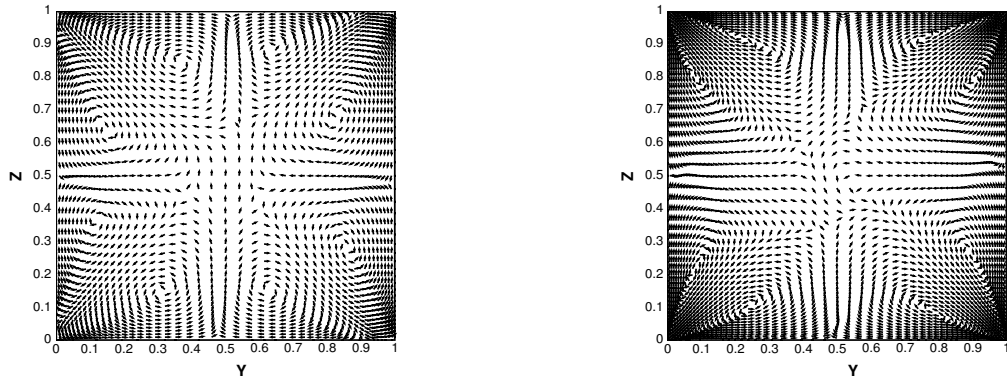


Figure 4.3: Secondary flow of the time-averaged flow field of the channel at  $Re = 5000$  (left) and  $Re = 35,000$  (right), at  $x = 0.3$  m [51] .

the wall bisectors.

Figure 4.3 (left) shows the secondary flow of the time-averaged flow in a cross section of the channel at  $Re = 5000$ . The maximum secondary velocity obtained in this work is 1.5 % of the mean bulk velocity. This agrees well with results gained by Denev et al.[52]. A Direct Numerical Simulation (DNS) of Gavrilakis [96] delivers a value of the maximum secondary velocity with respect to the bulk mean velocity of 1.9 % at a Reynolds number of  $Re = 5000$ . In our calculations the magnitude of the maximum secondary velocity at Reynolds numbers of  $Re = 35,000$  is 2.33 % of the bulk velocity, see Figure 4.3 (right). At a Reynolds number of  $Re = 100,000$  the magnitude of the maximum secondary velocity amounts to 2,67 % (see Figure 4.4). The maximum secondary velocity values related to the normal velocity are gathered in Figure 4.5. The indicated curve presents a qualitative course of the secondary flow as function of the Reynolds number.

The purpose of the validation of the three-dimensional square channel flows with

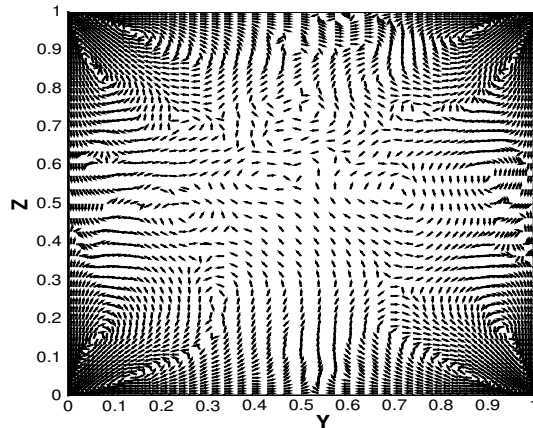


Figure 4.4: Secondary flow of the time-averaged flow field of the channel at  $Re = 100,000$ , at  $x = 0.3$  m [51].

different Reynolds numbers was to evaluate the accuracy and suitability of LES implemented in our code MISTRAL-3D. For that purpose secondary flow phenomena have been studied and the results revealed a qualitative agreement compared with the literature data. The comparison with DNS shown in Figure 4.5 is very good for the case under consideration. As a conclusion remark one can say that LES are able to capture the essential physics of secondary flow phenomena in square channel flows. After having validated and verified our modified code using LES, it will now be used in particular to simulate particle cyclone separation flows with highly swirling and anisotropic turbulence.

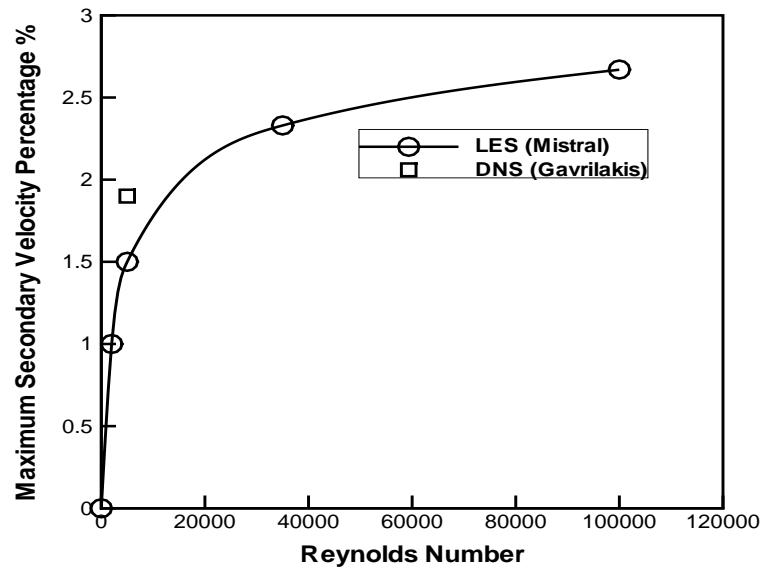


Figure 4.5: Maximum secondary velocity in percentage of the normal velocity versus  $Re$ .

## 4.2 Cyclone Flows

Our developed MISTRAL/PartFlow code and CFX version 4.4 have been used to predict the gas flow profiles. These calculations of the flow will be the basis for modeling the behavior of the solid particles in the cyclone. Particle trajectories, pressure drop and the cyclone separation efficiency have been studied in some detail.

This study was restricted to the most common reverse flow type of cyclone where the flow enters the cyclone through a tangential inlet and leaves it via an axial outlet at the top of the cyclone. The design of different cyclones was based on the Stairmand type cyclone [1]. The main characteristics of the flow was an annular outer flow which was swirling down the cyclone and an inner core which was moving upwards towards the outlet tube. The numerical calculations were compared with experimental results from different sources. The calculations for two different cyclone geometries with corresponding experimental results of Fraser et al. [103] and Boysan et al. [104] are presented. The difference in geometry between these two cyclones is basically characterized by the geometrical *swirl number*  $S_g$  [105]

$$S_g = \frac{\pi D_e D}{4 \cdot a \cdot b} \quad (4.2.1)$$

where

- $D_e$  is the outlet pipe diameter
- $D$  is the cyclone diameter
- $a$  is the cyclone inlet duct width
- $b$  is the cyclone inlet duct height

Due to different swirl numbers, the flow pattern in the two cyclones is significantly different.

### 4.2.1 Computational parameters

Two different cyclone geometries have been studied. The dimensions of the two cyclones under investigation are given in Table 4.1. For cyclone A and B, the calculated velocity field was compared with measurements presented by Fraser et al. [103] and Boysan et al. [104].

Due to the complex geometry of the cyclone a first-guess numerical grid with 80 different grid blocks and about 660,000 finite volume elements had to be designed for first numerical calculations of the continuous phase flow. It will be referred to the first numerical grid as coarse grid. In a second numerical investigation the numerical grid was redesigned using the grid generator ICEM/CFD-HEXA [102] with 80 grid blocks, about 1,300,000 finite volume elements, which will be referred to as fine uniform grid, Figure 4.6.

The blocks were created by extracting a solid block volume from the top surface of the cyclone in the axial-downward direction. The conical section was created by extracting and scaling the block volume to the designed angle. In the center region a geometric shape block was used, instead of a cylindrical block to avoid very high density of control volumes to the center.

The design of the control volumes was important for several reasons. First of all the control volumes had to be small enough to be able to resolve the significant length scale of the flow. In general this means that a more complex flow with large gradients needs more cells, i.e. a higher cell density in order to capture the correct flow field. More cells will on the other hand lead to a computationally larger problem

and require more CPU time. A compromise is to generate a denser mesh where large gradients are expected, by decreasing the mesh size, and to decrease the total number of cells in areas where the flow calculation is less sensitive to the cell size. The mesh size variation has been limited by a factor of 5 to ensure a smooth solution. Grid refinement was applied at the gas inlet and to the region in the vicinity of the lower end of the gas exit tube.

Table 4.1: Cyclone dimensions in mm

Cyclone Configuration	A	B
References	Fraser et al. [103]	Boysan et al. [104]
Cyclone diameter ( $D$ )	440	200
Outlet pipe diameter ( $De$ )	100	100
Cyclone outlet pipe length ( $S$ )	350	100
Height of the cylindrical section of cyclone ( $h$ )	360	300
Cyclone height ( $H$ )	1460	800
Cyclone inlet duct width ( $a$ )	200	100
Cyclone inlet duct height ( $b$ )	50	40
Cyclone lower outlet diameter ( $B$ )	110	72
Geometrical swirl number ( $S_g$ )	3.5	4

Boundary conditions were used at the inlet, which means that the values of the variables are specified. The Reynolds numbers are about 140,000 (Case A) and 50,000 (Case B) at the inlet duct based on the hydraulic diameter and the bulk velocity. At the inlet area, a laminar velocity profile was assumed. In reality, the inlet flow is not laminar. However, the results are insensitive to the inlet velocity profile [12]. This is likely due to the inlet region of the cyclone body where the inlet flow merges with the swirling gas within the flow field of the cyclone. In this region, the gas quickly forgets the conditions in the inflow duct. The variables that have been specified at the inlet were the normal velocity and the turbulence quantities  $k - \varepsilon$  for RSM turbulence

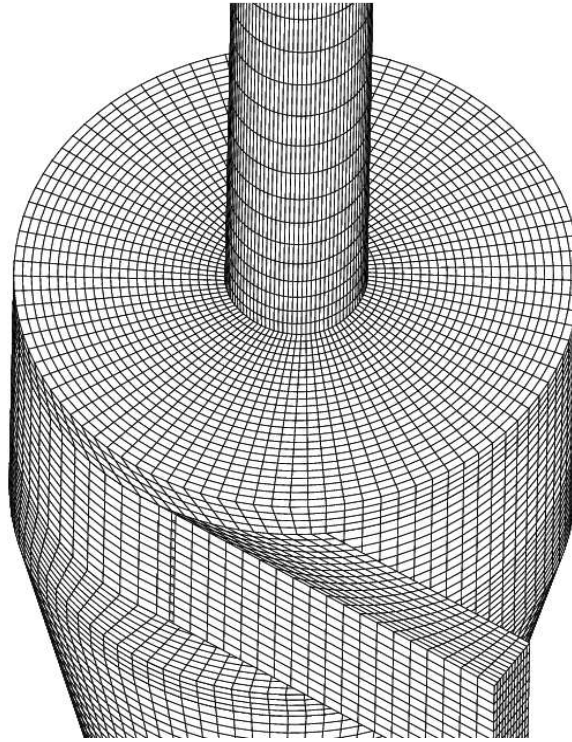


Figure 4.6: Schematic of the cyclone geometry and numerical grid.

models. The inlet turbulence energy is calculated using [57]

$$k_{inl} = (T_u \cdot u_{inl})^2 \quad (4.2.2)$$

and the turbulence dissipation is calculated using

$$\varepsilon = \frac{k_{inl}}{0.3D} \quad (4.2.3)$$

$u_{inl}$  is the mean inlet velocity,  $T_u$  the turbulence intensity defined as  $\frac{\sqrt{u'^2}}{\bar{u}}$  and  $D$  the hydraulic diameter at the inlet.  $D$  is calculated as  $D = 4A/P$  where  $A$  is the inlet area and  $P$  its perimeter. In case of the Reynolds stress model the Reynolds stresses must also be specified. By default, the normal stresses are set equal  $\frac{3}{2}k_{inl}$  and the other stresses are set equal to zero.

Computational results presented in this thesis have been performed on sub clusters of 40 processors of the Chemnitz Linux Cluster CLIC (528 Intel / Pentium III, 800 MHz, 512 Mb RAM per node, 2 x FastEthernet). The calculations on the PC clusters were performed using a Message Passing Interface (MPI) distribution of LAM-MPI 6.3.5. The CPU-time for the investigation (35 000 time steps) was 242 hours and the parallel efficiency (the ratio of speed up to the number of processors) achieved amounts to 0.74. On average, 5 iterations of the SIMPLE algorithm within one time step were performed.

Initially, 500 consequently decreasing time steps were performed in order to allow the cyclone flow to reach a fully-developed state. The time step reached after the initial iterations was 0.0001 s real (physical) time. This time-step was kept constant during the rest of the computations. The averaging process was started after the initial iterations and all mean characteristics of the flow have been obtained after averaging over 35 000 time steps. The averaging in the present study was done only with respect to time. The CFL number which defines the relation between the temporal and spatial discretization accuracy was 0.85,

$$CFL = \Delta t \max_{x,y,z} \left[ \frac{|u|}{\Delta x} + \frac{|v|}{\Delta y} + \frac{|w|}{\Delta z} \right] \quad (4.2.4)$$

Moreover, a second order accurate implicit time scheme was used in the study. The variables computed and later on shown for the two cyclones are presented in Table 4.2.



Table 4.2: Computed variables

Cyclone Configuration	A	B
References	Fraser et al. [103]	Boysan et al. [104]
Axial velocity	x	x
Tangential velocity	x	x
Axial velocity fluctuation		x
Tangential velocity fluctuation		x
Axial velocity at apex cone	x	
Tangential velocity at apex cone	x	
Pressure drop	x	
Particle trajectories	x	
Cyclone separation efficiency	x	

### 4.2.2 Continuous flow predictions (Cyclone A)

The investigated cyclone separator is characterized by the geometrical properties shown in Figure 4.7. Comparisons have been made between the calculated and measured axial and tangential velocity profiles at different horizontal cut planes in dimensionless form [106]. The dimensionless velocity profile is scaled with the inlet duct velocity. The spatial position is scaled by the cyclone radius  $D/2$ . The experimental data used for validation are published in Reference [103]. The error analysis in the experimental measurement is an important item to justify the accuracy of the experimental results and measurement uncertainty. The total errors are found in ranges of 0.90-13.35 percent for the tangential and axial velocities [103].

The predictions have also been checked at the apex cone of a cyclone separator. To our knowledge, there is no experimental data material available yet regarding the velocity fields at the apex cone area in the cyclone [106]. Thus, the presented comparison is limited to the differences observed between three different turbulence models, i.e.  $k - \epsilon$ , RSM and LES at this position. The location of interest here is

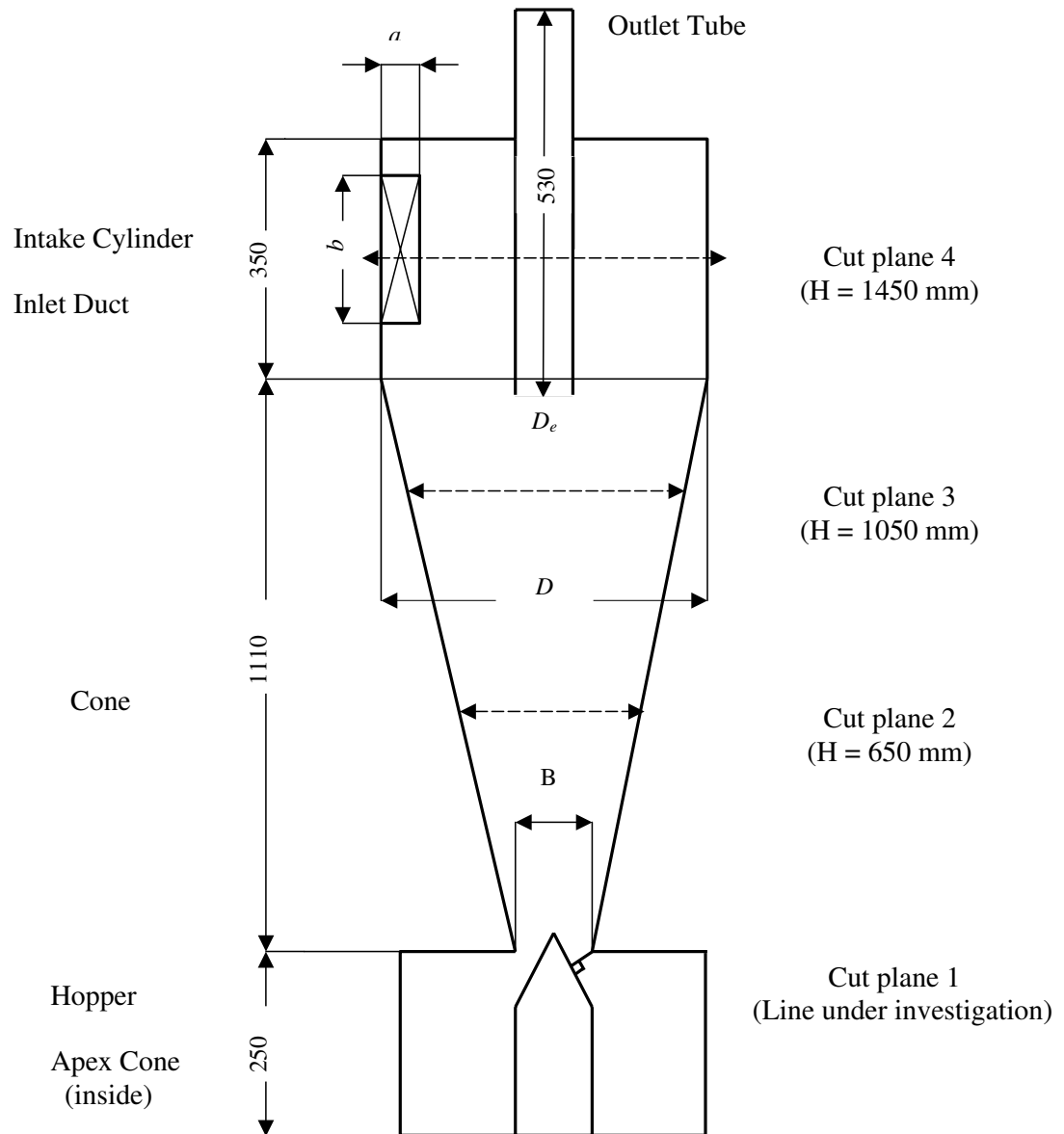


Figure 4.7: Location of different cut planes of cyclone A.

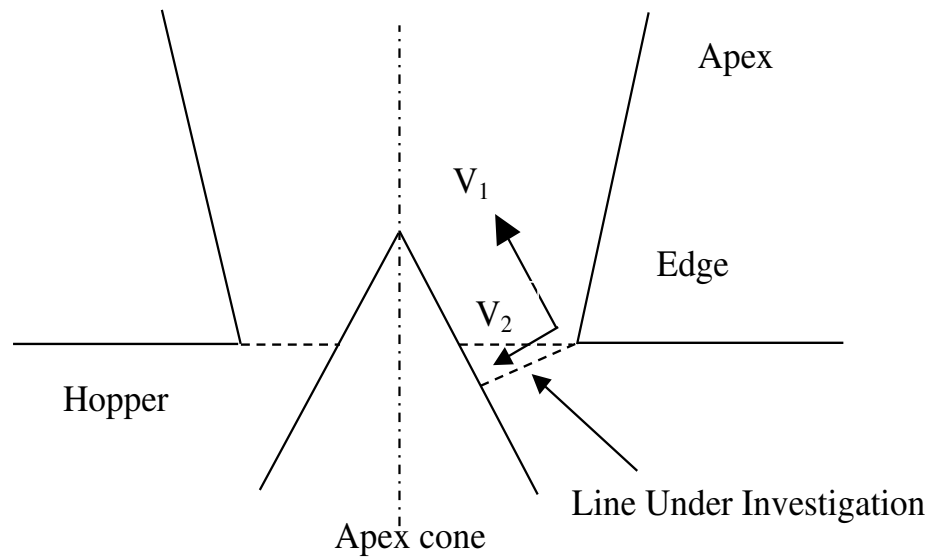


Figure 4.8: Apex cone frontal view, line under investigation normal to the apex cone surface towards the edge.

the separation area between the cyclone apex and the hopper. Hence, the velocity profile on a line between the surface of the apex cone and the edge (cut plane 1) of the hopper and perpendicular to the cone as shown in Figure 4.8 has been investigated. The line is normal to the cone surface. The length of the line under investigation is 30 mm in our case. Two of the three velocity components were predicted, ( $V_1$ ) is directed to the tip of the apex cone (axial component) and ( $V_2$ ) has a tangential direction. The velocity profiles were predicted in steps of  $90^\circ$ , see Figure 4.9.

In Figure 4.10 the predicted and measured tangential velocity profiles of the continuous phase flow of cut plane 2 are shown. The measured profiles show that the central region in the cyclone rotates like a solid body where the tangential velocity is increasing with an increasing radius. The maximum tangential velocity of approximately 1.24 times the inlet velocity is reached at a radius 25% from the centre of the cyclone. Then, the tangential velocity starts to decrease and reaches zero velocity at the wall. Comparison with the experimental data shows, that LES predicts the

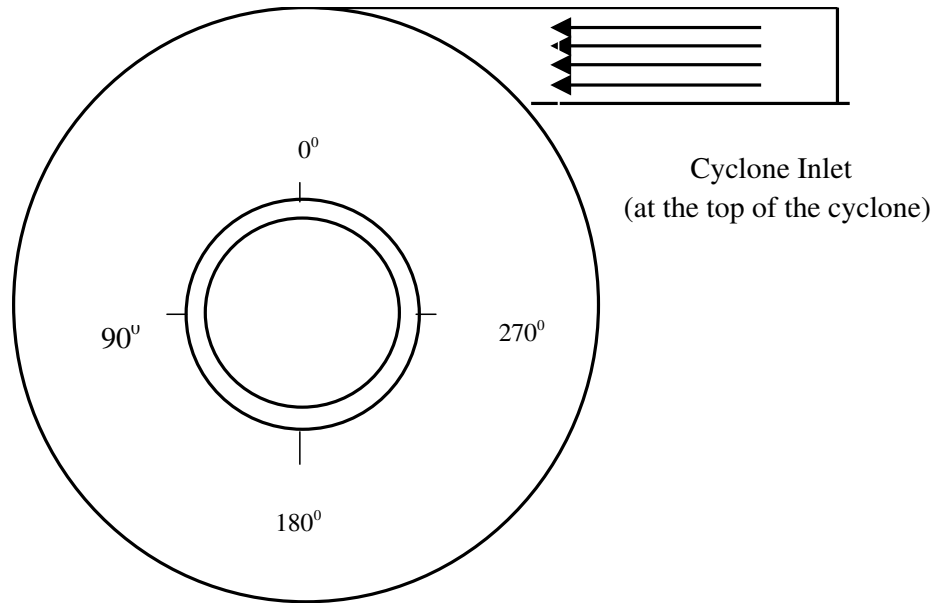


Figure 4.9: Apex cone top view.

shape of the tangential velocity profile with higher accuracy when compared to the predictions of the other models. The maximum tangential velocity in case of LES with fine grid is about 1.25 times the inlet velocity at about 25% of the cyclone radius. However, in case of RSM the maximum tangential velocity is about 0.95 times the inlet velocity but is shifted from the centre of the cyclone to about 45% of the cyclone radius. In case of  $k - \epsilon$ , it is shown that the maximum tangential velocity is about 1.2 times the inlet velocity and shifted very far toward the wall of the cyclone.

In Figure 4.11 the predicted and measured axial velocity profiles are shown at cut plane 2. Zero on the radial axis characterizes the centre of the cyclone. Positive velocities are directed upward towards the outlet. Both measurements and predictions show the typical axial velocity profiles of a cyclone. There is an outer region close to the wall of the cyclone where the flow is directed downwards. The maximum axial velocities are found in the centre of the cyclone where the flow is directed upwards

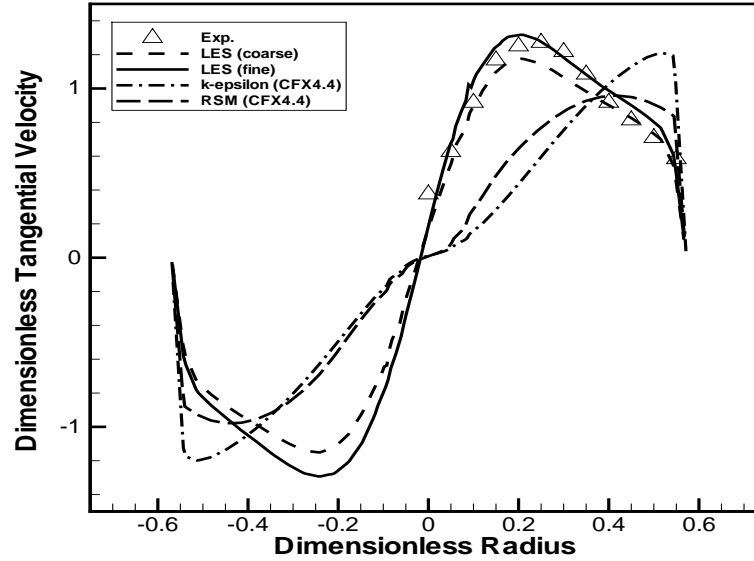


Figure 4.10: Comparison of three turbulence models and experimental data of reference [103], tangential velocities at cut plane 2.

with 1.1 times the inlet velocity. At about half or more of the cyclone radius, the flow reverses. The maximum axial velocities are found equal to the inlet velocity in case of LES with fine grid, 0.85 times the inlet velocity in case of RSM, and 0.9 times the inlet velocity in case of  $k - \epsilon$ . The flow reverses its direction at approximately 35% of the cyclone radius in case of LES, 40% in case of RSM, and 25% in case of  $k - \epsilon$ . It is also shown here that LES predicts the axial velocity profile more accurately than the RSM and  $k - \epsilon$  models, as shown in Figure 4.11 by comparison with the experimental data.

In Figure 4.12 the predicted and measured tangential velocity profiles are shown for the cyclone at cut plane 3. The same phenomenon of a rotating solid body is predicted especially in case of measurements and LES. It is shown that the LES

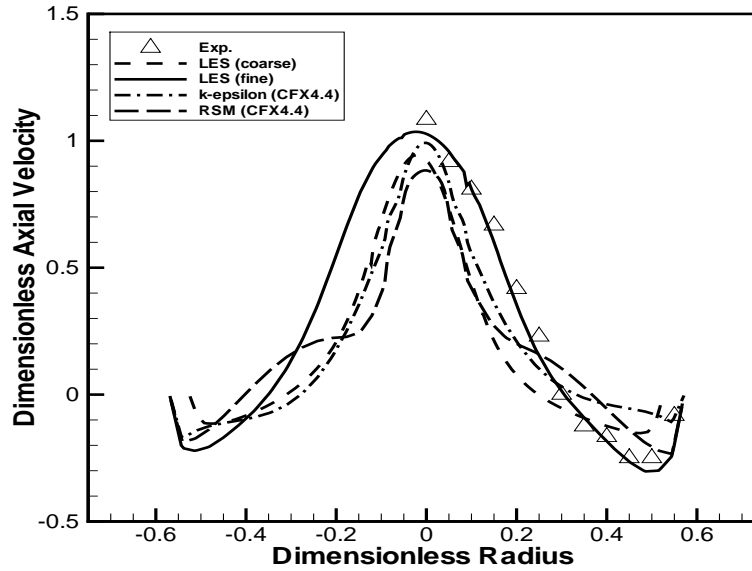


Figure 4.11: Comparison of three turbulence models and experimental data of reference [103], axial velocities at cut plane 2.

data obtained with a fine grid compare quite well with the measurement data. The maximum tangential velocity in case of LES is about 1.25 times the inlet velocity at about 25% of the cyclone radius. However, in case of RSM the maximum tangential velocity is about 1.1 times the inlet velocity and shifted from the centre of the cyclone also to about 60% of the cyclone radius. In case of the  $k-\epsilon$  model, it turns out that the maximum tangential velocity is about 1.4 times the inlet velocity and the maximum tends to be located very close to the wall.

In Figure 4.13 the predicted and measured axial velocity profiles of cut plane 3 are shown. Also here the positive velocities are directed upward towards the outlet. At this position, it can also be noted that LES with fine grid is most comparable to measurement data, with the maximum axial velocity equal to about 1.2 times the

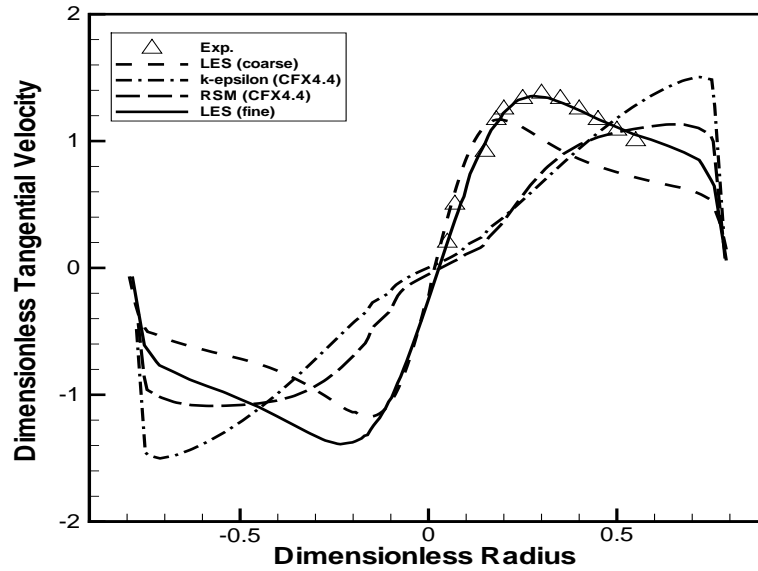


Figure 4.12: Comparison of three turbulence models and experimental data of reference [103], tangential velocities at cut plane 3.

inlet velocity. In case of RSM, the maximum axial velocity is still located at the centre of the cyclone with about 0.65 times the inlet velocity and will then reverse downward at approximately 45% of the cyclone radius. The maximum axial velocity is about 0.7 times the inlet velocity in case of the  $k - \epsilon$  model and the flow will also reverse its direction downward at 45% of the cyclone radius.

In Figure 4.14 the predicted tangential velocity profiles are presented for the cyclone at cut plane 4. It is shown that this plane has two regions; the outlet tube itself and the area outside the tube near the inlet duct. It is noted that the maximum tangential velocity is located outside the outlet tube with respect to the three turbulence models. The maximum tangential velocity is about 1.9 times the inlet velocity in case of LES, 1.95 times the inlet velocity in case of RSM, and 2 times the

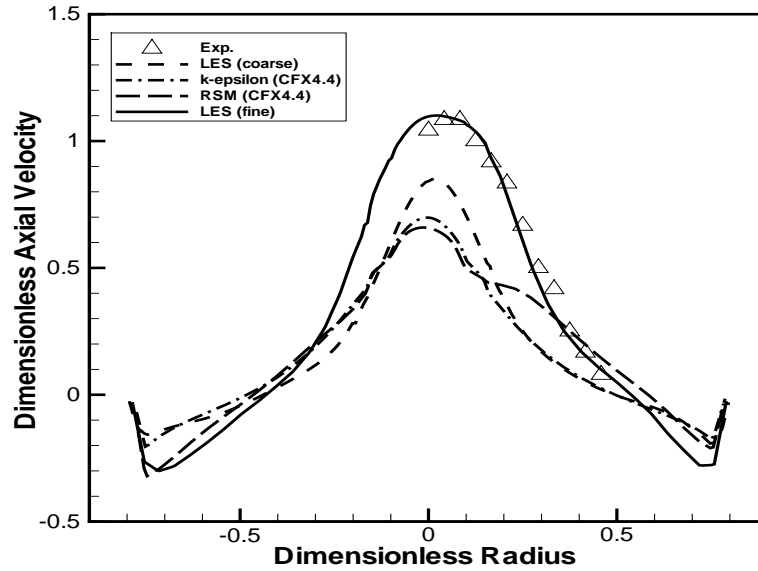


Figure 4.13: Comparison of three turbulence models and experimental data of reference [103], axial velocities at cut plane 3.

inlet velocity in case of the  $k - \epsilon$  model. The tangential velocity will tend to zero at the wall of the outlet tube. Inside the outlet tube, the same trend is shown for the maximum tangential velocity shifted from the centre of the tube in case of LES with a maximum velocity of 1.8 times the inlet velocity. The maximum velocity in case of RSM is about 1.2 times the inlet velocity and about 0.95 times the inlet velocity in case of the  $k - \epsilon$  model. For this (cut plane 4) and the following predictions, no experimental data are available yet.

In Figure 4.15 the predicted axial cyclone velocity profiles of cut plane 4 are shown. It turns out that the axial velocity outside the outlet tube is slightly below zero. Inside the outlet tube, the maximum axial velocity is about 4 times the inlet velocity in case of LES. However, the maximum velocity in case of RSM is only about



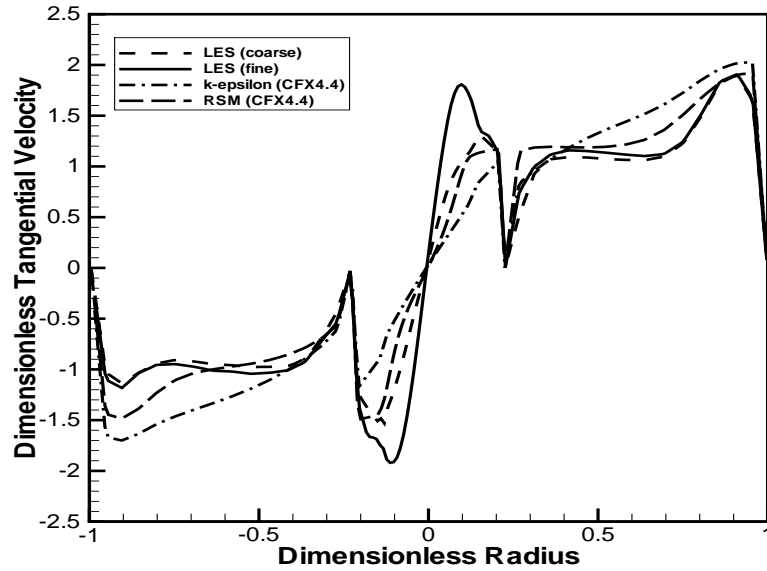


Figure 4.14: Comparison of three turbulence models and experimental data of reference [103], tangential velocities at cut plane 4.

2.8 times the inlet velocity and about 2.4 times the inlet velocity in case of the  $k - \epsilon$  model. It should be noted, that the three applied turbulence models are capable to resolve different degrees of flow complexity. The  $k - \epsilon$  model predicts as expected a solid body swirl shown in Figures 4.13 and 4.14. The flow within the outlet tube is a swirling pipe flow, which can be correctly described only by the LES approach. The reason is the strong anisotropic stress distribution due to the streamlines curvature.

In Figure 4.16, the predicted tangential velocity profiles at the  $0^\circ$  angle line are shown at the line between the apex cone and the edge of the hopper. The  $x$ -axis represents the scaled radius of the line under investigation. Zero is attached to the apex cone surface and 1 is attached to the edge of the hopper. Negative tangential velocities are directed downward toward the hopper in case of LES and RSM where

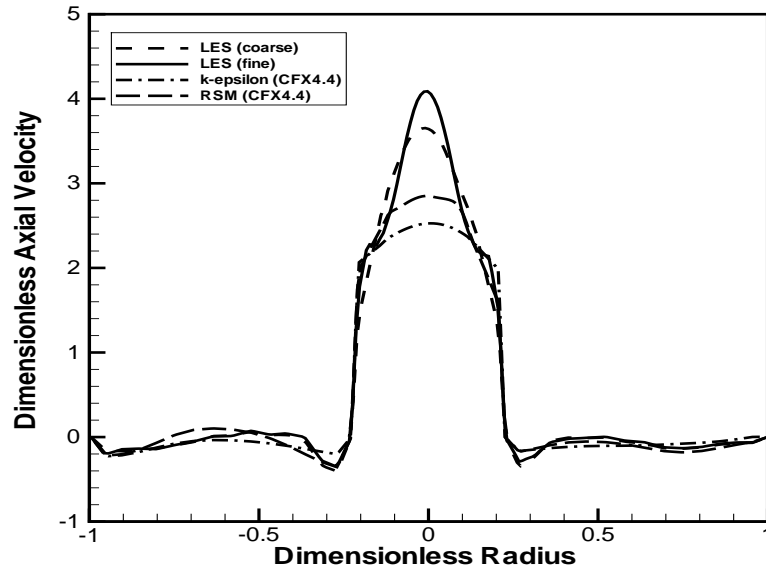


Figure 4.15: Comparison of three turbulence models and experimental data of reference [103], axial velocities at cut plane 4.

the minimum velocity is located at the centre of the line. The minimum tangential velocity is approximately about 0.78 times the inlet velocity in case of LES and 0.6 times the inlet velocity in case of the RSM model. The flow will tend to slow down close to the surface of the apex cone, which is the reason for incorporating the apex cone. It should be noted, that there is qualitative agreement between LES and RSM data here. However, there is a large deviation in case of the  $k - \epsilon$  model.

In Figure 4.17, the predicted axial velocity profiles at the  $0^\circ$  angle line are shown. There are outer regions close to the wall of the surface of the apex cone where the flow is directed upwards and close to the edge of the hopper where this flow in turn is directed downward. The maximum axial velocity in case of LES is about 0.48 times the inlet velocity close to the surface of the apex cone and 0.5 times the inlet velocity

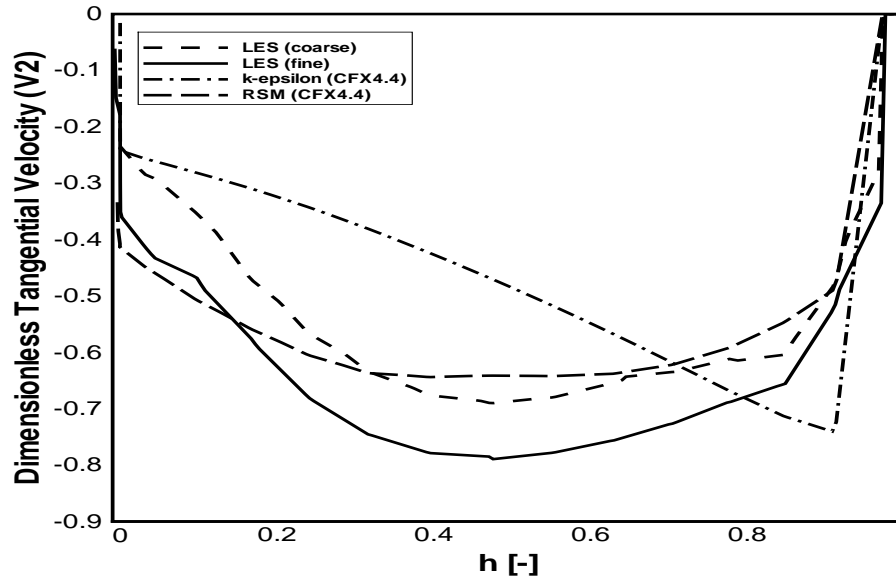


Figure 4.16: Comparison of three turbulence models, tangential velocities at cut plane 1 at  $0^\circ$ .

in case of the RSM. It was also found that there is a rough agreement between LES and RSM results compared to the poor  $k - \epsilon$  results.

In Figure 4.18, the predicted tangential velocity profiles at the  $180^\circ$  angle line are shown. Positive velocities are directed upward to the cyclone body in case of the LES and RSM models. The maximum tangential velocity at the centre of the line under investigation is about 0.74 times the inlet velocity in case of LES and 0.62 times the inlet velocity in case of RSM models. It should also be noted that there is agreement between LES and RSM, however, there is a large deviation when compared to the  $k - \epsilon$  model results.

In Figure 4.19 representing a  $180^\circ$  angle line, the predicted axial velocity profiles are shown. There are outer regions close to the wall of the surface of the apex cone where the flow is directed downwards and close to the edge of the hopper where the

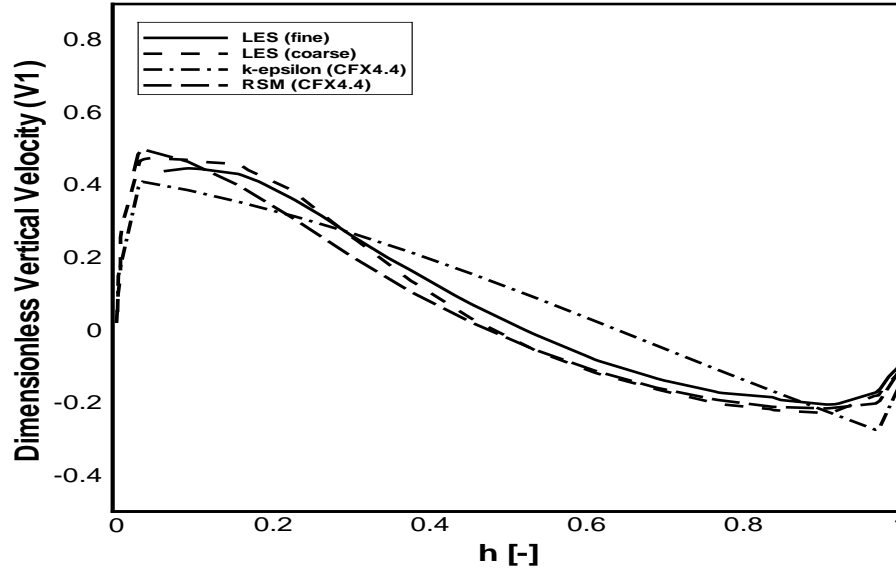


Figure 4.17: Comparison of three turbulence models, vertical velocities at cut plane 1 at  $0^\circ$ .

flow is directed upward. The maximum axial velocity in case of LES is about 0.4 times the inlet velocity close to the surface of the apex cone and 0.52 times the inlet velocity in case of the RSM model.

In Figure 4.20 representing a  $90^\circ$  angle line, the predicted tangential velocity profiles are shown. It can be noted that the maximum tangential velocity is about 0.02 times the inlet velocity in case of LES and RSM at about 60% of the line, directed downwards. The flow velocity close to the surface of the apex cone is directed downward with about 0.34 times the inlet velocity in case of LES and 0.3 times the inlet velocity with RSM. In case of the  $k - \epsilon$  model, there is a large deviation and the maximum tangential velocity tends to be close to the wall.

In Figure 4.21 representing a  $90^\circ$  angle line, the predicted axial velocity profiles are shown. The maximum axial velocity in case of LES is about 0.4 times the inlet

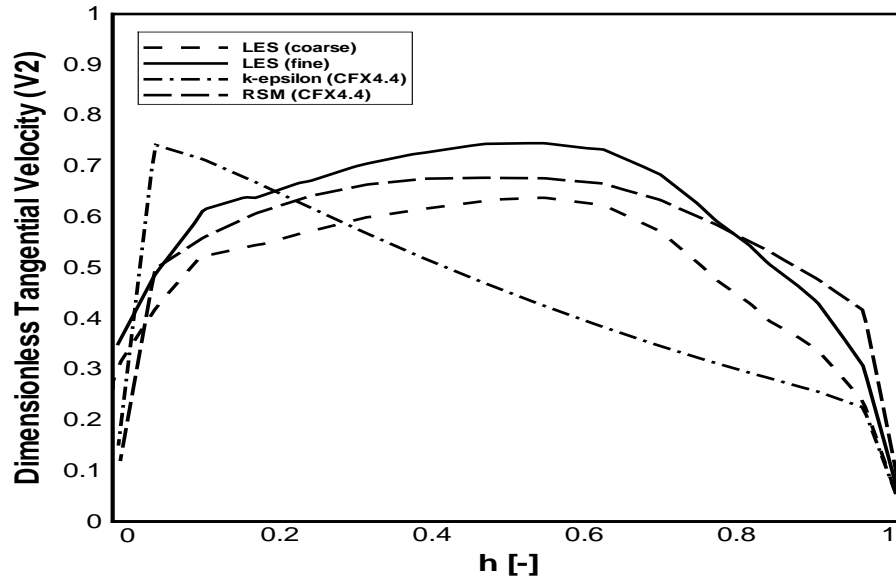


Figure 4.18: Comparison of three turbulence models, tangential velocities at cut plane 1 at  $180^\circ$ .

velocity at about 5% of the line directed upward close to the surface of the apex cone and about 0.33 times the inlet velocity at about 90% of the line directed downward close to edge of the hopper. In case of RSM the maximum axial velocity tends to be close to the surface of the apex cone at the edge of the hopper with about 0.5 times the inlet velocity directed upwards and 0.36 directed downwards, respectively. In case of  $k - \epsilon$  the maximum axial velocity tends to be close to the surface of the apex cone at the edge of the hopper with about 0.36 times the inlet velocity directed upwards and 0.18 directed downwards, respectively.

In Figure 4.22 representing a  $270^\circ$  angle line, the predicted tangential velocity profiles are shown. It can be noted that LES and RSM are not comparable in this plane. The maximum tangential velocity in case of LES is about 0.26 times the inlet velocity directed upwards at 25% of the line. In case of RSM the maximum tangential

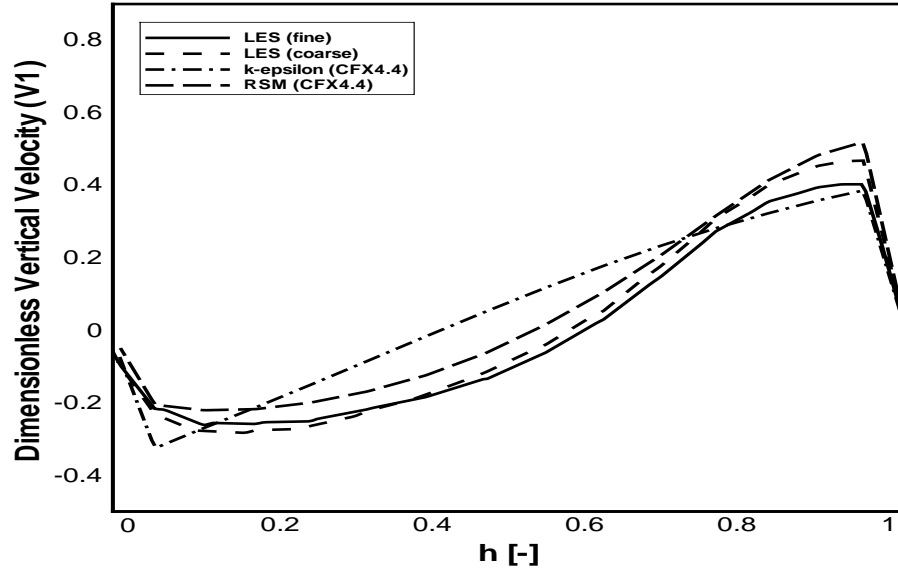


Figure 4.19: Comparison of three turbulence models, vertical velocities at cut plane 1 at  $180^\circ$ .

velocity is about 0.26 times the inlet velocity directed upwards close to the wall of the apex cone. The minimum tangential velocity in case of RSM is about 0.02 times the inlet velocity directed downwards at the centre of the line. It can also be noted that there is a bigger difference between LES, RSM and  $k - \epsilon$  results. However, the maximum tangential velocity always tends to be close to the walls.

In Figure 4.23 representing a  $270^\circ$  angle line, predicted axial velocity profiles are shown. The maximum axial velocity in case of LES and RSM is approximately 0.38 and 0.5 times the inlet velocity and located close to the surface of the apex cone. In case of  $k - \epsilon$  the maximum velocity tends to be very close to the walls with values of about 0.38 times the inlet velocity.

Finally, the flow field visualized in Figure 4.24 was gained by LES computations only. This is the average velocity field obtained at the end of the computations

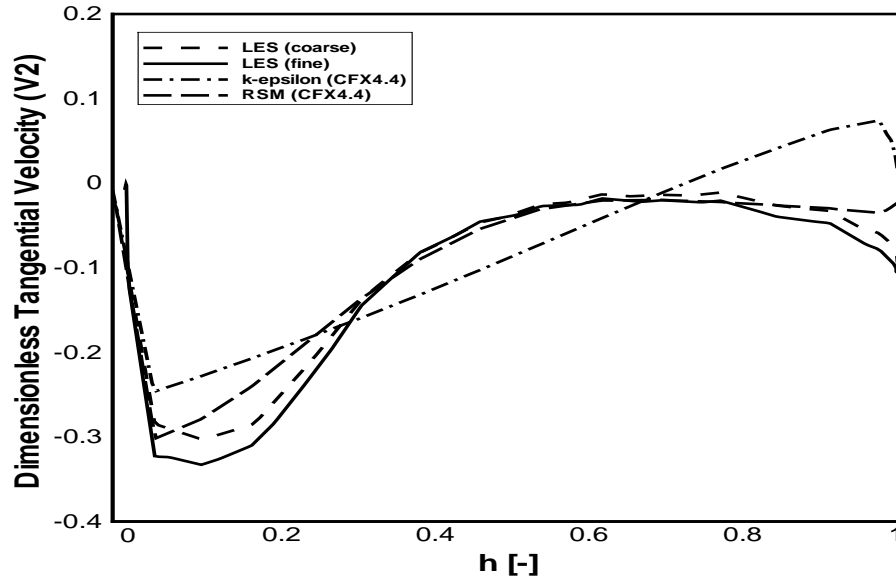


Figure 4.20: Comparison of three turbulence models, tangential velocities at cut plane 1 at  $90^\circ$ .

through an averaging over 35,000 time steps. It is shown in the upper part of the figure, that recirculating flow appears along the wall of the cylindrical part of the cyclone. Furthermore, it can be observed, that the flow is directed downwards along the outer wall of the outlet tube. In the lower part of Figure 4.24, a strong secondary flow along conical walls of the cyclone is directed downwards to the hopper. Furthermore, it can be noted that a certain amount of gas flow is entering the hopper. The gas flow is then recirculating along the surface of the apex cone back into the main cyclone body.

### 4.2.3 Pressure drop (Cyclone A)

It can be shown in Figure 4.25 that the static pressure decreases radially from wall to center and the minimum values appear in forced vortex (solid body rotation).

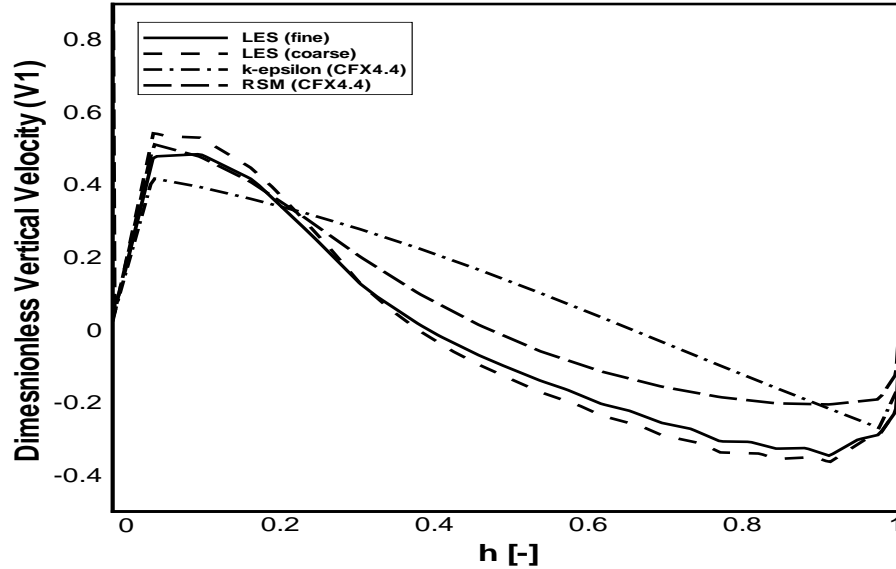


Figure 4.21: Comparison of three turbulence models, vertical velocities at cut plane 1 at  $90^\circ$ .

The pressure gradient is the largest along radial direction since there exists a highly intensified forced vortex. The pressure drop between the inlet and outlet has been predicted from the results obtained with LES using a fine grid. These computations have been carried out for various gas inlet velocities and compared with the experimental data of [107]. Figure 4.26 shows the obtained total pressure drop compared to the experimental data.

It shows that the numerical results of LES agree very well with the experiments. The difference between LES and the experiments are of the order of 2%. From the comparison between the experimental and predicted total pressure loss across the cyclone, we can conclude that LES is an appropriate tool for the modeling of flow within the cyclone A.



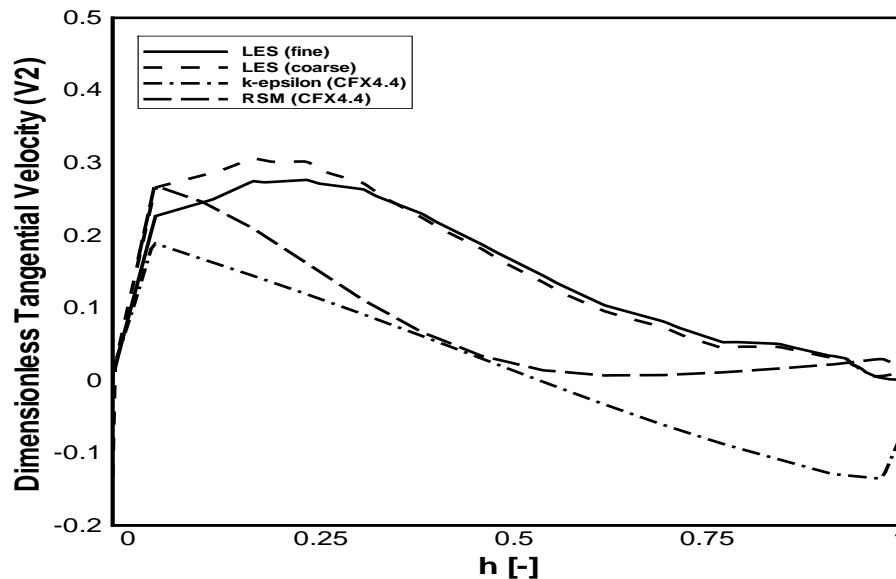


Figure 4.22: Comparison of three turbulence models, tangential velocities at cut plane 1 at  $270^\circ$ .

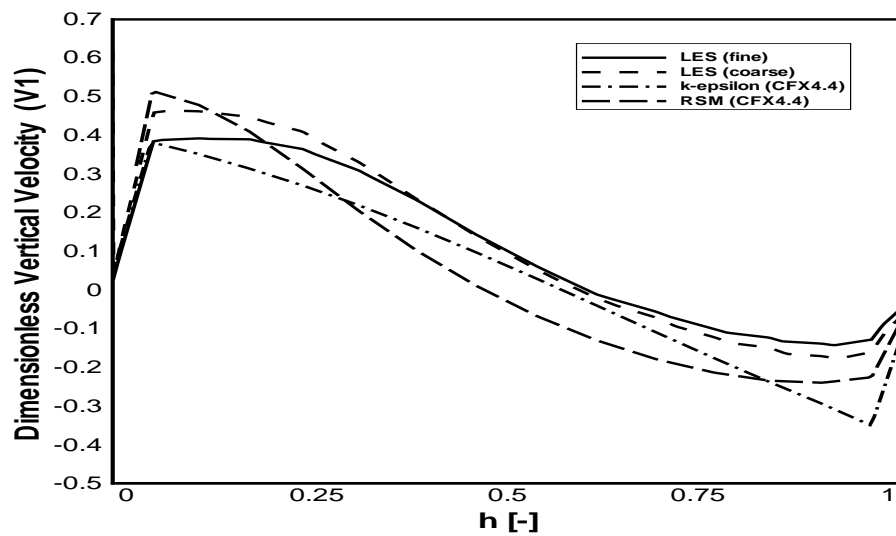


Figure 4.23: Comparison of three turbulence models, vertical velocities at cut plane 1 at  $270^\circ$ .

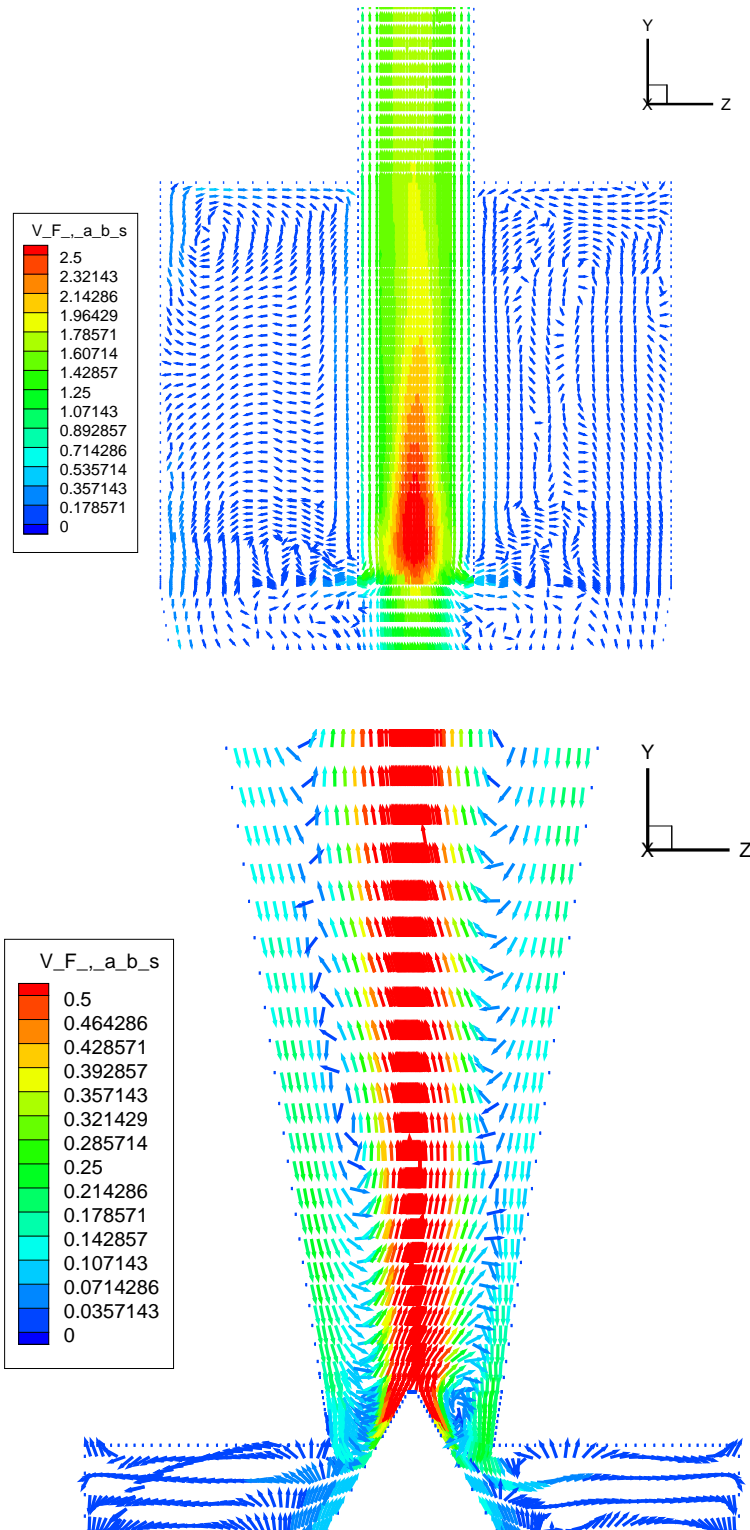


Figure 4.24: Flow field (absolute velocity in m/s ) in the upper and lower part of the cyclone (vertical mid-plane cut).

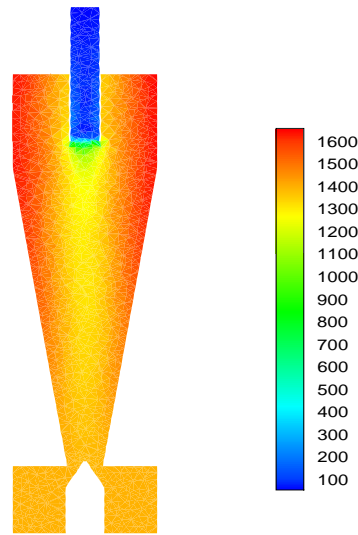


Figure 4.25: Contours of static pressure for cyclone A.

#### 4.2.4 Continuous flow predictions (Cyclone B)

The cyclone separator geometry of cyclone B is shown in Figure 4.27. Here, the comparison is based only on LES and experimental results. The predicted and measured tangential velocity profiles are shown at cut plane 1 (left) and cut plane 2 (right) in Figure 4.28. The shape of the tangential velocity profile was basically similar to cyclone A. However, in the center of the cyclone the flow is rotating like a solid body where the tangential velocity is increasing up to a certain point and then it starts to decrease towards the wall. Due to the larger outlet of cyclone B, the slope of the tangential velocity profile is not as steep as for cyclone A. The maximum tangential velocity of about 1.8 times the inlet velocity was reached at cut plane 1 at approximately half the radius. At cut plane 2, the maximum tangential velocity is about 2.1 times the inlet velocity. The tangential velocity in the outer region is not decreasing when compared to cyclone A. The LES model predicts the shape and the magnitude

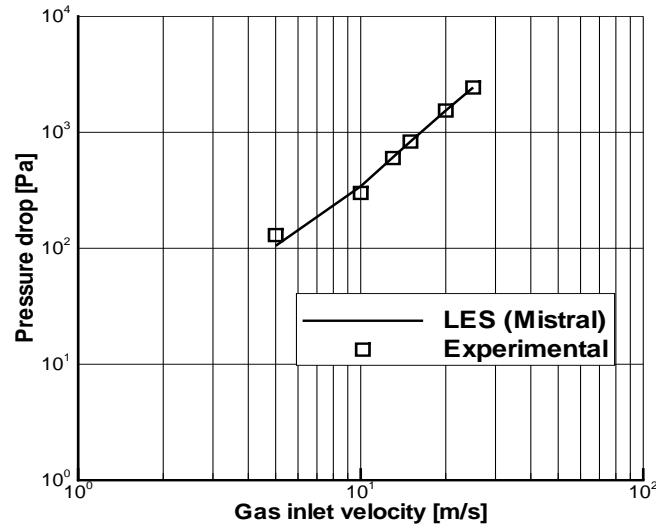


Figure 4.26: Comparison of predicted pressure loss in the cyclone for various inlet velocities with experimental data of [107] for cyclone A.

quite well when compared to the experimental data.

The predicted and measured axial velocity profiles at cut plane 1 (left) and cut plane 2 (right) are shown in Figure 4.29. Zero on the  $x$ -axis is at the center of the cyclone. Positive velocities are directed towards the outlet. Resulting from a different geometry and inlet velocity, the flow pattern in cyclone B is slightly different from cyclone A. The magnitude of the downwards axial flow close to the wall is slightly higher, maximum about 0.4 and 0.5 times the inlet velocity for cyclone B compared to 0.3 for cyclone A. Furthermore, a different flow pattern can be seen in the center of cyclone B where a core flow is going downwards through the entire cyclone length. The superiority of the LES model can be shown here. However, the more complex flow in cyclone B is difficult to predict especially for axial velocity profile. The LES model predicts a downwards flow of about 0.2 times the inlet velocity.

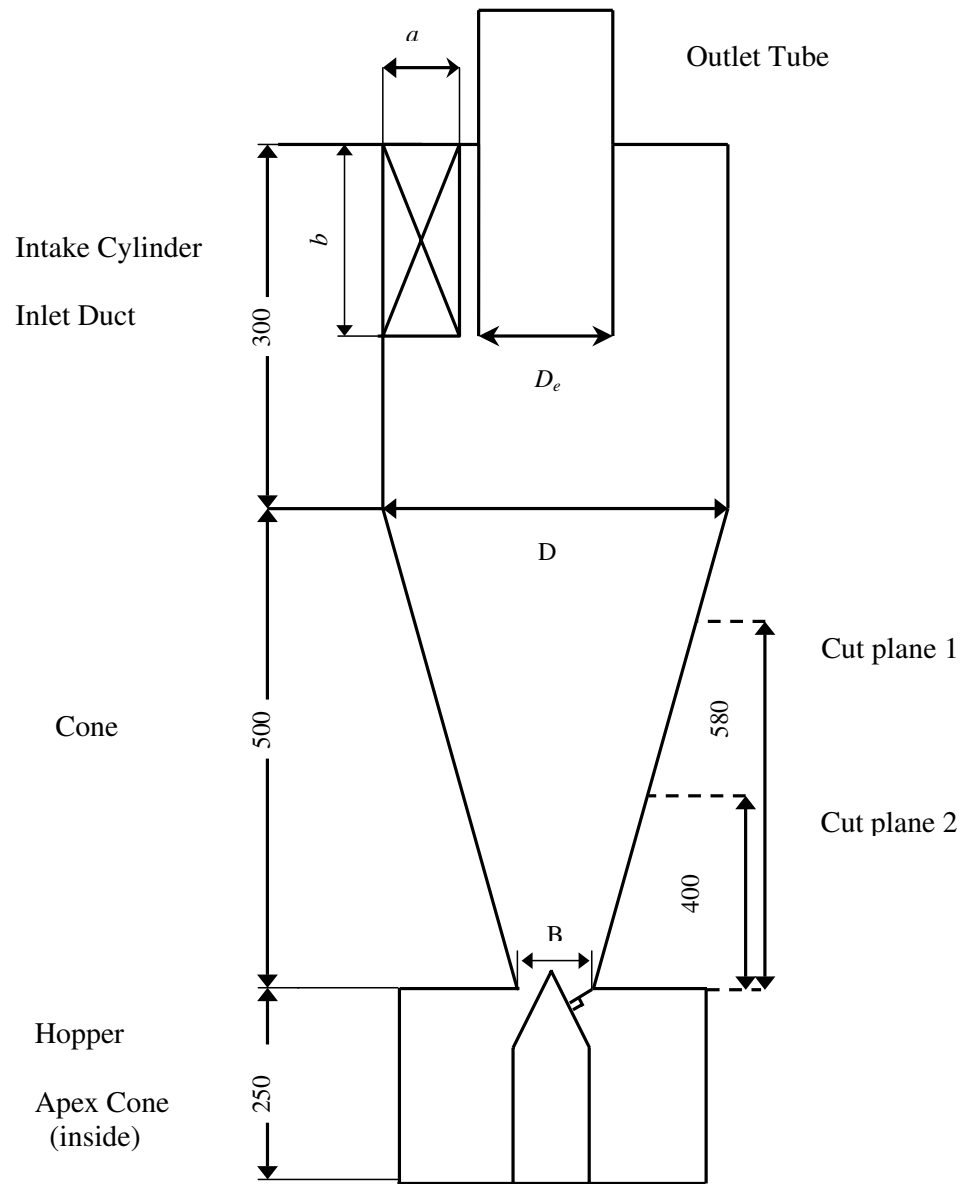


Figure 4.27: Location of different cut planes of cyclone B.

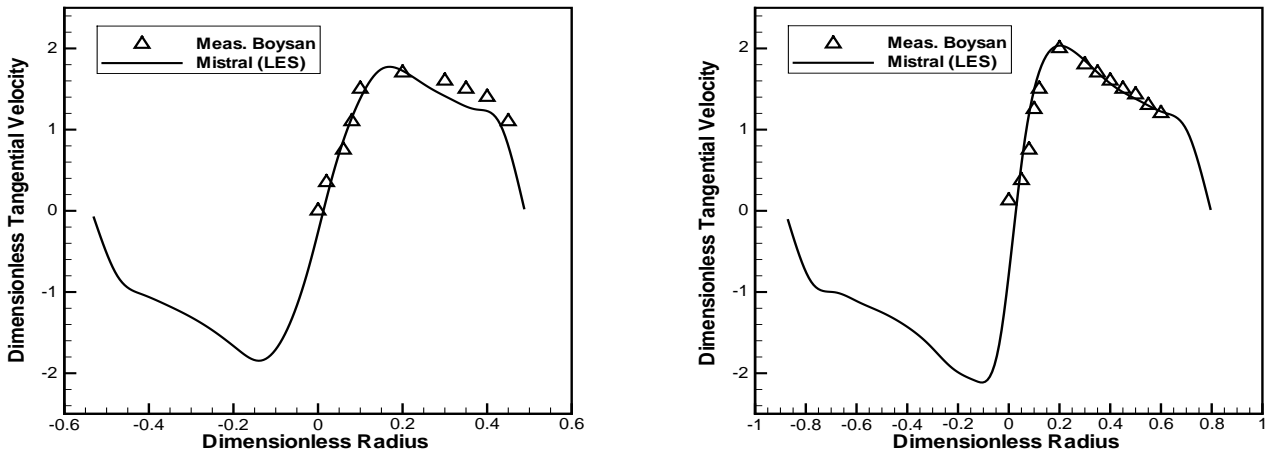


Figure 4.28: Predicted and measured tangential velocity profile at cut plane 1 (left) and cut plane 2 (right), experimental data from [104].

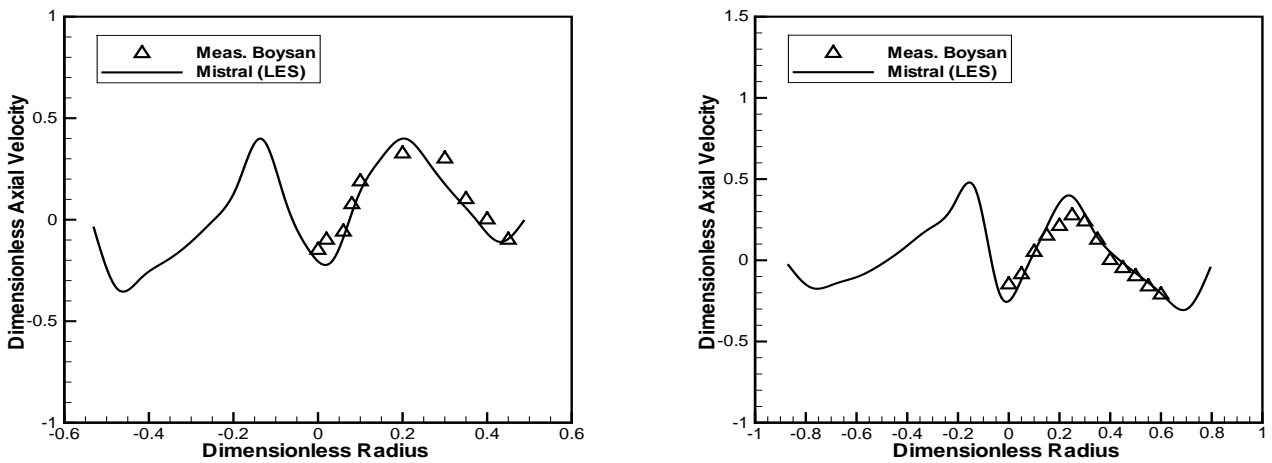


Figure 4.29: Predicted and measured axial velocity profile at cut plane 1 (left) and cut plane 2 (right), experimental data from [104].

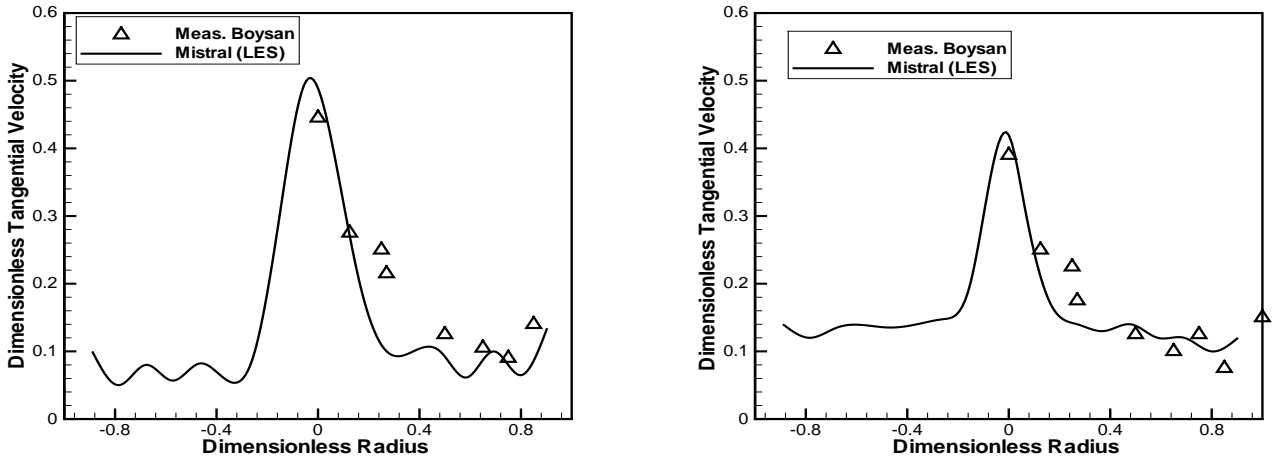


Figure 4.30: Predicted and measured r.m.s. tangential velocity profile at cut plane 1 (left) and cut plane 2 (right), experimental data from [104].

Figure 4.30 shows experimental data and predicted r.m.s tangential turbulent fluctuations  $\sqrt{w'^2}$  as a function of radius at cut plane 1 (left) and cut plane 2 (right). It can be noted that the calculated and experimental results show a good agreement. In the center of the cyclone at cut plane 1 the maximum tangential velocity fluctuation is about 0.5 times the inlet velocity compared to 0.48 in the experimental data. At cut plane 2, the maximum tangential velocity fluctuation is about 0.4 and 0.36 for the experimental data. Near the wall, the maximum tangential fluctuation is about 0.1 times the inlet velocity at cut plane 1 and 2.

In Figure 4.31 it is possible to examine measured and predicted r.m.s axial turbulent fluctuations  $\sqrt{v'^2}$  as a function of radius at cut plane 1 (left) and cut plane 2 (right). The predicted levels of the r.m.s values are between 0.15 and 0.23 times the inlet velocity. The same magnitude of predicted axial fluctuations can be observed at cut plane 2 as well. When compared to measured axial fluctuations the LES shows a

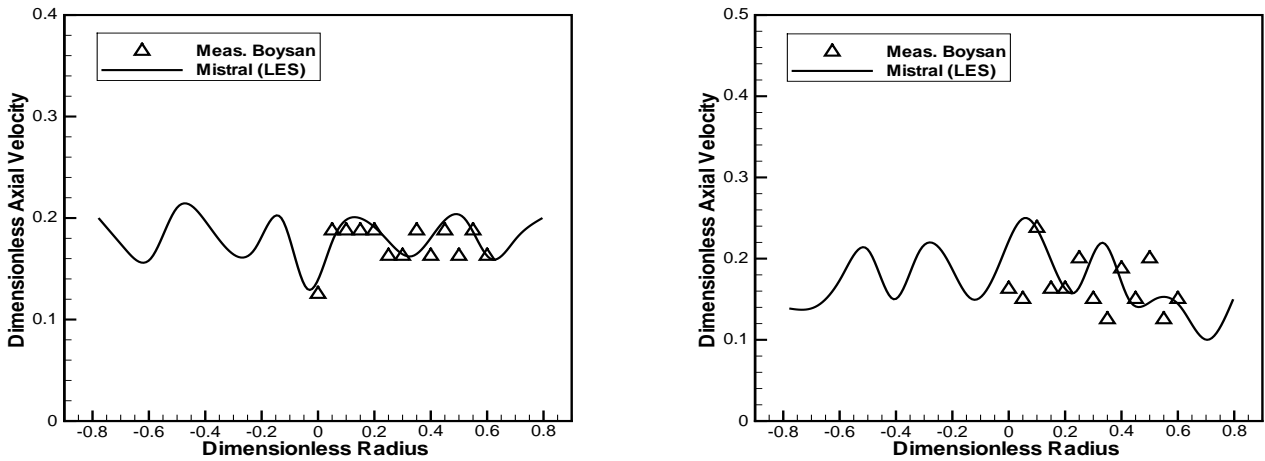


Figure 4.31: Predicted and measured r.m.s. axial velocity profile at cut plane 1 (left) and cut plane 2 (right), experimental data from [104].

good agreement.

### 4.3 Dispersed phase motion

It has been shown in the previous sections that the application of LES leads to a good agreement with the experimental data. However, it requires high computer capacity and long running times. These calculations of the continuous phase flow will now be the basis for modeling the behavior of the solid particles in the cyclone. Cyclone separation efficiency and particle trajectories will be studied in some detail. To my knowledge, there is no experimental data material available yet regarding the dispersed phase motion in Cyclone B. Therefore, the emphasis will be here mainly related to solid particles behavior in Cyclone A.



### 4.3.1 Cyclone separation efficiency (Cyclone A)

The prediction of the particle collection efficiency has been carried out in accordance to [107]. The quartz dust has a particle diameter distribution in the range of  $d_P = 0...50 \mu\text{m}$  with a mean particle diameter of  $10.9 \mu\text{m}$ . The numerical computations have been carried out for 20 particle diameter classes in the range between  $0.5...15 \mu\text{m}$ . A particle density of  $2500 \text{ kg/m}^3$  was assumed. The coefficients of restitution and kinetic friction values are 0.8 and 0.35 respectively. With an inlet gas velocity of 20 m/s, series of separation rates were performed. The separation rate can be calculated by:

$$T(d_P) = 1 - \frac{\dot{N}_{out}(d_P)}{\dot{N}_{in}(d_P)} \quad (4.3.1)$$

where  $\dot{N}_{in}(d_P)$  and  $\dot{N}_{out}(d_P)$  are the particle flow rates for a given particle size in the inlet cross section and gas exit cross section respectively. The particle is assumed to be collected in the cyclone, if:

- the particle trajectory reaches the inlet cross section of the particle hopper
- the particle sticks to the wall of the cyclone
- the particle residence time in the cyclone is larger than the maximum allowed computation time

Figure 4.32 shows the comparison of the predicted separation efficiency with the experimental results of [107] at an inlet gas velocity of 20 m/s. The figure presents a very satisfying agreement between LES and experimental results. The shape of the efficiency curve is approximately identical.

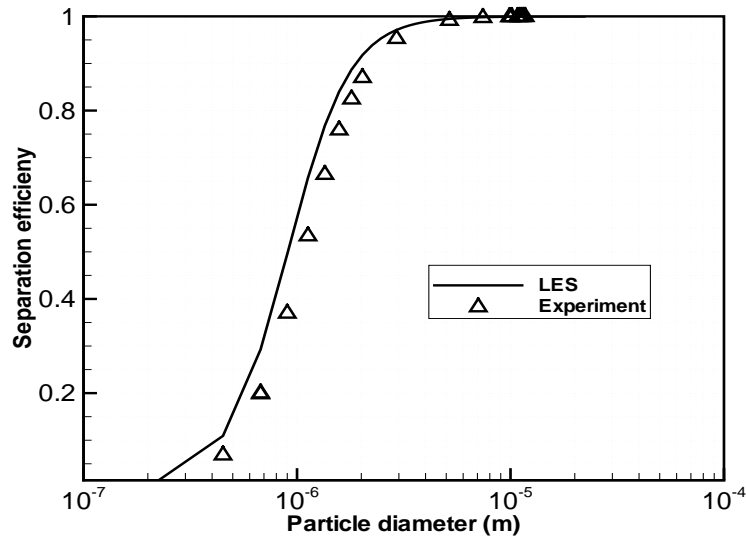


Figure 4.32: Comparison of predicted cyclone separation efficiency with experimental data of [107] for cyclone A.

### 4.3.2 Particle trajectories (Cyclone A)

Figure 4.33 shows examples of particle trajectories with residence time in the cyclone with an inlet gas velocity of 20 m/s. Figure 4.33 (left) shows a smaller particle, which is captured by the secondary flow along the cyclone lid and follows the secondary flow along the wall of the vortex finder tube to the outlet gas exit. Figure 4.33 (right) shows a particle with  $1.0 \mu\text{m}$  moving along the outer conical wall to the particle hopper. Because of its small size it cannot follow to be collected. It follows the recirculating gas flow back into the cyclone body where it is separated and captured into the vortex core and moves upward to the outlet gas exit. A slightly larger particle of  $1.3 \mu\text{m}$  in Figure 4.34 is first captured in a particle rope along the cyclone lid. However, it is too large to follow the recirculating flow to the vortex finder tube. Therefore, it can be separated and moves down to the particle hopper where it is collected.

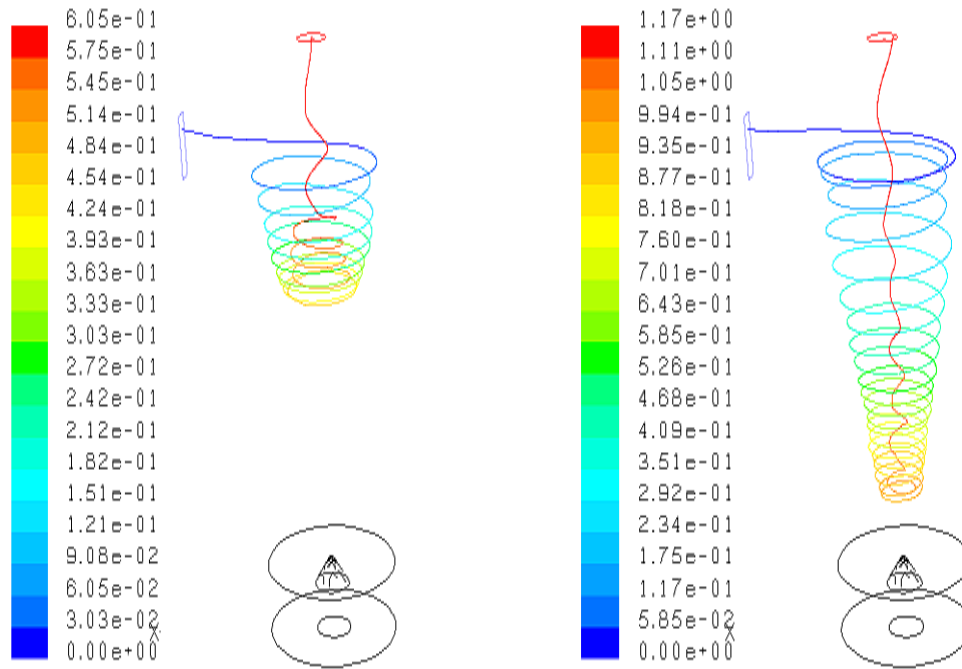


Figure 4.33: Particle trajectories with residence time (second) at different particle diameters of 0.5 (left) and 1.0 (right)  $\mu\text{m}$  of cyclone A.

Figure 4.35 shows the particle trajectories with particle diameters ranged from  $0.5\mu\text{m}$  to  $10.5\mu\text{m}$ . It can be seen that the trajectory of the largest particles is at the downside of the cyclone and the trajectory of the smallest particles is at the up of the cyclone. Moreover, the large particles are collected while the small particles escape from the outlet pipe of the cyclone. The particles with the smallest diameter can not move outward to the wall of the cyclone since the centrifugal force on them is not exceeding the strength of the gas drag force.

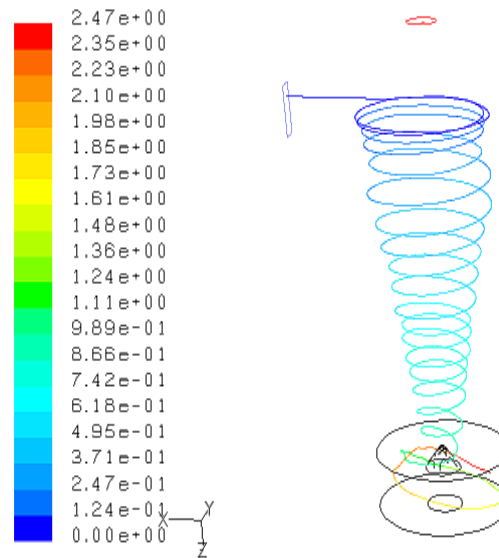


Figure 4.34: Particle trajectories with residence time (second) at  $1.3 \mu\text{m}$  of cyclone A.

## 4.4 Conclusion

The results of LES in case of the complex flow in a cyclone separator compare well with the measurement data found in the literature. Therefore, the LES results are very encouraging and have shown that this model is a better alternative to conventional turbulence modeling of cyclone separators. The dynamic behavior of the flow has been captured, providing important information on the flow structure within the cyclone.

Furthermore, the LES results of the continuous phase flow form the basis for modelling solid particle motion in the cyclone, based on one-way coupling between the gas flow field and the disperse phase. The pressure drop inside the cyclone has been studied with a fine grid for various gas inlet velocities. In the flow field, solid particles of various sizes are released to predict the cyclone separation efficiency. Here, one-way coupling between the gas and the particles is assumed. The predicted cyclone

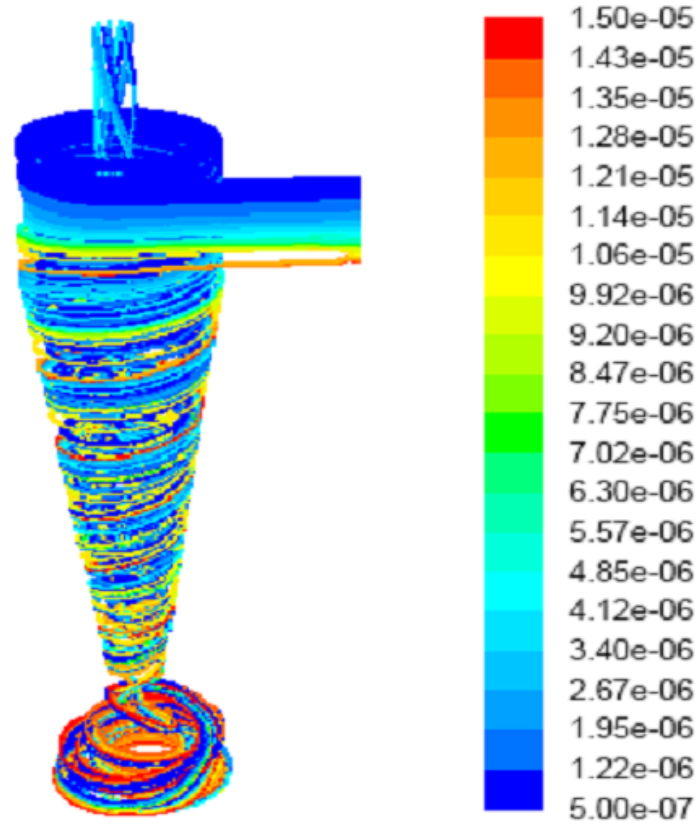


Figure 4.35: Particle trajectories with the particle diameters (meter) distribution at different particle diameter  $d_P$  in range from  $0.5 \mu\text{m}$  to  $10.5 \mu\text{m}$  for cyclone A.

separation efficiency results of LES show satisfying agreement with experimental data.

With these results, the potential of the LES model to simulate flows in a cyclone separator has been distinctly demonstrated. Eventually, we hope that this work will contribute to an improved understanding of the flow and separation process within cyclone separators.

# Chapter 5

## Concluding Remarks and future work

The nature of the gas flow of a particle cyclone separator is highly swirling with anisotropic turbulence. Therefore, advanced turbulence models such as RSM and LES have to be applied to predict the gas flow behavior rather than the meanwhile classical  $k - \epsilon$  turbulence model.

Turbulent secondary flows inside a straight square channel have been investigated numerically using LES in order to verify and validate the implementation process. The results of the high Reynolds number investigations at  $Re = 35,000$  and  $Re = 100,000$  reveal that the mechanisms driving the secondary flows resemble the low Reynolds number case at  $Re = 5000$ . The magnitude of the maximum secondary velocity at a Reynolds number of  $Re = 5000$  is 1.5% of the bulk velocity (at  $Re = 35,000$  it is 2.33%). At a Reynolds number of  $Re = 100,000$  the magnitude of the maximum secondary velocity reaches 2.67%. Prandtl's secondary motion calculated by the LES shows satisfying agreement with Direct Numerical Simulation (DNS).

After that, numerical calculations of two different cyclones with geometrical *swirl numbers*  $S_g$  of 3.5 and 4 have been carried out. Furthermore, comparisons have been

made between three turbulence models ( $k - \epsilon$ , RSM and LES) and experimental data at  $S_g = 3.5$ . Moreover, the comparisons have been carried out between the LES model and experimental results at  $S_g = 4$ .

Our calculations confirm, that in case of cyclone continuous phase flows the  $k - \epsilon$  model generates weak results. The reason for the poor performance of the  $k - \epsilon$  model is that the important assumption of isotropic turbulence does not hold in flows with non-uniform pressure distributions such as swirling flows.

The predicted data from the RSM investigations were not as good as the LES data. The tangential velocity profiles showed that with RSM we tend to obtain a solid body rotation, which reached too far towards the external wall. RSM calculations using a central advection scheme for the momentum equations should be used in future investigations rather than the higher order QUICK scheme. Also, the linear approach for the pressure strain term in the LRR model seems to be inadequate for such swirling flows.

The results of LES in case of the complex flow in a cyclone compare very well with the measurement data found in the literature. They are even acceptable when using a coarse-grid. This is one key result of the investigations. Therefore, the LES results are very encouraging and have shown that this model is a better alternative to conventional turbulence modeling of cyclone separators. Depending on a different geometry and inlet velocity, the flow pattern at  $S_g = 4$  is slightly different compared to  $S_g = 3.5$ . The magnitude of the downward axial flow close to the wall is slightly higher. Furthermore, different flow patterns have been noted in the center of the cyclone at  $S_g = 4$ , where a core flow is going downwards over the entire cyclone length. The dynamic behavior of the flow has been captured, providing important

information on the flow structure within the cyclone at  $S_g = 3.5$ .

Also, the LES results of the continuous phase flow formed the basis for modelling solid particle motion in the cyclone based on one-way coupling between the gas flow field and the disperse phase. The pressure drop inside the cyclone has been studied using a fine grid at various gas inlet velocities. The difference between LES and available experimental pressure drop data is very small around 2%. Sample particle trajectories in the cyclone with an inlet particle velocity of 20 m/s have been presented and discussed.

In the flow field, solid particles of various sizes are released to predict the cyclone separation efficiency. Here, one-way coupling between the gas and the particles was assumed. The cyclone separation efficiency results of LES show a satisfying agreement with experimental data.

With these results, the potential of the LES model to simulate flows in a cyclone separator has been distinctly demonstrated. Eventually, we hope that this work will contribute to an improved understanding of the flow and separation process within cyclone separators in order to optimise their technical concepts and encourage researchers to apply LES to calculate particle separation processes.

In future work one should generate further experimental laboratory data especially at the apex cone area in order to further validate the presented numerical results. Moreover, numerical investigation of the separation area between the cone and the hopper could be carried out by using Direct Numerical Simulation (DNS). These results should be compared with LES data in order to further evaluate the LES accuracy.



# List of Figures

1.1	Schematic of the cyclone separator principle. . . . .	4
2.1	A sketch of the Kolmogorov energy spectrum of homogeneous turbulence. The straight section of the curve between the integral scale $l$ and the viscous micro scale $\eta$ has a slope of $-5/3$ . . . . .	17
2.2	Decomposition of the energy spectrum in the solution encountered with large eddy simulation [45]. . . . .	28
2.3	Commonly used filter kernels. . . . .	30
3.1	Transverse force on a rotating particle in a parallel flow. . . . .	40
3.2	Transverse force on a particle in a shear flow. . . . .	43
3.3	Sketch of a particle path in a control volume. . . . .	50
3.4	Wall roughness effect with the particle. . . . .	52
3.5	Particle-wall collision of a spherical particle with an inclined virtual wall.	52
4.1	Schematic of the channel geometry and numerical grid. . . . .	60
4.2	Isocontours of the mean streamwise velocity in a cross-section of the channel at a low Reynolds number of 5000 [51]. . . . .	64

4.3	Secondary flow of the time-averaged flow field of the channel at $Re = 5000$ (left) and $Re = 35,000$ (right), at $x = 0.3$ m [51]. . . . .	65
4.4	Secondary flow of the time-averaged flow field of the channel at $Re = 100,000$ , at $x = 0.3$ m [51]. . . . .	66
4.5	Maximum secondary velocity in percentage of the normal velocity versus $Re$ . . . . .	67
4.6	Schematic of the cyclone geometry and numerical grid. . . . .	71
4.7	Location of different cut planes of cyclone A. . . . .	74
4.8	Apex cone frontal view, line under investigation normal to the apex cone surface towards the edge. . . . .	75
4.9	Apex cone top view. . . . .	76
4.10	Comparison of three turbulence models and experimental data of reference [103], tangential velocities at cut plane 2. . . . .	77
4.11	Comparison of three turbulence models and experimental data of reference [103], axial velocities at cut plane 2. . . . .	78
4.12	Comparison of three turbulence models and experimental data of reference [103], tangential velocities at cut plane 3. . . . .	79
4.13	Comparison of three turbulence models and experimental data of reference [103], axial velocities at cut plane 3. . . . .	80
4.14	Comparison of three turbulence models and experimental data of reference [103], tangential velocities at cut plane 4. . . . .	81
4.15	Comparison of three turbulence models and experimental data of reference [103], axial velocities at cut plane 4. . . . .	82

4.16	Comparison of three turbulence models, tangential velocities at cut plane 1 at $0^\circ$ . . . . .	83
4.17	Comparison of three turbulence models, vertical velocities at cut plane 1 at $0^\circ$ . . . . .	84
4.18	Comparison of three turbulence models, tangential velocities at cut plane 1 at $180^\circ$ . . . . .	85
4.19	Comparison of three turbulence models, vertical velocities at cut plane 1 at $180^\circ$ . . . . .	86
4.20	Comparison of three turbulence models, tangential velocities at cut plane 1 at $90^\circ$ . . . . .	87
4.21	Comparison of three turbulence models, vertical velocities at cut plane 1 at $90^\circ$ . . . . .	88
4.22	Comparison of three turbulence models, tangential velocities at cut plane 1 at $270^\circ$ . . . . .	89
4.23	Comparison of three turbulence models, vertical velocities at cut plane 1 at $270^\circ$ . . . . .	89
4.24	Flow field (absolute velocity in m/s ) in the upper and lower part of the cyclone (vertical mid-plane cut). . . . .	90
4.25	Contours of static pressure for cyclone A. . . . .	91
4.26	Comparison of predicted pressure loss in the cyclone for various inlet velocities with experimental data of [107] for cyclone A. . . . .	92
4.27	Location of different cut planes of cyclone B. . . . .	93
4.28	Predicted and measured tangential velocity profile at cut plane 1 (left) and cut plane 2 (right), experimental data from [104]. . . . .	94

4.29	Predicted and measured axial velocity profile at cut plane 1 (left) and cut plane 2 (right), experimental data from [104]. . . . .	94
4.30	Predicted and measured r.m.s. tangential velocity profile at cut plane 1 (left) and cut plane 2 (right), experimental data from [104]. . . . .	95
4.31	Predicted and measured r.m.s. axial velocity profile at cut plane 1 (left) and cut plane 2 (right), experimental data from [104]. . . . .	96
4.32	Comparison of predicted cyclone separation efficiency with experimental data of [107] for cyclone A. . . . .	98
4.33	Particle trajectories with residence time (second) at different particle diameters of 0.5 (left) and 1.0 (right) $\mu\text{m}$ of cyclone A. . . . .	99
4.34	Particle trajectories with residence time (second) at 1.3 $\mu\text{m}$ of cyclone A. . . . .	100
4.35	Particle trajectories with the particle diameters (meter) distribution at different particle diameter $d_P$ in range from 0.5 $\mu\text{m}$ to 10.5 $\mu\text{m}$ for cyclone A. . . . .	101

# Bibliography

- [1] A Gorton-Hülgerth. *Messung und Berechnung der Geschwindigkeitsfelder und Partikelbahn im Gaszyklon*. PhD thesis, Technical University of Graz, Austria, 1999.
- [2] J.P. Minier, O. Simonin, and M. Gabillard. Numerical modelling of cyclone separators. *Proceedings of the International Conference on Fluidized Bed Combustion, Quebec, Canada, April*, 3:1251–1259, 1991.
- [3] F. Boysan, J. Swithenbank, and W.H. Ayers. Mathematical modelling of gas-particle flows in cyclone separators. In *Encyclopedia of Fluid Mechanics*, volume 4 Solids and Gas-Solids Flows, Chapter 42. Gulf Publishing Company, Houston, Texas, 1986.
- [4] F. Boysan, W.H. Ayers, and J. Swithenbank. A fundamental mathematical modelling approach to cyclone design. *Trans Inst Chem Eng*, V 60(N 4):222–230, 1982.
- [5] G. Staudinger, S. Obermaier, and C. Meisel. Treffsicherheit und Zuverlässigkeit der heutigen Zyklonberechnung. Technical Report VDI-Bericht 1511, pp. 1-23, VDI-Verlag, 1999.

- [6] VDI-Gesellschaft Energietechnik. Zyklonabscheider in der Energie- und Verfahrenstechnik. *Tagung Essen, 29-30 Oktober VDI-Berichte 1290, VDI-Verlag, Düsseldorf, 1996.*
- [7] VDI-Gesellschaft Energietechnik. Zyklonabscheider in der Energie- und Verfahrenstechnik. *Tagung Leverkusen, 27-28 Oktober VDI-Berichte 1511, VDI-Verlag, Düsseldorf, 1999.*
- [8] T. Frank and E. Wassen. Parallel efficiency of PVM- and MPI-implementations of two algorithms for the lagrangian prediction of disperse multiphase flows. In *ISAC '97 Conference on Advanced Computing on Multiphase Flow*, Tokyo, Japan, July 18-19,1997. JSME Centennial Grand Congress 1997.
- [9] T. Frank, E. Wassen, and Q. Yu. Lagrangian prediction of disperse gas-particle flow in cyclone separators. In *ICMF '98 -3rd International Conference on Multiphase Flow, June 8.-12. CD-ROM Proceedings, Paper No. 217*, Lyon, France, 1998.
- [10] T. Frank, E. Wassen, and Q. Yu. A 3-dimensional lagrangian solver for disperse multiphase flows on arbitrary, geometrically complex flow domains using block structured numerical grids. In ASME Fluid Engineering Division Summer Meeting, editor, *Proceedings of the 7th Int. Symposium on Gas-Particle Flows*, Vancouver, BC, Canada, June 22-26, 1997. ASME Fluid Engineering Division Summer Meeting.
- [11] T. Frank, Q. Yu, E. Wassen, and J. Schneider. Experimental and numerical investigation of particle separation in a symmetrical double cyclone separator. *Proceedings of the 1999 3rd ASME/JSME Joint Fluids Engineering Conference, FEDSM'99, San Francisco, California, USA, 18-23 July, 1999.*
- [12] J. Derksen. LES - based separation performance predictions of a stairmand cyclone. *10th Workshop on Two - Phase Flow Predictions, Martin - Luther-*

*Universität Halle - Wittenberg, Halle (Saale), Germany*, pages 217–226, 9 - 12 April 2002.

- [13] F. Souza and A. Neto. Large eddy simulations of a hydrocyclone. In *Proceedings of FEDSM ASME Fluid Engineering Division Summer Meeting, Montreal*, pages 1 – 6, Quebec, Canada, 14 - 18 July 2002.
- [14] R.-G. Huang, B.-W. Huan, and S.-P. Zhang. Partitioning parallel procedure for numerical simulation of gas flow in a cyclone separator. *Journal of Hydrodynamics*, 14(1):52–58, 2002.
- [15] D.B. Ingham and L. Ma. Predicting the performance of air cyclones. *International Journal of Energy Research*, 26(7):633–652, 2002.
- [16] K. Pant, C.T. Crowe, and P. Irving. On the design of miniature cyclones for the collection of bioaerosols. *Powder Technology*, 125(2-3):260–265, 2002.
- [17] C.A. Ho and Sommerfeld M. Numerical study on the effect of agglomeration for the particle separation in a gas cyclone. In *Proceedings of the ASME/JSME Joint Fluids Engineering Conference*, volume 1 B, pages 1315–1317, 2003.
- [18] T. Lu, L. Qiu, S. Wang, and D. Zhao. The computer simulation - design and application for the double-stage separating cyclone separator. In *Energy and the Environment - Proceedings of the International Conference on Energy and the Environment, Halkidiki, Greece*, volume 2, pages 1775–1779, 2003.
- [19] K. Matsuzaki, M. Munekata, and H. Ohba. Direct numerical simulation of gas-particle turbulent swirling flows in an axially rotating pipe. In *Proceedings of the ASME/JSME Joint Fluids Engineering Conference*, volume 2 B, pages 1379–1384, 2003.

- [20] L.M. Portela and R.V.A. Oliemans. Eulerian-Lagrangian DNS/LES of particle-turbulence interactions in wall-bounded flows. *International Journal for Numerical Methods in Fluids*, 43(9):1045–1065, 2003.
- [21] J. Ran, L. Zhang, and M. Xin. Numerical simulation of gas-solid flow motion characteristics and deposition efficiency of particles in water-film cyclone separator. *Huagong Xuebao/Journal of Chemical Industry and Engineering (China)*, 54(10):1391–1396, 2003.
- [22] A. Suguri, K. Toda, and M. Yamamoto. Numerical investigation on small-scale cyclone for spm removal. *Proceedings of the ASME/JSME Joint Fluids Engineering Conference*, 1 B:805–810, 2003.
- [23] H.-G. Wang and S. Liu. Application and comparison of different turbulence models in the three-dimensional numerical simulation of cyclone separators. *Re-neng Dongli Gongcheng/Journal of Engineering for Thermal Energy and Power*, 18(4):337–342, 2003.
- [24] X.-L. Wu, J.-H. Shentu, and Z.-L. Ji. Numerical simulation of three-dimension flow field in a pv type cyclone. *Shiyou Xuebao, Shiyou Jiagong/Acta Petrolei Sinica (Petroleum Processing Section)*, 19(5):74–79, 2003.
- [25] L. Xiaodong, Y. Jianhua, C. Yuchun, N. Mingjiang, and C. Kefa. Numerical simulation of the effects of turbulence intensity and boundary layer on separation efficiency in a cyclone separator. *Chemical Engineering Journal*, 95(1):235–240, 2003.
- [26] H. Yoshida, Y. Kwan-Sik, K. Fukui, S. Akiyama, and S. Taniguchi. Effect of apex cone height on particle classification performance of a cyclone separator. *Advanced Powder Technology*, 14(3):263–278, 2003.



- [27] Z. Chao, G. Sun, B. Gong, and M. Shi. Numerical simulation and experimental study on gas flow field in a rough-cut cyclone separator. *Petroleum Processing and Petrochemicals*, 35(7):57–61, 2004.
- [28] L. Hu, L. Zhou, J. Zhang, and M. Shi. Numerical simulation of 3-d strongly swirling turbulent flow in a cyclone separator. *Qinghua Daxue Xuebao/Journal of Tsinghua University*, 44(11), 2004.
- [29] D. Snider, K. Williams, and R.A. Johnson. Multiphase particle-in-cell simulations of dense-phase flows in cyclone separators. *Proceedings of the ASME Heat Transfer/Fluids Engineering Summer Conference 2004, HT/FED 2004*, 3:777–785, 2004.
- [30] S.-Y. Liu, B.-G. Wang, and Y. Zhang. Cyclone separator three-dimensional turbulent flow-field simulation using the Reynolds stress model. *Beijing Ligong Daxue Xuebao/Transaction of Beijing Institute of Technology*, 25(5), 2005.
- [31] X.-H. Xue, Y.-D. Wei, G.-G. Sun, and M.-X. Shi. Numerical simulation on the secondary eddies in the upper space of a cyclone separator. *Kung Cheng Je Wu Li Hsueh Pao/Journal of Engineering Thermophysics*, 26(2):243–245, 2005.
- [32] K. Matsuzaki, Y. Kudo, H. Ohba, and M. Munekata. A study on swirling flows in a cyclone separator (application of large eddy simulation). *Nihon Kikai Gakkai Ronbunshu, B Hen/Transactions of the Japan Society of Mechanical Engineers, Part B*, 71(702):480–486, 2005.
- [33] A. K. Gupta, D. G. Lilly, and N. Syred. *Swirl Flows*. Abacus Press, Tunbridge Wells, U.K, 1984.
- [34] A. N. Kolmogorov. The local structure of turbulence in incompressible viscous fluid for very large Reynolds numbers. *C.R. Acad. Sci.*, 30:301, 1941.

- [35] U. Piomelli and E. Balaras. Wall-layer models for large eddy simulations. *Ann. Rev. Fluid Mech.*, 34:349–374, 2002.
- [36] J.H. Ferziger and M. Perić. *Computational Methods for Fluid Dynamics*. Springer, Berlin, 1999.
- [37] P. Sagaut. *Large Eddy Simulation for Incompressible Flows. An Introduction*. Springer, Heidelberg, 2001.
- [38] B.E. Launder, G.J. Reece, and W. Rodi. Progress in the development of a Reynolds-stress turbulence closure. *J Fluid Mech.*, 68(pt 3):537–566, 1975.
- [39] W. P. Jones and B. E. Launder. The prediction of laminarization with a two-equation model of turbulence. *Int. J. Heat Mass Transfer*, 15:301–314, 1972.
- [40] V.C Patel, W. Rodi, and J. Schneider. Turbulence models for near-wall and low-Reynolds-number flows: A review. *AIAA j.*, 23:1308–1319, 1985.
- [41] D.C. Wilcox. *Turbulence modeling for CFD*. DCW Industries, Inc., La Canada, California, 2002.
- [42] B.E. Launder and D.B. Spalding. The numerical computation of turbulent flows. *Computer Methods in Applied Mechanics and Engineering*, 3(2):269–289, 1974.
- [43] J.M. Österlund, A.V. Johansson, and M.N. Hassan. A note on the intermediate region in turbulent boundary layers. *Phys. Fluids*, 12(9):2360–2363, 2000.
- [44] T.J. Craft, B.E. Launder, and K. Suga. A non-linear eddy viscosity model including sensitivity to stress anisotropy. In *Proc. 10th Symp. Turbulent Shear Flows*, Pen. State Univ., August, 1995.
- [45] M. Lesieur and O. Métais. New trends in large-eddy simulations of turbulence. *Annual Review of Fluid Mechanics*, 28:45–82, 1996.

- [46] J.H. Ferziger. Large eddy simulations of turbulent flows. *AIAA Journal*, 15(9):1261–1267, 1977.
- [47] P.J. Mason. Large-eddy simulation: A critical review of technique. *Q.J.R. Meteorol. Soc.*, 120:1–26, 1994.
- [48] R.S. Rogallo and P. Moin. Numerical simulation of turbulent flows. *Ann. Rev. Fluid Mech.*, pages 99–137, 1984.
- [49] A. Leonard. Energy cascade in large eddy simulations of turbulent fluid flows. *Adv. Geophys.*, 18A,237, 1974.
- [50] J. Smagorinsky. General circulation experiment with the primitive equations. *Mon. Weather Rev.*, 91:99–164, 1963.
- [51] H. Shalaby, K. Pachler, K. Wozniak, and G. Wozniak. Numerical simulation of turbulent flow through a straight square channel. *PAMM*, 4(1):652–653, 2004.
- [52] J. Denev, T. Frank, and K. Pachler. Large eddy simulation (LES) of turbulent square channel flow using a PC-cluster architecture. *Proceedings of the 4th International Conference on Large-scale Scientific Computations, Sozopol, Bulgaria.*, pages 1 – 11, 2003.
- [53] E.R. van Driest. On the turbulent flow over a wall. *J. Aeronautical Science*, 23:1007 – 1011, 1965.
- [54] O.J. McMillan, J.H. Ferziger, and R.A. Rogallo. Tests of new subgrid scale models in strained turbulence. *Paper 80-1339, AIAA*, 1980.
- [55] Y. Yakhot and S.A. Orszag. Renormalization group analysis of turbulence. I. Basic theory. *Journal of Scientific Computing*, 1(1):3–51, 1986.

- [56] U. Piomelli, J. Ferziger, P. Moin, and J. Kim. New approximate boundary conditions for large eddy simulations of wall-bounded flows. *Phys. Fluids*, 1:1061–1068, 1989.
- [57] CFX 4.4 ANSYS GmbH. CFX solver documentation, 1998.
- [58] T. Frank. Parallele Algorithmen für die numerische Simulation dreidimensionaler, disperser Mehrphasenströmungen und deren Anwendung in der Verfahrenstechnik. *Habilitationsschrift, TU-Chemnitz, Germany*, 2002.
- [59] E. Schreck and M. Perić. Parallelization of implicit solution methods. *ASME Fluid Engineering Conference, June 22-23, Los Angeles (CA), USA*, 1992.
- [60] L.S. Carretto, A.D. Gosman, S.V. Patankar, and D.B. Spalding. Two calculation procedures for steady, three-dimensional flows with recirculation. *Proc. 3rd Int. Conf. Num. Methods Fluid Dyn., Paris, Vol. II*, page 60, 1972.
- [61] H.L. Stone. Iterative solution of implicit approximations of multidimensional partial differential equations. *SIAM J. Numer. Anal.*, 5:530–558, 1968.
- [62] K. Bernert, Th. Frank, H. Schneider, and K. Pachler. Multi-grid acceleration of a SIMPLE based CFD code and aspects of parallelization. *IEEE International Conference on Cluster Computing - CLUSTER 2000, November 2, Chemnitz, Germany*, 2000.
- [63] C.T. Crowe. On the relative importance of particle-particle collisions in gas-particle flows. *Proc. Conf. on Gas Borne Particles. Paper C78/81*, pages 135–137, 1981.
- [64] C.T. Crowe, M. Sommerfeld, and Y. Tsuji. *Multiphase Flows with Droplets and Particles*. CRC Press, New York, 1998.

- [65] R. Clift, J. R. Grace, and M. E. Weber. *Bubbles, Drops, and Particles*. Academic Press, New York, 1978.
- [66] SA. Moris and AJ. Alexander. An investigation of particle trajectories in two-phase flow systems. *J. Fluid Mech.*, 55:193–208, 1972.
- [67] Y. Tsuji, N. Y. Shen, and Y. Morikawa. Lagrangian simulation of dilute gas-solid flows in a horizontal pipe. *Advanced Powder Technology*, 2(1):63–81, 1991.
- [68] Y. Tsuji, Y. Morikawa, and O. Mizuno. Experimental measurement of the Magnus-force on a rotating sphere at low Reynolds numbers. *Journal of Fluids Engineering, Transactions of the ASME*, 107(4):484–488, 1985.
- [69] S. Matsumoto and S. Saito. On the mechanism of suspension of particles in horizontal pneumatic conveying: Monte-carlo simulation based on the irregular bouncing model. *J. Chemical Eng. of Japan*, 9(1):83–92, 1970.
- [70] P.G. Saffman. The lift on a small sphere in a shear flow. *J. Fluid Mech.*, 22:385–400, 1965.
- [71] R. Mei. An approximate expression for the shear lift force on a spherical particle at finite Reynolds number. *Int. J. Multiphase Flow*, 18:145–147, 1992.
- [72] D.S. Dandy and H.A. Dwyer. A sphere in shear flow at finite Reynolds number: Effect of shear on particle lift, drag and heat transfer. *J. Fluid Mech.*, 216:381–410, 1990.
- [73] M. Lopez de Bertodano, F.J. Morage, D.A. Drew, and R.T. Lahey. The modeling of lift and dispersion forces in two-fluid model simulations of a bubbly jet. *J Fluid Eng.*, 126(4):573–577, 2004.
- [74] D.A. Drew, L. Cheng, and R.T. Lahey Jr. The analysis of virtual mass effects in two-phase flow. *Int. J. Multiphase Flow*, 5:233–242, 1979.

- [75] M.S. Kazimi and H.C. No. On the formulation of the virtual mass term in two-fluid models. *Nuclear Engineering and Design*, 95:163–170, 1986.
- [76] J.J.M. Magnaudet. The forces acting on bubbles and rigid particles. *Proceedings ASME Summer Meeting, Vancouver, Canada, FEDSM97-3522*, 1997.
- [77] J.F. Domgin, D.G.F. Huilier, J.J. Karl, P. Gardin, and H. Burnage. Experimental and numerical study of rigid particles, droplets and bubbles motion in quiescent and turbulent flows-influence of the history force. *Proceedings ICMF, Lyon, France*, 1998.
- [78] D.G.F. Huilier and K. Launay. On the influence of the non-stationary forces on the particles dispersion. *3rd ASME/JSME Conference, San Francisco*, July, 1999.
- [79] L. Liang and E.E. Michaelides. The magnitude of Basset forces in unsteady multiphase flow computations. *J. Fluids Engineering*, 114:417–419, 1992.
- [80] I. Kim, S. Elghobashi, and W.A. Sirignano. On the equation for spherical-particle motion: effect of Reynolds and acceleration numbers. *J. Fluid Mech.*, 367:221–253, 1998.
- [81] J.N. Chung and T.R. Troutt. Simulation particle dispersion in an axisymmetric jet. *J. Fluid Mech.*, 186:199–222, 1988.
- [82] S.C.R. Dennis, S.N. Singh, and D.B. Ingham. The steady flow due to a rotating sphere at low and moderate Reynolds numbers. *J. Fluid Mech.*, 110:257–279, 1980.
- [83] D. Milojevic. Lagrangian stochastic-deterministic (LSD) prediction of particle dispersion in turbulence. *Part. Syst. Charact.*, 7:181–190, 1990.

- [84] F. Durst, D. Milojevic, and B. Schönung. Eulerian and lagrangian predictions of particulate two-phase flows. *Appl. Math. Model*, 8, 1984.
- [85] D. I. Graham. Analytical comparison of lagrangian particle dispersion models. *Proceedings of 3rd ICMF, Lyon, France*, 1998.
- [86] M. Sommerfeld. Modellierung und numerische Berechnung von partikelbeladenen, turbulenten Strömungen mit Hilfe des Euler/Lagrange-Verfahrens. *Habilitationsschrift Universität Nürnberg-Erlangen, Shaker Verlag Aachen*, 1996.
- [87] C.T. Crowe, M.P. Sharma, and D.E. Stock. The particle-source-in cell (psi-cell) model for gas-droplet flows. *J. Fluids Eng.*, 99:325–332, 1977.
- [88] Th. Frank. Numerische simulation der feststoffbeladenen Gasströmung im horizontalen Kanal unter Berücksichtigung von Wandrauigkeiten. *Freiberg University of Mining and Technology, Dissertation, Germany*, 1992.
- [89] S. Matsumoto, S. Saito, and S. Maeda. Simulation of gas-solid two-phase flow in horizontal pipe. *Journal of Chemical Engineering of Japan*, 9(1):23–28, 1976.
- [90] Y. Tsuji, N.Y. Shen, and Y. Morikawa. Numerical simulation of pneumatic conveying in a horizontal pipe. *KONA - Powder Science and Technology in Japan*, 3:38–51, 1985.
- [91] M. Sommerfeld. Modelling of particle-wall collision in confined gas-particle flows. *Int. Journal of Multiphase Flows*, 18(6):905–926, 1992.
- [92] A.O. Demuren and W. Rodi. Calculation of turbulence-driven secondary motion in non circular ducts. *J Fluid Mech.*, 140:189–222, 1984.
- [93] F.B. Gessner. The origin of secondary flow in turbulent flow along a corner. *J Fluid Mech.*, 58(1):1–25, 1973.

- [94] A. Huser and S. Biringen. Direct numerical simulation of turbulent flow in a square duct. *J Fluid Mech.*, 257:65–95, 1993.
- [95] M.S. Vazquez and O. Métais. Large-eddy simulation of the turbulent flow through a heated square duct. *J. Fluid Mech.*, 453:201–238, 2002.
- [96] S. Gavrilakis. Numerical simulation of low-Reynolds-number turbulent flow through a straight square duct. *J Fluid Mech.*, 244:101–129, 1992.
- [97] Y. Sato, K. Sato, N. Kasagi, and N. Takamura. Turbulence air flow measurement with three-dimensional particle tracking velocimetry. *Trans. JSME*, 60(571):865–871, 1994.
- [98] S.V. Patankar. *Numerical Heat Transfer and Fluid Flow*. McGraw Hill, New York, 1980.
- [99] J Denev. private communication. 2003.
- [100] U. Piomelli. Large-eddy simulation: achievements and challenges. *Progress in Aerospace Sciences*, 35:335–362, 1999.
- [101] H. Werner and H. Wengle. Large-eddy simulation of turbulent flow over and around a cube in a plate channel. In Schumann et al., editor, *8th Symp. on Turb. Shear Flows*, Berlin, 1993. Springer Verlag.
- [102] ICEMCFD Engineering. *ICEMCFD Hexa Manual Documentation*. 1998.
- [103] S.M. Fraser, A.M. Abdel Razek, and M.Z. Abdullah. Computational and experimental investigations in a cyclone dust separator. *Proceedings of the Institution of Mechanical Engineers, Part E: Journal of Process Mechanical Engineering*, 211 E4(E4):247–257, 1997.



- [104] F. Boysan, B.C.R. Ewan, J. Swithenbank, and W.H. Ayers. Experimental and theoretical studies of cyclone separator aerodynamics. In *Institution of Chemical Engineers Symposium Series*, pages 305–319, 1983.
- [105] N. Syred and J. Beer. Combustion in swirling flows- a review. *Combustion and Flame*, (23):143–201, 1974.
- [106] H. Shalaby, G. Wozniak, K. Pachler, and K. Wozniak. Comparative study of the continuous phase flow in a cyclone separator using different turbulence models. *Int. J. Numer. Meth. Fluids*, 48(11):1175–1197, 2005.
- [107] C. König. Untersuchungen zum Abscheidverhalten von geometrisch ähnlichen Zyklonen. *Dissertation, University of Kaiserslautern, Germany*, 1990.